Joule

CellPress

Article

Predicting the impact of formation protocols on battery lifetime immediately after manufacturing

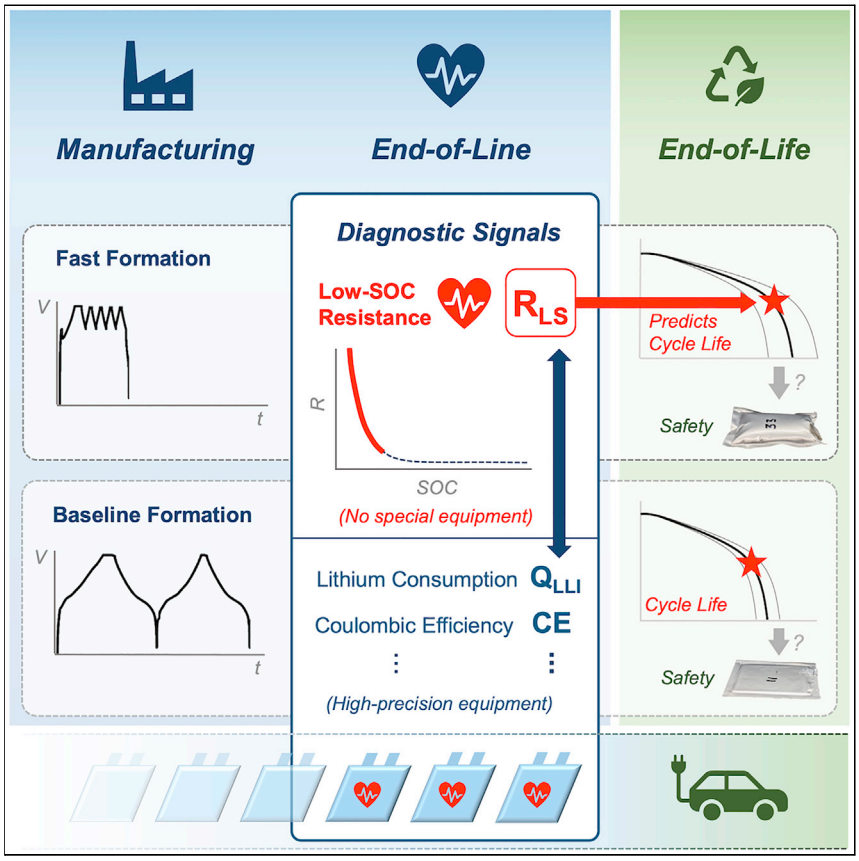

Manufacturing is an integral part of the cost and environmental footprint of batteries. An inexpensive and rapid diagnostic signal was found that can guide improvements in the manufacturing process. The signal can resolve differences in lithium consumed during battery formation and can be used to diagnose the impact of process changes on the lifetime of the battery.

Andrew Weng, Peyman Mohtat, Peter M. Attia, Valentin Sulzer, Suhak Lee, Greg Less, Anna Stefanopoulou

asweng@umich.edu

Highlights

A low-SOC resistance signal measured after formation can accurately predict cycle life

The signal is an indicator for lithium consumed during formation

The signal improves the detectability of lithium consumption over standard measures

The signal is measurable immediately after manufacturing using ordinary equipment

Weng et al., Joule 5, 1–22
November 17, 2021
https://doi.org/10.1016/j.joule.2021.09.015

Please cite this article in press as: Weng et al., Predicting the impact of formation protocols on battery lifetime immediately after manufacturing, Joule (2021), https://doi.org/10.1016/j.joule.2021.09.015

Joule

CellPress

Article

Predicting the impact of formation protocols on battery lifetime immediately after manufacturing

Andrew Weng,[1,4,*] Peyman Mohtat,[1] Peter M. Attia,[2] Valentin Sulzer,[1] Suhak Lee,[1] Greg Less,[3] and Anna Stefanopoulou[1]

SUMMARY

Increasing the speed of battery formation can significantly lower lithium-ion battery manufacturing costs. However, adopting faster formation protocols in practical manufacturing settings is challenging due to a lack of inexpensive, rapid diagnostic signals that can inform possible impacts to long-term battery lifetime. This work identifies the cell resistance measured at low states of charge as an early-life diagnostic feature for screening new formation protocols. We show that this signal correlates to cycle life and improves the accuracy of data-driven battery lifetime prediction models. The signal is obtainable at the end of the manufacturing line, takes seconds to acquire, and does not require specialized test equipment. We explore a physical connection between this resistance signal and the quantity of lithium consumed during formation, suggesting that the signal may be broadly applicable for evaluating any manufacturing process change that could impact the total lithium consumed during formation.

INTRODUCTION

With the increasing demand for electric vehicles, global lithium-ion battery manufacturing capacity is quickly approaching the terawatt-hour scale.[1–3] A key step in battery manufacturing is formation/aging, which has been estimated to account for up to 30% of total manufacturing costs.[4–8] The formation/aging process involves charging and discharging hundreds of thousands of cells in environmentally controlled chambers, an expensive process that takes days to weeks to complete but is necessary to improve battery performance and lifetime.[9–14] Given the high cost burden, manufacturers are incentivized to develop new formation processes that decrease the total time consumed by formation/aging. A variety of fast formation strategies have been studied in academic literature, which employ some combination of rapid charge-discharge cycles, restricted voltage windows, and optimized temperature.[10,15–26] Recent studies have shown that formation time can be decreased while preserving battery lifetime,[16,22,25] although conclusions remain tenuous due to the limited sample sizes typically used.

In real manufacturing settings, a "one-size-fits-all" formation protocol is unlikely to exist since cell designs with different electrolytes, electrodes, and active materials influence important formation factors such as charging capability, electrode wettability, and solid electrolyte interphase (SEI) reaction pathways. However, cycle life testing often takes months or years to complete, posing a significant barrier to the adoption of new, potentially cost-saving formation protocols. While characterization techniques, such as volume change detection,[27–29] impedance spectroscopy,[15,30]

Context & scale

Despite recent progress in battery development, electric vehicles remain unaffordable for many. A key enabler for less expensive electric vehicles is lowered battery manufacturing costs, a significant portion of which is due to the formation and aging process. Although some fast formation protocols have been proposed, a one-size-fits-all solution is unlikely to succeed in practice since an optimized formation protocol for one battery design will, in general, not be optimal for another. New formation protocols need to be vetted for their impacts on long-term battery lifetime—a slow process that hinders the discovery of optimal formation protocols. Here, we identify a scalable method for predicting the effect of new formation protocols on cycle life. The method is obtained directly at the end of the manufacturing line and can be deployed immediately in mass production settings to improve diagnostics of new formation protocols.

acoustic spectroscopy,[31–34] and X-ray tomography,[35,36] have been proposed for use in manufacturing settings, these methods can be costly to implement since the metrology will need to be deployed at scale in the battery factory. Diagnostic features obtainable from already existing cycling equipment and especially those using only current-voltage signals[37] are thus highly attractive.

In this work, we show that the cell resistance at low states of charge (SOC) can be used to screen new formation protocols and predict battery lifetime. Our work shows that this signal, measured at the beginning of life, is a stronger predictor of battery lifetime than conventional signals such as Coulombic efficiency (CE). This metric can be measured within seconds and integrated directly into the battery manufacturing process with no additional capital costs. This low-SOC resistance metric can, thus, be deployed in practical manufacturing settings to accelerate the evaluation of new formation protocols. We further demonstrate that the low-SOC resistance (R_{LS}) decreases as the quantity of lithium lost to the SEI during formation increases. With our physical insight, we propose that R_{LS}, in principle, can also be used to diagnose the impact of any manufacturing process that alters the total lithium consumed during formation.

RESULTS AND DISCUSSION

Fast formation experimental design

Two formation protocols have been implemented in this work: a fast formation protocol previously reported by Wood et al.[15,16] that completes within 14 h (Figure S1B) and a baseline formation protocol (Figure S1C) that completes in 56 h. The fast formation protocol maximizes the time spent at low negative electrode potentials to promote the creation of a more passivating SEI.[15,38–40]

Forty nickel manganese cobalt (NMC)/graphite pouch cells with a nominal capacity of 2.36 Ah were built for this study (Table S1). Half of the cells underwent fast formation, and the remaining cells underwent baseline formation. Cells were further subdivided into "room temperature" and "45°C" aging groups for cycle life testing. The cycling profile was identical for all cells: 1 C charge to 4.2 V with a constant voltage (CV) hold to 10 mA and 1 C discharge to 3.0 V. Reference performance tests (RPTs)[41] were inserted throughout the cycle life test, which includes slow (C/20) charge and discharge curves as well as a hybrid pulse power characterization (HPPC) sequence[42] used to extract the cell internal resistance as a function of SOC.

Our experimental design (Figure S1A) uses larger samples sizes (n = 10 per group) compared with those typically reported in the literature, which often use three cells or fewer per group. The increased sample size enables a more statistically rigorous analysis of the impact of different formation protocols on cell characteristics at the beginning and the end of life.

Fast formation cells had longer cycle life

Fast formation cells had higher average lifetimes than the baseline formation cells under the cycle life test, as shown in Figure 1. The degradation rate of fast formation cells initially track the baseline formation cells closely under both temperatures tested (Figures 1A and 1C). However, after 250 cycles, all cells begin to lose capacity rapidly. The fast formation cells sustained over 100 cycles longer before reaching the end of life, defined as when cells reach 70% of their initial measured capacity (Figures 1B and 1D). This result is highly statistically significant (p-value < 0.001). The general result that fast formation improved lifetime performance holds across multiple performance metrics, including CE (Figure S4), voltage efficiency (Figure S5), as well as

[1]Mechanical Engineering, University of Michigan, Ann Arbor, MI 48109, USA

[2]Materials Science and Engineering, Stanford University, Stanford, CA 94305, USA

[3]University of Michigan Battery Laboratory, Ann Arbor, MI 48105, USA

[4]Lead contact

*Correspondence: asweng@umich.edu

https://doi.org/10.1016/j.joule.2021.09.015

Please cite this article in press as: Weng et al., Predicting the impact of formation protocols on battery lifetime immediately after manufacturing, Joule (2021), https://doi.org/10.1016/j.joule.2021.09.015

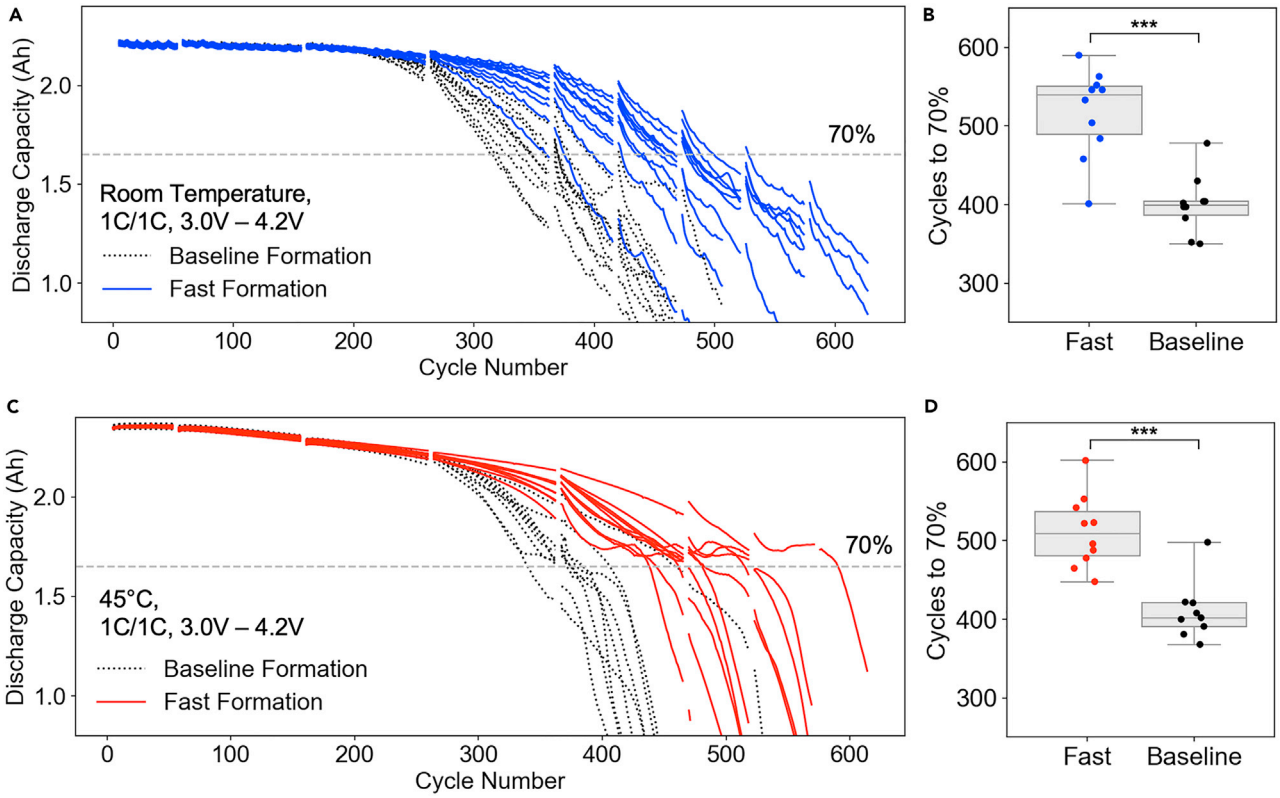

Figure 1. Cycle life test results

(A and C) Discharge capacity for individual cells as measured during the 1 C/1 C aging test at (A) room temperature and (C) 45°C. Gaps in the curves correspond to the embedded reference performance test (RPT) cycles.

(B and D) Cycle life distributions, where the end-of-life is defined as when the cell discharge capacity reaches 70% of the initial capacity. "***" - statistically significant with p-value < 0.001.

when plotted against equivalent cycles (Figure S7). Together, these results support the growing body of evidence that well-designed fast formation protocols can improve cycle life.[15,22,38]

Finding diagnostic signals at the beginning of life

Given the demonstrated impact of formation protocol on battery cycle life, we next investigate methods to quantify the impact of fast formation on the initial cell state. Differences in the initial cell state (e.g., the amount of lithium consumed during formation) may offer clues as to how fast formation could have improved cycle life. We focused on studying signals directly obtainable from full cell current-voltage data, which offer the lowest barrier-to-entry for deployment in real manufacturing settings.

Conventional metrics of formation efficiency

Figures 2A–2C show standard measures of formation efficiency extracted from the formation cycling data. The discharge capacity, Q_d, was measured at the end of each formation protocol during a C/10 discharge step from 4.2 to 3.0 V. Q_d corresponds to the capacity of cyclable lithium excluding the contribution from lithium irreversibly lost to the SEI during formation. Fast formation decreased Q_d by 0.3%, a small but statistically significant difference (p = 0.01). The charge capacity, Q_c, was taken during the initial charge cycle and includes both the capacity of cyclable lithium as well as the capacity of lithium lost irreversibly to the SEI. The quantity of

Please cite this article in press as: Weng et al., Predicting the impact of formation protocols on battery lifetime immediately after manufacturing, Joule (2021), https://doi.org/10.1016/j.joule.2021.09.015

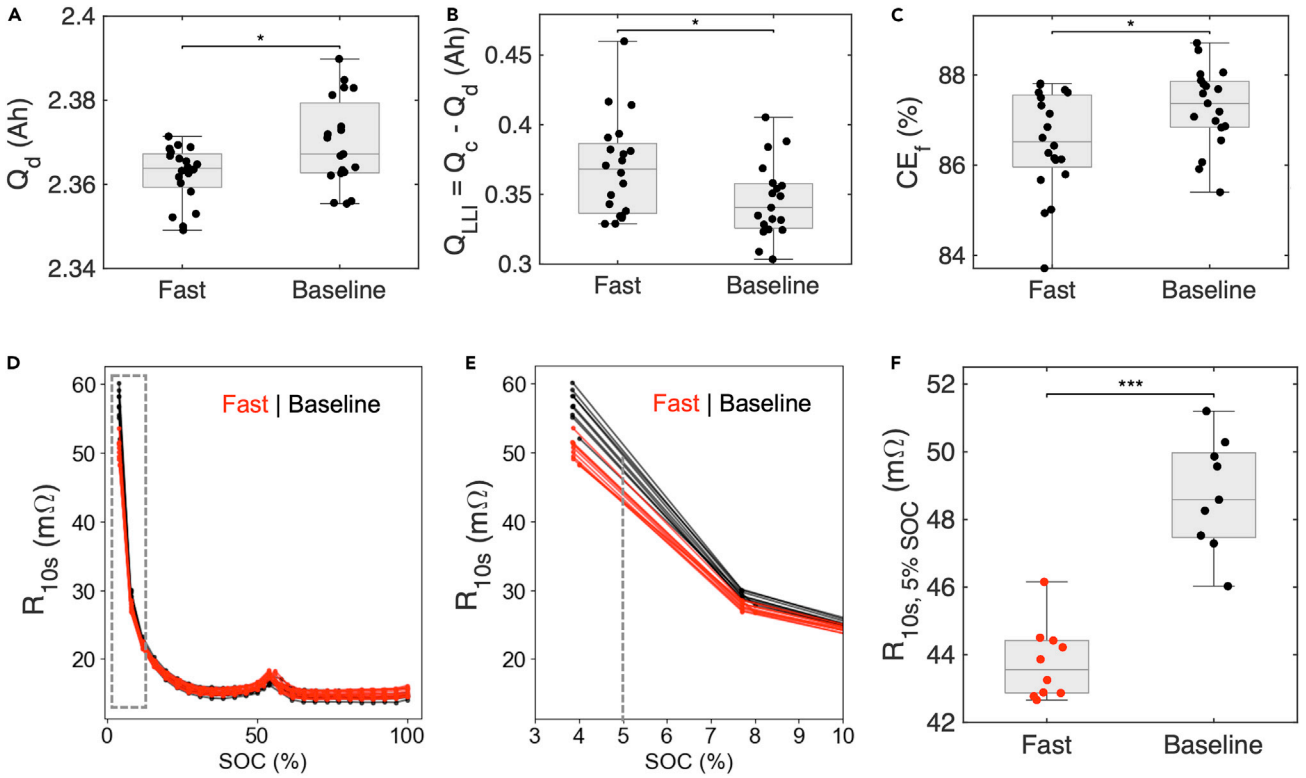

Figure 2. Diagnostic signals for differences in the initial cell state

(A) Final discharge capacity.

(B) Capacity of lithium inventory lost during formation.

(C) Formation Coulombic efficiency, measured from the formation protocol.

(D) 10-s resistance obtained from the hybrid pulse power characterization test prior to the start of the cycle life test.

(E) Magnification of the 10-s resistance at low SOCs.

(F) Distribution of 10-s resistance at 5% SOC comparing between the two formation protocols.

(A–C) Are extracted directly from the formation test protocol run on each cell. (D–F) Are extracted from the initial reference performance test from the 45°C cycle life test (see Figure S9 for the results from the room temperature cycle life test). "*"—statistically significant with p-value < 0.05. "***"—statistically significant with p-value <0.001.

lithium inventory lost to the SEI can be calculated as $Q_{LLI} = Q_c - Q_d$ (Figure 2B). Note that while the two formation protocols differed in the initial charging rate, Q_c remains a fair comparison metric since both charge protocols ended on a potentiostatic hold at 4.2 V until the current dropped below C/100. Fast formation increased Q_{LLI} by 23 mAh (p = 0.03). Finally, we also included another common evaluation metric, the formation CE, defined as $CE_f = Q_d/Q_c$ (Figure 2C), which shows that fast formation decreased CE_f by 0.8% (p = 0.02). Measured values are summarized in Table 1. Together, the results show that fast formation marginally increased the amount of lithium consumed during formation. A p-value of less than 0.05 in all cases indicate that the measured differences, while small, are statistically significant to a least a 95% confidence level.

Low-SOC resistance

Following formation, the cell internal resistance was measured using the hybrid pulse power characterization (HPPC) technique[42] prior to the start of the cycle life test. During this test, a series of 10-s, 1 C discharge pulses were applied to the cell at varying SOCs, and the resistance is calculated using Ohm's law (Figure S8). The 10-s resistance, R_{10s}, was plotted against SOC for all cells cycled at 45°C

Please cite this article in press as: Weng et al., Predicting the impact of formation protocols on battery lifetime immediately after manufacturing, Joule (2021), https://doi.org/10.1016/j.joule.2021.09.015

Table 1. Comparison of initial cell state metrics

Metric	Unit	Temperature	Baseline formation	Fast formation	Delta (abs)	Delta (%)	*p*-value
Q_d	mAh	room temp	2370 (11)	2362 (7)	−8	−0.3%	0.01
Q_{LLI} (Q_c−Q_d)	mAh	room temp	346 (27)	369 (35)	+23	+6.6%	0.03
CE_f	%	room temp	87.3 (0.9)	86.5 (1.1)	−0.8	−0.9%	0.02
$R_{10s,5\%SOC}$ (R_{LS})	mΩ	room temp	139.7 (2.9)	130.0 (2.3)	−9.7	−6.9%	< 0.001
$R_{10s,5\%SOC}$ (R_{LS})	mΩ	45°C	48.7 (1.6)	43.8 (1.1)	−4.9	−10.0%	< 0.001
$R_{10s,\ 90\%SOC}$	mΩ	room temp	23.6 (0.1)	23.9 (1.0)	+0.3	+1.3%	0.28
$R_{10s,\ 90\%SOC}$	mΩ	45°C	14.5 (0.4)	14.9 (0.5)	+0.4	+2.8%	0.10

Values are reported as mean (standard deviation). Q_d, Q_{LLI}, and CE_f are extracted directly from the formation test protocol. Resistance metrics are extracted from the initial reference performance test at the beginning of the cycle life test.

(Figure 2D). R_{10s} generally remained flat at mid-to high SOCs. The peak at 55% SOC corresponds to the stage 2 solid-solution regime of the graphite negative electrode.[43] R_{10s} rose sharply below 10% SOC. Focusing on the low-SOC region (Figure 2E), we observed that R_{10s} measured at 4% and 8% SOC were lower for fast formation cells compared with that of baseline formation cells. This result was highly statistically significant, with a *p*-value less than 0.001 (Figure 2F). A similar result held when R_{10s} was measured at room temperature (Figure S9). At mid to high SOCs, differences in R_{10s} between fast formation and baseline formation cells were generally not statistically significant (Figure S9). Thus, differences in resistance between the two formation protocols appeared uniquely at low SOCs. All initial cell state metrics are summarized as part of Table 1.

To study the robustness of the low-SOC resistance signal, we varied the SOC setpoint between 4% and 10% and also computed the resistance under 1 and 5-s pulse durations. In all cases, the resistance metric provided a high degree of contrast between the two different formation protocols (Figures S10 and S11). The lowest SOC measured in our dataset was 4% SOC.

The remainder of the paper will focus on the resistance measured at 5% SOC and with a 10-s pulse duration. From hereon, this metric will be referred to as the "low-SOC resistance," R_{LS}.

Low-SOC resistance as a diagnostic signal: A data-driven perspective

Low-SOC resistance correlates to cycle life

To evaluate the merit of R_{LS} as a diagnostic feature, we explored the correlations between the initial cell metrics (Figure 2) and cycle life, defined as cycles to 70% of the initial capacity. The results are shown in Figure 3. Out of all metrics studied, R_{LS} was the only signal with a meaningful correlation to cycle life, with a correlation coefficient of $\rho = -0.84$. Other metrics such as Q_d and CE_f were poorly correlated to cycle life ($|\rho| < 0.5$). We attribute the weakness of these correlations to the poor signal-to-noise inherent in cell capacity measurements in the absence of high-precision cycling,[44,45] a topic we explore in detail later. The resistance measured at high SOCs also did not correlate to cycle life. From these results, we observe that the low-SOC signal uniquely holds information related to cycle life. These results have been reproduced for different end-of-life definitions ranging between 50% and 80% (Figures S13 and S14), as well as for charge pulses (Figure S15).

Low-SOC resistance predicts cycle life

To understand if R_{LS} can be used to improve battery lifetime prediction, we trained univariate prediction models with regularized linear regression models inspired by

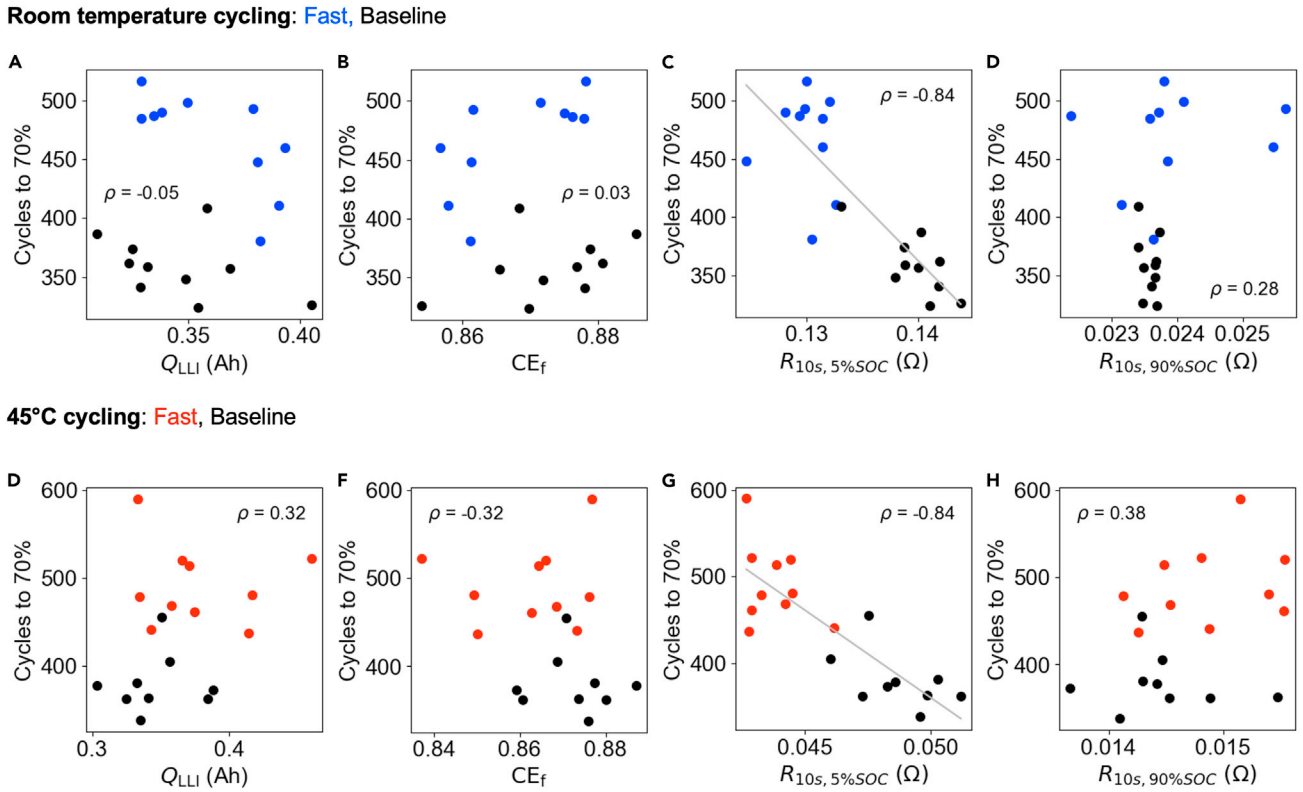

Figure 3. Correlation between early-life diagnostic signals and cycle life

(A–D) Correlations under room temperature cycling.

(E–H) Correlations under 45°C cycling.

Cycle life is defined as cycles to 70% of initial capacity. Q_{LLI} and CE_f are taken directly from the formation test. $R_{10s,5\%SOC}$ (R_{LS}) and $R_{10s,90\%SOC}$ are measured at the beginning of the cycle life test and, thus, share the same temperature as the cycle life test.

Severson et al.[46] The performance of the predictive models are summarized in Table 2. A dummy regressor, which predicts the mean of the training set and requires no cycling data, was included as a benchmark. For room temperature cycling, the model trained using R_{LS} achieved the lowest test error of 6.9% compared with 13.3% for the dummy regressor. A similar result held under 45°C cycling. To compare, we also included the $\mathrm{Var}(\Delta Q_{100-10}(V))$ metric introduced by Severson et al.,[46] defined as the variance in the discharge capacity versus voltage curve between cycle 10 and cycle 100. When applied to our dataset, this metric did not yield a significant improvement over the dummy regressor. This result suggests that R_{LS} is a stronger predictor of battery lifetime than $\mathrm{Var}(\Delta Q_{100-10}(V))$.

We repeated this study with multivariate regularized linear regressions: one using the three capacity-based features from formation (Q_{LLI}, CE_f, and Q_d) and another using the previous three formation features plus R_{LS}. Using only the features from formation, no improvement over the dummy regressor was achieved. By including R_{LS} in the feature set, however, the test error was improved. Yet, the test error achieved did not exceed the test error of the univariate model using R_{LS} alone. This result suggests that the chosen set of formation features does not provide useful information about cycle life beyond what is provided by R_{LS}. This result is counter-intuitive considering the important role that lithium consumption plays in determining battery lifetime,[9–14] which should be reflected in the formation features such as Q_{LLI} and CE_f. We hypothesize that the reason for the poor model

Please cite this article in press as: Weng et al., Predicting the impact of formation protocols on battery lifetime immediately after manufacturing, Joule (2021), https://doi.org/10.1016/j.joule.2021.09.015

Table 2. Training and testing errors for different lifetime prediction models

		Room temp		45°C	
Model	*Data needed*	Train	Test	Train	Test
Dummy regressor	None	13.3 (1.0)	14.4 (4.0)	14.0 (0.9)	15.1 (3.6)
R_{LS}	3 cycles	6.9 (0.5)	8.0 (2.8)	6.5 (0.6)	7.4 (2.9)
Q_{LLI}	formation	12.2 (1.2)	14.0 (4.6)	14.1 (0.8)	15.2 (4.4)
CE_f	formation	12.2 (1.2)	13.8 (4.5)	14.1 (0.7)	15.1 (4.3)
Q_d	formation	12.0 (1.2)	13.6 (5.0)	13.5 (0.8)	15.0 (4.0)
$Var(\Delta Q_{100-10}(V))$	100 cycles	11.6 (1.7)	14.4 (5.2)	10.3 (1.1)	11.5 (4.7)
$Q_{LLI} + CE_f + Q_d$	formation	12.8 (1.3)	14.5 (5.1)	13.4 (1.1)	14.1 (4.0)
$Q_{LLI} + CE_f + Q_d + R_{LS}$	3 cycles	7.2 (1.1)	9.4 (4.0)	6.5 (1.0)	7.4 (2.9)

Values represent means (standard deviations). The dummy regressor model uses no features and returns the mean of the training set, and hence is the baseline against which to judge the performance of other features. All remaining models use a ridge regression with nested cross-validation to determine the optimal regularization strength. See experimental procedures.

performance using formation signals is not because these formation signals lack physical meaning. Rather, due to the absence of high-precision cycling and temperature control, the useful information within these signals may be masked by the noise in the data (e.g., due to current integration errors and temperature variations over the course of 10+ h of formation) R_{LS} appears to be able to overcome these limitations. We explore the connection between R_{LS} and the other formation metrics in detail later.

As defined in this work, the model trained using R_{LS} required just three cycles of lifetime testing, i.e., one diagnostic cycle, where the two preceding cycles consisted of slow-rate charge-discharge cycles as part of the RPT inserted at the beginning of the cycle life test. By comparison, $Var(\Delta Q_{100-10}(V))$ requires 100 cycles of lifetime testing. For future implementations, R_{LS} can be incorporated directly into the formation protocol, further decreasing the required measurement time. The total amount of data required to exercise each predictive model is summarized in Table 2.

Overall, the correlation and prediction results suggest that R_{LS} may be useful for advancing broad-scale efforts to improve cycle life prediction using small and readily obtainable datasets at the beginning of life. While the results are promising, they are also limited, since only two types of formation protocols have been studied here. To understand the extent to which R_{LS} can generalize to other applications (e.g., chemistries, use cases, and cell designs) and to understand the relation between R_{LS} and the other formation signals, the rest of the paper will focus on providing a physical interpretation of R_{LS}. A mechanistic understanding of R_{LS} will provide the necessary context required to evaluate the general scope of applicability and limitations of the method.

Low-SOC resistance as a diagnostic signal: A mechanistic perspective

Understanding the physical interpretation of diagnostic signals can help assess whether prediction frameworks leveraging such signals can generalize to new systems. In principle, different formation protocols, manufacturing process changes, and cell design changes could all lead to changes in lithium consumption and active material losses during formation. To this end, we will first review the commonly accepted theory of SEI passivation and show how our observations of Q_{LLI} and CE_f support this theory. Next, we will show that our observations of R_{LS} are consistent with this theory but provide a stronger and more easily measurable signal compared with conventional measures.

Please cite this article in press as: Weng et al., Predicting the impact of formation protocols on battery lifetime immediately after manufacturing, Joule (2021), https://doi.org/10.1016/j.joule.2021.09.015

Benefits of fast formation on cycle life

Lithium intercalation at negative electrode potentials higher than 0.25–0.5 V versus Li/Li^+ is generally associated with the formation of a porous, poorly passivated SEI film.[12,14,40,47,48] Conversely, lithium intercalation at negative electrode potentials below 0.25–0.5 V have been found to promote the formation of a more conductive and passivating SEI film.[38,40] Attia et al.[38] showed that the reduction of ethylene carbonate (EC) at negative electrode potentials above 0.5 V versus Li/Li^+ is non-passivating. This negative electrode potential corresponds to a full cell voltage of below 3.5 V, neglecting overpotential contributions. Hence, an ideal formation protocol would minimize the time spent charging below 3.5 V while maximizing the time spent above 3.5 V. The fast formation protocol we tested[15] achieves this objective by rapidly charging the cell to above 3.9 V at a 1 C rate and subsequently cycling the cell between 3.9 and 4.2 V, thus decreasing the time associated with the non-passivating EC reduction reaction. Focusing on the initial charge cycle, fast formation cells spent only 2 min below 3.5 V and 12.9 h above 3.5 V, while baseline formation cells spent 30 min below 3.5 V and 9.4 h above 3.5 V. Fast formation decreased the time spent below 3.5 V by 28 min. Fast formation resulted in a net increase in total lithium consumed during formation, ΔQ_{LLI}, by 23 mAh (Table 1). This increase is attributed to the additional lithium consumed to form the passivating SEI.

While fast formation cells consumed more lithium during formation and, thus, exhibited lower CE_f (or, equivalently, higher Q_{LLI}), these cells lasted longer on the cycle life test. While a lower initial CE is conventionally associated with poor cycle life performance,[44,49] the opposite was true in our study since the additional lithium consumed during fast formation was associated with the creation of a more passivating SEI. A more passivating SEI can, for example, lower the rate of electrolyte reduction reactions associated with the formation of solid products that decrease the negative electrode porosity and subsequently increase the propensity for lithium plating during charge.[50,51] A more passivating SEI could, therefore, play a role in delaying the "knee-point" observed in the cycle test data. Our result reinforces the notion that passivation of the SEI during the first cycle plays an important role in improving battery cycle life.

Lithium loss dominates overall cell capacity loss over cycling

We performed a voltage fitting analysis[44,52–55] to confirm that the main failure mode in our cells is the loss of lithium inventory (LLI) over cycle life (Figures S18 and S19). We found that LLI can fully account for the thermodynamic (i.e., C/20) cell capacity loss over life. The knee-point in LLI over cycle life coincides with the knee-point in the capacity loss. All cells also experienced an increase in the loss of active material (LAM) in the negative electrode (LAM_{NE}) after the knee-point, which could indicate the occurrence of porosity decrease and/or electrolyte depletion as a result of a less passivating SEI, as discussed previously. The increased LAM_{NE} after the knee-point was less prominent in the fast formation cells, suggesting that the more passivating SEI generated from fast formation could be playing a role in delaying the knee-point to improve lifetime. Finally, all cells experienced a knee-point in the capacity fade rate irrespective of whether the discharge capacity is measured at higher (C/3) or lower (C/20) C-rates (Figure S20), indicating that kinetic limitations cannot fully account for the observed knee-point in the cycle life data. The origin of the capacity loss, therefore, has a strong thermodynamic component, which can be attributed to the LLI. This analysis further supports the theory that consuming more lithium at low negative electrode potentials during formation can create a passivating SEI that is beneficial to cycle life.[38]

Please cite this article in press as: Weng et al., Predicting the impact of formation protocols on battery lifetime immediately after manufacturing, Joule (2021), https://doi.org/10.1016/j.joule.2021.09.015

Low-SOC resistance is attributed to kinetic limitations in the positive electrode

To explore possible physical connections between R_{LS} and the impact of fast formation on cycle life, we first developed a physical interpretation of the R_{LS}. Here, we focus our discussion on the resistance contributions from the positive and negative electrode. While other cell components (e.g., current collectors, tabs, and electrolyte) also contribute to the total cell resistance, they are not known to depend on SOC and, hence, cannot explain the rising resistance measured at low SOCs.

Positive electrode diffusion limitations generally play a significant role in the low-SOC cell resistance in NMC/graphite systems. The solid-state diffusion coefficient in NMC materials has been measured to decrease by more than one order of magnitude at high states of lithiation,[56] a phenomenon attributed to the depletion of divacancies needed to support diffusion as the electrode becomes fully lithiated.[57,58] Using half-cell HPPC measurements, we experimentally verified that the positive electrode dominates the R_{LS}. In the coin cell form factor, the 10-s resistance of graphite/Li stayed below 100 mΩ as the graphite approached full delithiation, while the 10-s resistance of NMC/Li exceeded 1,000 mΩ as the NMC approached full lithiation (Figure S22). This finding is consistent with previous empirical studies on NMC/graphite systems.[59–61] In particular, An et al.[59] used a three-electrode pouch cell configuration to show that, for an NMC/graphite system, the positive electrode accounts for nearly all of the measured full cell resistance at all SOCs.

Charge transfer kinetics at either electrode could also play a role at determining total cell resistance. The charge transfer process at either electrode can be modeled using the Butler-Volmer equation[62]:

$$j = k_0 c_e^{1-\alpha}(c_{s,max} - c_{s,e})^{1-\alpha} c_{s,e}^{\alpha}\left(exp\left(\frac{(1-\alpha)F}{RT}\eta\right) - exp\left(-\frac{\alpha F}{RT}\eta\right)\right). \quad \text{(Equation 1)}$$

In this equation, j is the reaction flux, the exponential terms describe the overpotential dependence of the forward and backward reactions, and the exponential prefactor terms together describe the exchange current density. $c_{s,max}$ is the theoretical maximum allowable lithium concentration in the solid phase, $c_{s,e}$ is the surface concentration of lithium, and k_0 is the reaction rate constant. The exchange current density approaches zero as the electrode becomes either fully lithiated or fully delithiated. Indeed, our coin cell data show that as the graphite negative electrode approaches full delithiation, the measured resistance rises steeply (Figure S22i). However, the magnitude of this charge transfer effect remains small compared with the contribution from the diffusion-limited NMC positive electrode (Figure S22h) at high states of lithiation.

In summary, we attribute the R_{LS} to kinetic limitations in the positive electrode. This result was experimentally verified using coin cell measurements of electrode resistances and is consistent with literature findings.[59–61] The kinetic limitation arises from a combination of diffusion and charge transfer limitations in the positive electrode. For NMC/graphite systems, diffusion limitations (i.e., "kinetic hindrance[58]") is a major component of the rapid rise in measured resistance at low SOCs.

Lithium consumption leads to an apparent decrease in low-SOC resistance

Fast formation decreased the measured R_{LS}. From our previous analysis, fast formation also increased the lithium consumed during formation (Q_{LLI}) to create a more passivating SEI. To explain the connection between these two quantities, we employed a simple electrode stoichiometry model that describes both the thermodynamic potentials and kinetic limitations of both electrodes. Figure 4A shows the

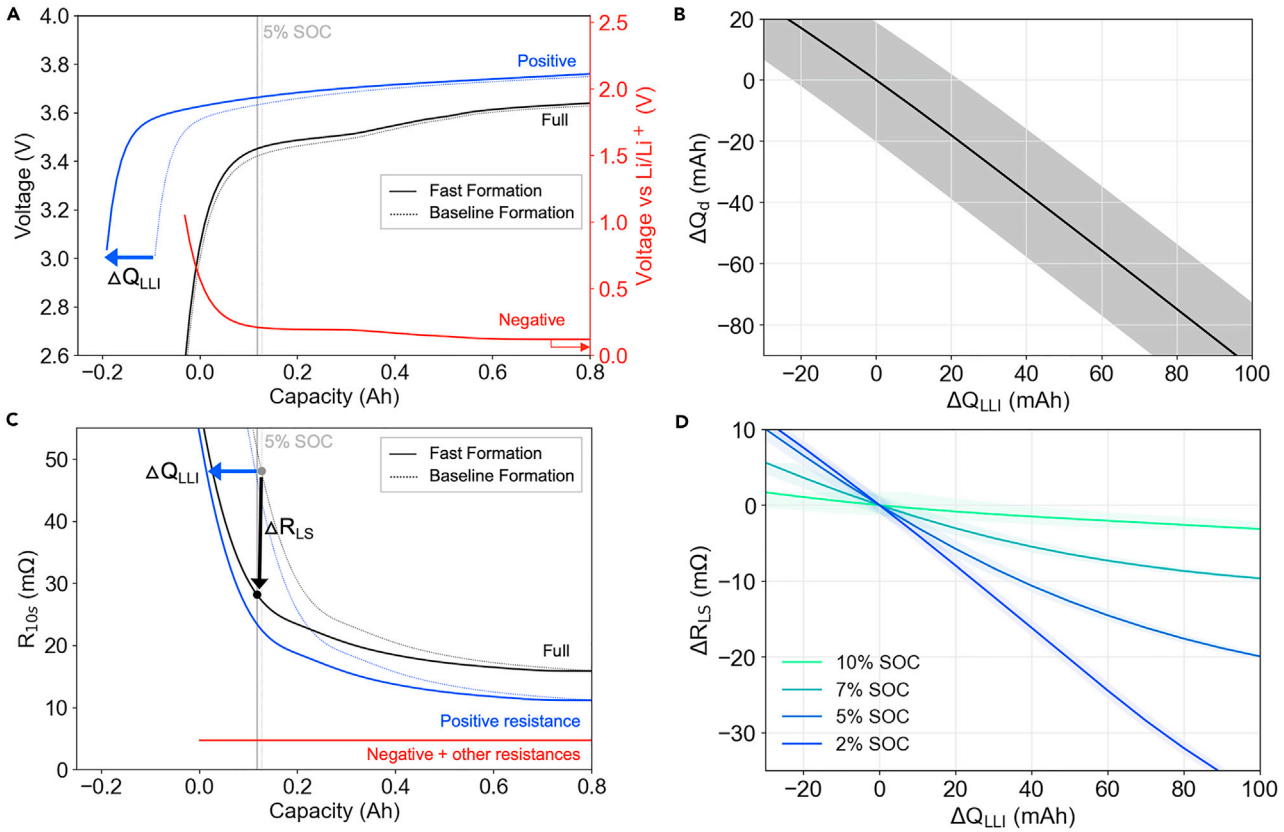

Figure 4. Electrode stoichiometry model illustrating the impact of lithium consumption on low-SOC resistance

(A) Relative alignment of the positive (blue) and negative (red) equilibrium potential curves after baseline formation (dashed lines) and fast formation (solid lines). The full cell equilibrium potential curve is shown in black.

(B) Effect of increasing lithium consumption (ΔQ_{LLI}) on the measured discharge capacity.

(C) The corresponding cell resistance curves, where the measured full cell resistance (black) have been broken down into positive electrode charge resistance (blue) and all other resistances (red).

(D) The effect of increasing ΔQ_{LLI} on the measured low-SOC resistance for varying SOC set-points. Bands in (B and D) indicate estimates of the measurement error bound using conventional battery cycling equipment, clarifying R_{LS}'s improved accuracy in capturing changes in Q_{LLI} when compared with Q_d (see Note S1 for an error analysis).

relative alignment of the positive and negative equilibrium potential curves after baseline formation and fast formation. The origin of the capacity axis corresponds to 0% SOC (3.0 V) after baseline formation. The gap between the positive and negative potential curve endpoints is attributed to the lithium lost to the SEI during formation or Q_{LLI}.[44,53] By comparison, the curves prior to formation do not have a gap, corresponding to $Q_{LLI} = 0$ (Figure S23). The positive electrode curve was shifted to the left by some amount ΔQ_{LLI} to emulate the impact of additional lithium consumed during fast formation. Here, ΔQ_{LLI} has been set to an exaggerated value of 100 mAh for graphical clarity. An alternative graphic is provided in Figure S24, which sets ΔQ_{LLI} = 23 mAh to coincide with the measured difference between baseline formation and fast formation.

Figure 4C shows the corresponding full cell 10-s resistance measured from the HPPC test. The full cell resistance is partitioned to model a scenario in which the positive electrode dominates the R_{LS}, consistent with previous findings. The resistance curve of the positive electrode must also translate to the left by the same amount ΔQ_{LLI} due to the increased lithium consumed during fast formation. From the reference

Please cite this article in press as: Weng et al., Predicting the impact of formation protocols on battery lifetime immediately after manufacturing, Joule (2021), https://doi.org/10.1016/j.joule.2021.09.015

frame of the full cell, the measured R_{LS} will decrease by ΔR_{LS}. In this manner, R_{LS} can decrease without any real change in positive electrode kinetic properties. The decrease in R_{LS} reflects the shifting of the positive electrode stoichiometry window as lithium is consumed.

Two additional observations support the connection between ΔQ_{LLI} and ΔR_{LS}. First, R_{LS} appears to be positively correlated to CE_f and negatively correlated to Q_{LLI} (Figure S12), a result consistent with theory and predicted by the electrode stoichiometry model. The strengths of the correlations are generally weak, with correlation coefficients, $|\rho|$, ranging between 0.2 and 0.5. We attribute the weakness of the correlations to the poor signal-to-noise of the capacity measurements using typical battery cycling equipment, which may compound at room temperature where the temperature is not strictly controlled (Figure S25). Second, we note that the resistance around 90% SOC is insensitive to small changes in SOC, so changes in resistance at 90% SOC provides a measure of true resistance changes rather than apparent changes due to electrode stoichiometry shifts (Figure 2D). Fast formation did not significantly increase the resistance at 90% SOC (Figure S9), so changes in R_{LS} are not likely due to material changes in the cell resistance (e.g., due to resistive surface films). This observation further supports the hypothesis that changes in R_{LS} are due to electrode stoichiometry window shifts in the presence of lithium consumption.

Low-SOC resistance improves the observability of lithium loss during formation

Figure 4B shows that the sensitivity of the measured cell discharge capacity (ΔQ_d) to the lithium consumed (ΔQ_{LLI}) is 0.9 mAh/mAh. The error in measuring Q_d is 20 mAh due to current integration inaccuracies using ordinary cycling equipment. Hence, using Q_d to estimate Q_{LLI} leads to a measurement error of 22 mAh. Since the total difference in lithium consumed between fast formation and baseline formation is 23 mAh, measurement noise may prevent ΔQ_d from effectively resolving this difference. In our experiments, we relied on large sample sizes ($n = 10$ per group) to resolve the small difference in lithium consumption between the two formation protocols.

Figure 4D shows that the sensitivity of the low-SOC resistance (ΔR_{LS}) to ΔQ_{LLI} is 0.22 mΩ/mAh when measured at 5% SOC. The error in measuring R_{LS} is 0.88 mΩ due to the voltage and current precision for calculating resistance using Ohm's law and using ordinary cycling equipment. Hence, using R_{LS} measured at 5% SOC to estimate Q_{LLI} leads to a measurement error of 4 mAh, a five-fold improvement over using Q_d. Figure 4D further shows that the sensitivity of R_{LS} is improved at lower SOCs. For example, R_{LS} measured at 2% SOC leads to a measurement error of 2.5 mAh. Any SOC set-point lower than 7% SOC makes R_{LS} a more precise measure of Q_{LLI} compared with Q_d. (See supplemental information for a detailed derivation of the measurement errors.)

Generalizability

So far, we have explored the sensitivity of R_{LS} to lithium lost during formation for an NMC/graphite system. By understanding the benefits of fast formation,[38] we rationalized why R_{LS} was predictive of cycle life for our system. Here, we discuss the application of R_{LS} toward understanding other degradation modes, chemistries, and use cases. This discussion sets the stage for understanding how R_{LS} may be incorporated into generalizable lifetime prediction and diagnostic frameworks.

Please cite this article in press as: Weng et al., Predicting the impact of formation protocols on battery lifetime immediately after manufacturing, Joule (2021), https://doi.org/10.1016/j.joule.2021.09.015

R_{LS} can detect active material losses

In principle, some small quantity of positive and negative active material could be lost during formation, i.e., due to expansion and contraction of the electrodes during initial lithiation and delithiation. In the positive electrode, lithiation-induced stresses can induce particle fracturing in the metal oxide particles,[63–65] leading to capacity loss. In the negative electrode, while graphite cracking is unlikely to occur under most applications,[66] insufficient binder adhesion or electrolyte wetting[67] could create local islands of isolated graphite particles, leading to active material loss.

We develop a simple mechanistic electrode stoichiometry model to examine the influence of active material losses in both the positive and negative electrodes. Our model differentiates between LAM in the lithiated phase versus the delithiated phase.[53] For the positive electrode, LAM in the delithiated phase is represented by shrinking the positive electrode equilibrium potential curve with the point of minimum stoichiometry fixed (i.e., shrinking from the bottom, Figure S26A), while LAM in the lithiated phase is represented by shrinking the positive electrode equilibrium potential curve with the point of maximum stoichiometry fixed (i.e., shrinking from the top, Figure S26D). R_{LS} was found to increase with loss of positive active material, but only in the delithiated phase (Figure S26B). By contrast, active material lost in the lithiated phase bears a negligible effect on R_{LS} (Figures S26D and S26E). This result can be understood graphically by considering the influence of the positive curve shifts on the positive electrode stoichiometry at low SOCs. In the case of LAM in the lithiated phase, the positive electrode stoichiometry at low SOCs does not significantly change, whereas in the delithiated case, the maximum positive electrode stoichiometry increases, causing R_{LS} to increase. Note that Q_d has the opposite sensitivity: Q_d is sensitive to LAM in the lithiated state only. Hence, R_{LS} and Q_d complement each other in the study of positive electrode active material loss mechanisms. A similar analysis can be done on the negative electrode (Figure S27).

Figure S28 compares the sensitivity of R_{LS} and Q_d to the four different modeled cases of active material losses. The results highlight that the measured value of R_{LS} is determined by multiple degradation factors, including both lithium inventory loss and active active material losses. It would therefore be impractical to use R_{LS} to identify any dominant degradation mode without some *a priori* understanding of the system through additional characterization and analysis. For diagnostic purposes, we recommend that R_{LS} be used within the context of a broader set of non-destructive techniques to enrich the understanding of degradation mechanisms. From a data-driven prediction perspective, however, the sensitivity of R_{LS} to active material losses in addition to lithium inventory loss may make it a more robust indicator for multiple degradation modes. In general, R_{LS} may need to be coupled with other signals to improve the observability of distinct degradation modes.

When is R_{LS} sensitive to lithium loss?

We have so far focused on an NMC111/graphite system where kinetic limitations in the positive electrode dominates R_{LS}, a result that holds for nickel-rich cathode chemistries such as nickel cobalt aluminum (NCA) and higher nickel content NMC materials.[57,58] In general, electrode design factors such as particle size[68] and surface modifications[69] could impact the relative contribution of each electrode to R_{LS}. To study how such changes could modify the sensitivity of R_{LS} to changes in Q_{LLI}, we performed a sensitivity study using our electrode stoichiometry model by varying the proportion of the total cell resistance attributed to the positive electrode. The results (Figures S29 and S30) show that R_{LS} becomes ineffective at quantifying Q_{LLI} if the positive electrode contributes to less than 50% of the total cell resistance at

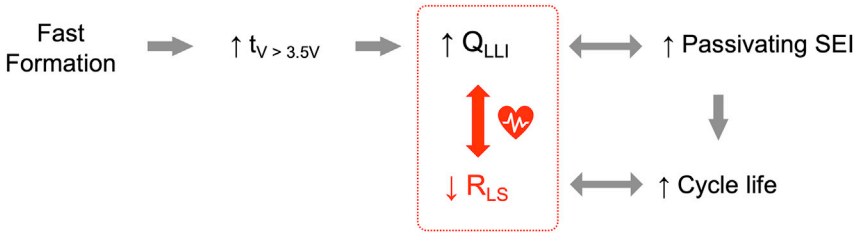

Figure 5. Connection between the fast formation degradation pathway and the low-SOC resistance early-life diagnostic signal

Inner box: the relationship between low-SOC resistance (R_{LS}) and lithium consumed during formation (Q_{LLI}) is general.

Outer box: the relationship between low-SOC resistance (R_{LS}) and cycle life applies specifically to fast formation, where higher Q_{LLI} signaled a higher quantity of passivating SEI[38] which improved cycle life. The relationship between R_{LS} and cycle life may differ for other use cases.

low SOCs. This result suggests that the utility of R_{LS} as a diagnostic signal for Q_{LLI} diminishes for systems where the positive electrode is not the main contributor to R_{LS}.

When can R_{LS} predict cycle life?

Our cycle life correlation study was presented in the context of the study of fast formation. To understand whether R_{LS} can predict cycle life for other use cases (i.e., chemistries and aging conditions), we start by reviewing why R_{LS} was predictive of cycle life for fast formation. Figure 5 outlines the proposed connection between fast formation and cycle life. Fast formation spent more time above 3.5 V, creating a higher quantity of SEI that is more passivating.[38] The passivating SEI improved cycle life by protecting the negative electrode against side reactions over life. R_{LS} provided an estimate of the amount of lithium consumption during formation, Q_{LLI}, where more lithium consumed implied a higher amount of passivating SEI formed leading to improved cycle life.. This physical description rationalizes the predictive power of R_{LS} within the context of the specific degradation pathway (fast formation) and chemistry (NMC/graphite) explored in this study.

To gain confidence that R_{LS} can predict cycle life for other use cases, the relationship between lithium loss (Q_{LLI}) and cycle life must first be understood. For our study, the knowledge that increased Q_{LLI} signals a more passivating SEI was necessary for rationalizing why higher Q_{LLI} after formation could be beneficial to cycle life. For other use cases, the opposite may be true. For example, low first cycle efficiencies for silicon-containing anodes[70] or lithium metal anodes[71] generally indicate poor negative electrode passivation, which leads to poor cycle life. Under such use cases, R_{LS} may still be predictive of cycle life, but the relationship may become inverted.

Unique properties of R_{LS}

Here, we highlight several unique properties of using R_{LS} as an early-life diagnostic signal. First, since the positive electrode kinetics becomes increasingly poorer as the electrode approaches full lithiation, the sensitivity of R_{LS} to lithium loss (Q_{LLI}) improves as the measurement SOC decreases (Figure 4D). The results from this study used R_{LS} measured at 5% SOC. For future work, the sensitivity to Q_{LLI} may be further improved by taking the measurement at even lower SOCs. Second, R_{LS} can be used to extract information about Q_{LLI} within seconds and, therefore, can be deployed in manufacturing settings without decreasing production speed. By contrast, conventional measurements of Q_{LLI} relying on Coulomb counting require full charge-discharge cycles during formation, which could take hours to days to complete.

Please cite this article in press as: Weng et al., Predicting the impact of formation protocols on battery lifetime immediately after manufacturing, Joule (2021), https://doi.org/10.1016/j.joule.2021.09.015

Since measuring R_{LS} does not require full cycles, R_{LS} is also suitable for diagnosing differences in lithium consumption between formation protocols with different charge and discharge conditions. Finally, the magnitude of R_{LS} is larger the earlier in life it is measured. As the cell ages, continual LLI will cause the highly sloped region of the positive electrode resistance curve to become inaccessible during the normal full cell voltage operating window. Typically, diagnostic features become less predictive of cycle life the earlier in life the feature is sampled.[46] R_{LS} is expected to have the opposite relationship: the earlier in life R_{LS} is sampled, the more sensitive it will be to changes in Q_{LLI}.

Diagnosing state of health beyond cycle life: practical considerations

Our discussion has so far focused on evaluating the merits of R_{LS} for diagnosing cycle life. However, in real manufacturing settings, cycle life is only one of many considerations for adopting new formation protocols. Here, we introduce two such considerations: (1) impact to gas buildup over life, and (2) impact to aging variability over life. In our analysis, R_{LS} could not be used to learn the impact of fast formation on gas buildup or aging variability. Here, we give an overview of these observations.

Gas buildup over life

Swollen cells in a battery pack can compromise pack integrity and pose safety hazards to first-responders for electric vehicle fire accidents.[72] Understanding the impact of formation protocols on cell swelling is, therefore, just as important as understanding the impact on cycle life for practical purposes.

Fast formation caused a significant degree of swelling at the end of life for cells cycled at 45°C (Figures S31 and S32). At this temperature, 9 of 10 fast formation cells showed visible signs of swelling, compared with only 2 of 10 for baseline formation. None of the cells cycled at room temperature showed any appreciable degree of swelling. All swollen pouch cells were compliant and compressible, indicating that gas is occupying the space inside the pouch bags. Since the cells were de-gassed after formation, the gases present excludes the gas generated during formation and represent only the accumulation of gas over the course of the cycle life test. The absence of gas during room temperature cycling indicates that the gas evolution is thermally activated. More experimental work is needed to determine the origin of gas evolution over cycle life due to fast formation. We provide speculation into the origin of gas evolution as part of the supplemental information.

Our study found no correlations between R_{LS} and the gas amount as measured by pouch thickness. We attribute the lack of correlation primarily to the fact that the cell age was not well-controlled at the time of the pouch thickness measurement: cells stopped cycling anywhere between 0% and 50% capacity retention. Future studies will be needed to confirm the relationship between R_{LS} and gas buildup.

Aging variability

Adopting a new formation protocol in practice also requires a close understanding of the impact of new formation protocols on cell aging variability over life. Cells with non-uniform capacity fade could take longer to balance in a pack and cause a deterioration of energy available at the pack-level.[73] Pack imbalance issues could lead to consumer products being retired earlier, compounding existing battery recycling challenges.[74] Non-uniform cell degradation will also be more difficult to re-purpose into new modules,[75–77] creating higher barriers for pack reuse.

The inter-quartile range (IQR) of cycle lives for fast formation cells was higher than that of baseline formation cells (Figures 1B and 1D). The same result held under both room temperature and 45°C cycling, as well as across different end-of-life definitions (Figure S33), suggesting that fast formation increased aging variability. A key question is whether fast formation created more heterogeneous aging behavior, which caused the higher variability in aging, or if the higher variability is due to the cells lasting longer. To answer this question, we employed the modified signed-likelihood ratio test[78] to check for equality of the coefficients of variation, defined as the ratio between the standard deviation and the mean cycle life. The resulting *p*-values were greater than 0.05 in all cases. Therefore, with the available data, we cannot conclude that fast formation increased the variation in aging beyond the effect of improving cycle life. While a relationship between formation protocol and aging variability may still generally exist, this difference could not be determined with our sample sizes ($n = 10$ cells per group). This result warrants the use of larger samples sizes for future studies on the impact of formation protocol on aging variability.

Conclusion

In this work, we demonstrated that R_{LS} correlates to cycle life across two different battery formation protocols. As a predictive feature, R_{LS} provided higher prediction accuracy compared with conventional measures of formation quality such as CE as well as state-of-the art predictive features based on changes in discharge voltage curves. R_{LS} is measurable at the end of the manufacturing line using ordinary battery test equipment and can be measured within seconds. Changes in R_{LS} are attributed to differences in the amount of lithium consumed to the SEI during formation, where a decrease in R_{LS} indicates that more lithium is consumed. The sensitivity of R_{LS} to lithium consumption is due to the presence of kinetic limitations in the positive electrode causing the total cell resistance to increase at low SOCs. For this reason, R_{LS} provides a particularly strong signature in nickel-rich positive electrode systems where kinetic hindrance plays a strong role in limiting lithium transport toward high states of lithiation. Since the physical interpretation of R_{LS} is general, R_{LS} can be broadly applicable for screening any manufacturing process that impacts the amount of lithium consumed during battery formation. As a whole, our results hold promise for decreasing lithium-ion battery formation time and cost while improving lifetime, as well as identifying rapid diagnostic signals for screening new manufacturing processes and cell designs based on cycle life.

EXPERIMENTAL PROCEDURES

Resource availability

Lead contact

Further information and requests for resources and materials should be directed to and will be fulfilled by Andrew Weng (asweng@umich.edu).

Materials availability

All materials are commercially available, with the exception of the carbon methyl cellulose (CMC) binder material used in the anode formulation, which is proprietary.

Data and code availability

Data and code used in this study are available at Deep Blue Data: https://doi.org/10.7302/pa3f-4w30. The dataset includes raw time-series files exported using Voltaiq (www.voltaiq.com) and files containing post-processed features. Timeseries data covers formation cycling and aging cycles for all cells used in the study.

Supplementary coin cell data used to generate Figures S21 and S22 have also been included. The source code can be accessed at Zenodo: https://doi.org/10.5281/zenodo.5525258. The source code comprises Python modules used to handle raw data parsing and feature extraction ('src/'), IPython Notebooks used for data analysis ('notebooks/'), and MATLAB source files used for the voltage fitting algorithm ('matlab/').

Cell build process

The cathode was comprised of 94:3:3 NMC 111 (TODA North America), C65 conductive additive (Timcal), and polyvinylidene fluoride (PVDF) (Kureha 7208). The slurry was mixed in a step-wise manner, starting with a dry solids homogenization, wetting with n-methyl-2-pyrrolidone (NMP), and then addition of the PVDF resin. The slurry was allowed to mix overnight under static vacuum with agitation from both the double helix blades (30 rpm) and the high-speed disperser blade (1,600 rpm). The final slurry was gravity filtered through a 125 μm paint filter before coating on a roll-to-roll coating machine (Creative & Innovative Systems). The electrode was coated using the reverse comma method at 2 m/min. The final double-sided loading was 34.45 mg/cm^2.

The anode comprised 97:0:(1.5/1.5) graphite (Hitachi MAG-E3), no conductive additive, and equal parts CMC (proprietary) and styrene butadiene rubber (SBR) (Zeon BM-451B). The graphite and pre-dispersed CMC were mixed prior to further letdown with de-ionized water and overnight dispersion under static vacuum and double helix blade agitation (40 rpm). Prior to coating, the SBR was added and mixed in with helical blade agitation for 15 min under active vacuum. The final slurry was gravity filtered through a 125 μm paint filter before coating on a roll-to-roll coating machine (Creative & Innovative Systems). The electrode was coated using the reverse comma technique at 1.5 m/min. The final double-sided loading was 15.7 mg/cm^2.

Both anode and cathode were calendared at room temperature to approximately 30% porosity prior to being transferred to a −40°C dew point dry room for final cell assembly and electrolyte filling. The cells, comprising 7 cathodes and 8 anodes, were z-fold stacked, ultrasonically welded, and sealed into formed pouch material (mPlus). The assembled cells were placed in a vacuum oven at 50°C overnight to fully dry prior to electrolyte addition. Approximately 10.5 g of electrolyte (1.0 M lithium hexafluorophosphate ($LiPF_6$) in 3:7 EC:ethyl methyl carbonate (EMC) v/v + 2wt % vinylene carbonate [VC] from Soulbrain) was manually added to each cell prior to the initial vacuum seal (50 Torr, 5 s). The total mass of all components of the battery is 56.6 $\pm$ 0.3g.

The now-wetted cells were each placed under compression between fiberglass plates held in place using spring-loaded bolts. The compression fixtures are designed to allow the gas pouch to protrude and freely expand in the event of gas generation during formation. All cells were allowed to fully wet for 24 h prior to beginning the formation process.

After formation, the cells were removed from the pressure fixtures, returned to the −40°C dew point dry room and degassed. The degassing process was completed in an mPlus degassing machine, automatically piercing the gas pouch, drawing out any generated gas during the final vacuum seal (50 Torr, 5 s), and then placing the final seal on the cell. Cells are manually trimmed to their final dimensions before being returned to their pressure fixtures.

Please cite this article in press as: Weng et al., Predicting the impact of formation protocols on battery lifetime immediately after manufacturing, Joule (2021), https://doi.org/10.1016/j.joule.2021.09.015

The pouch cell architecture is summarized in Figure S2.

Formation protocols

Figure S1B describes the two different formation protocols used in this study. The fast formation protocol borrows from the "Ultra-fast formation protocol" reported in An et al.[15] and Wood et al.[16] In this protocol, the cell is brought to 3.9 V using a 1 C (2.36 Ah) charge, followed by five consecutive charge-discharge cycles between 3.9 and 4.2 V at C/5, and finally ending on a 1 C discharge to 2.5 V. Each charge step terminates on a CV hold until the current falls below C/100. A C/10 charge and C/10 discharge cycle was appended at the end of the test to measure the post-formation cell discharge capacity. A 6-h step was included in between the C/10 charge-discharge steps to monitor the voltage decay. The formation sequence takes 14 h to complete after excluding time taken for diagnostic steps.

A baseline formation protocol was also implemented, which serves as the control for comparing against the performance of fast formation. This protocol consists of three consecutive C/10 charge-discharge cycles between 3.0 and 4.2 V. A 6-h rest was also added between the final C/10 charge-discharge step to monitor the voltage decay signal. The total formation time was 56 h after excluding the diagnostic steps. Formation was conducted at room temperature for all cells and across both formation protocols.

All formation cycling was conducted on a Maccor Series 4000 cycler (0–5 V, 30 μA - 1A, and auto-ranging). Following formation, one cell (#9) was excluded from this study due to tab weld issues. Consequently, the sample count for the "baseline formation, 45°C" cycling group was decreased to 9. The remaining groups had sample counts of 10.

The mean cell energy measured at a 1 C discharge rate from 4.2 to 3.0 V at room temperature is 8.13 Wh. Full cell level volumetric stack energy density is estimated to be 365 Wh/L based on a volume of 69 mm × 101 mm × 71 mm × 3.2 mm, and the gravimetric stack energy density is estimated to be 144 Wh/kg based on a total cell mass of 56.6 g.

Cycle life testing

Following completion of formation cycling, cells were placed in spring-loaded compression fixtures to maintain a uniform stack pressure. Half of the cells from each formation protocol were placed in a thermal chamber (Espec) with a measured temperature of 44.2°C±0.1°C. The remaining cells were left at room temperature and were exposed to varying temperatures throughout the day (24.5°C±0.6°C). Long-term cycle life testing was conducted on a Maccor Series 4000 cycler (0–5 V, 10 A, auto-ranging). The cycle life test protocol was identical for all cells and consisted of 1 C (2.37 A), constant current (CC) charge to 4.2 V with a CV hold to 10 mA and 1 C discharges to 3.0 V. At every 50 to 100 cycles, the test was interrupted so that a RPT could be performed.[41] The RPT consists of a C/3 charge-discharge cycle, a C/20 charge-discharge cycle, followed by the HPPC protocol.[42] The HPPC test is used to extract 10-s discharge resistance (R_{10s}) as a function of SOC (Figure S8). Every cell was cycled until the discharge capacity was less than 1.18 Ah, corresponding to less than 50% capacity remaining. The total test time varied between 3 to 4 months and the total cycles achieved ranged between 400 and 600 cycles. Cycle test metrics are shown in Figures S3–S6.

Please cite this article in press as: Weng et al., Predicting the impact of formation protocols on battery lifetime immediately after manufacturing, Joule (2021), https://doi.org/10.1016/j.joule.2021.09.015

Statistical significance testing

The standard Student's t test for two samples was used throughout this study to check if differences in measured outcomes between the two different formation protocols were statistically significant. The *p*-value was used to quantify the level of marginal significance within the statistical hypothesis test and represents the probability that the null hypothesis is true. A *p*-value less than 0.05 was used to reject the null hypothesis that the population means are equal. All measured outcomes were assumed to be normally distributed. Box-and-whisker plots are also used throughout the paper to summarize distributions of outcomes. Boxes denote the IQR and whiskers show the minimum and maximum values in the set. No outlier detection methods are employed here due to the small sample sizes ($n < 10$). Finally, the Pearson correlation coefficient, $-1 \leq \rho \leq 1$, was used to determine the significance of correlations between initial state variables and lifetime output variables. $|\rho| > 0.5$ is taken to indicate a statistically meaningful correlation.

Predictive lifetime model

Due to the small number of data points available, the model prediction results are sensitive to which cells are chosen for validation. Therefore, we used nested cross-validation[79] to evaluate the regularized linear regression model on all the data without over-fitting. The nested cross-validation algorithm is as follows: first, we separated the data into 20% "validation" and 80% "train/test." Then, we performed four-fold cross-validation on the "train/test" data to find the optimal regularization strength for ridge regression, α^*, using grid search. Finally, we trained the ridge regression algorithm with regularization strength α^*, using all of the train/test data, and evaluated the error on the validation data. We repeated this process for 1,000 random train-test/validation splits and reported the mean and standard deviation of the mean percent error for each run:

$$\mathrm{MPE}[\%] = \frac{1}{N}\sum_{k=1}^{N}\frac{y_k^{\mathrm{pred}} - y_k^{\mathrm{true}}}{y_k^{\mathrm{true}}}. \qquad \text{(Equation 2)}$$

Each run can select a different optimal regularization strength α^*.

Electrode stoichiometry model

To construct the stoichiometry model shown in Figure 4A, a full cell near-equilibrium potential curve was first extracted using the C/20 charge cycle from the RPT. A randomly selected cell from the 45°C cycling group was selected for this data extraction. Positive and negative electrode near-equilibrium potential curves were adapted from Mohtat et al.[29] The electrode-specific utilization windows are determined by fitting the positive and negative electrode potential curves to match the full cell curve by solving a least squares optimization problem as outlined in Lee et al.[55] The resulting positive and negative electrode alignment minimized the squared error of the modeled versus the measured full cell voltage. The fast formation curve equilibrium potential curve was constructed by shifting the positive electrode curve horizontally and re-computing the full cell voltage curve.

The full cell resistance curves in Figure 4C sourced data from the HPPC sequence as part of the same RPT used to obtain the equilibrium potential curve shown in Figure 4A. A cubic spline fit was used to create smooth resistance curves (a model generated using a linear fit is provided in Figure S24). To break down the resistance contribution into "positive resistance" and "negative + other resistances," a baseline reference resistance R_{ref} was first defined as the minimum measured full cell resistance below 1Ah. The "negative + other resistances" was then assigned a value

of $(1 - f_{pos})$. The remaining resistance was then assigned to the positive electrode. f_{pos} was set to 0.7 to model a generic NMC/graphite system.[15,60,61]

Voltage fitting algorithm

Methods for estimating electrode-specific state of health metrics using half-cell reference curves have been previously reported.[52–54] Here, we applied an automated voltage fitting approach based on work by Lee et al.[55] to extract electrode capacity losses, LAM_{PE} and LAM_{NE}, as well as lithium inventory loss (LLI) for both fresh and aged cells. The input data consisted of C/20 charge curves measured at each RPT. An example set of C/20 charge curves over age is shown in Figure S16.

The method to extract electrode-specific state of health indicators LLI, LAM_{PE}, and LAM_{NE} is adapted from Lee et al.[55] Positive and negative near-equilibrium potential curves were adapted from Mohtat et al.[29] The curves were obtained at the C/20 rate and served as proxies for the true equilibrium potential curves. The same equilibrium potential curves were used to model data at both test temperatures.

To prevent over-fitting, the positive electrode stoichiometry at 100% SOC (y_{100}) was fixed to 0.03 at every instance for this analysis. Fixing this value yielded smoother and more physical degradation trajectories over cycle life. Figure S17 shows an example of voltage fitting results for a single cell. The degradation metrics, including LLI and LAM were computed in the usual manner (see Lee et al.[55] for more details).

Hybrid pulse power characterization of half cells

Coin cell half cells were built with LFP, NMC111, and graphite as the working electrode and lithium metal as the counter electrode. The NMC material used were identical to that used in the pouch cells for the formation experiments (TODA North America). The graphite material used differed from the ones used in the pouch cells. The coin cell construction consisted of 2032 form factor components including a wavespring and spacer. The electrolyte used was 1 M $LiPF_6$ with EC/EMC. The lithium counter electrode was 16 mm in diameter, the separator was 19 mm in diameter, and the working electrodes were 14 mm in diameter. Working electrodes were measured to be approximately 60 μm thick and the lithium counter electrodes were approximately 750 μm thick. Working electrodes were single-side coated. Calculated theoretical capacities for the NMC111, LFP, and graphite cells were 2.0, 2.9, and 4.6 mAh, respectively.

The HPPC protocol was adapted for the coin cells. Potential ranges were modified depending on the working electrode. The currents used in the pulses were also scaled down to 0.4 mA for all cells (Figure S21). The measured resistance drop includes a large Ohmic contribution due to the presence of the lithium metal counter electrode. However, since this counter electrode was present in all cells, differences in measured, SOC-dependent resistances between the different cells remain meaningful. All coin cells were pre-conditioned using at least three slow charge-discharge cycles prior to starting the HPPC sequence.

SUPPLEMENTAL INFORMATION

Supplemental information can be found online at https://doi.org/10.1016/j.joule.2021.09.015.

ACKNOWLEDGMENTS

This work was supported by the National Science Foundation, grant number 176224, and the University of Michigan Battery Laboratory. The authors acknowledge Voltaiq

(www.voltaiq.com) for providing software that made it easy to remotely monitor cycle life test data during the COVID-19 pandemic in 2020. The authors also thank Joseph Gallegos for building the coin cells for the study.

AUTHOR CONTRIBUTIONS

Conceptualization, A.W. and A.S.; methodology, A.W., P.M., G.L., P.M.A., V.S., and S.L.; investigation, A.W. and G.L.; data curation, A.W; software, A.W.; visualization, A.W.; formal analysis, V.S.; writing – original draft, A.W.; writing – review & editing, A.W., P.M.A., and A.S.; funding acquisition, A.S.

DECLARATION OF INTERESTS

A.W. and P.M.A. are employees of Tesla. A patent application relating to this work has been filed. The authors declare no other competing interests.

Received: July 7, 2021
Revised: August 9, 2021
Accepted: September 28, 2021
Published: October 21, 2021

REFERENCES

1. Australian Trade; Investment Commission (2018). The lithium-ion battery value chain: new economy opportunities for Australia, Technical report ((Australian Trade and Investment Commission)). https://apo.org.au/node/210341.

2. Benchmark minerals intelligence. (2019). EV battery arms race enters new gear with 115 megafactories, Europe sees most rapid growth. https://www.benchmarkminerals.com/ev-battery-arms-race-enters-new-gear-with-115-megafactories-europe-sees-most-rapid-growth/.

3. Wood Mackenzie. (2020). Global lithium-ion cell manufacturing capacity to quadruple to 1.3 TWh by 2030. https://www.woodmac.com/press-releases/global-lithium-ion-cell-manufacturing-capacity-to-quadruple-to-1.3-twh-by-2030/.

4. Liu, Y., Zhang, R., Wang, J., and Wang, Y. (2021). Current and future lithium-ion battery manufacturing. iScience *24*, 102332. https://doi.org/10.1016/j.isci.2021.102332.

5. Nelson, P.A., Gallagher, K.G., Bloom, I., and Dees, D.W. (2011). Modeling the performance and cost of lithium-ion batteries for electric-drive vehicles (Argonne National Laboratory). https://publications.anl.gov/anlpubs/2011/10/71302.pdf.

6. Duffner, F., Mauler, L., Wentker, M., Leker, J., and Winter, M. (2021). Large-scale automotive battery cell manufacturing: analyzing strategic and operational effects on manufacturing costs. Int. J. Prod. Econ. *232*, 107982. https://doi.org/10.1016/j.ijpe.2020.107982.

7. Küpper, D., Kuhlmann, K., Wolf, S., Pieper, C., Xu, G., and Ahmad, J. (2018). The future of battery production for electric vehicles, Technical report. https://www.bcg.com/publications/2018/future-battery-production-electric-vehicles.

8. Wood, D.L., Li, J., and Daniel, C. (2015). Prospects for reducing the processing cost of lithium ion batteries. J. Power Sources *275*, 234–242. https://doi.org/10.1016/j.jpowsour.2014.11.019.

9. Winter, M. (2009). The solid electrolyte interphase - the most important and the least understood solid electrolyte in rechargeable Li batteries. Z. Phys. chem. *223*, 1395–1406. https://doi.org/10.1524/zpch.2009.6086.

10. An, S.J., Li, J., Daniel, C., Mohanty, D., Nagpure, S., and Wood, D.L. (2016). The state of understanding of the lithium-ion-battery graphite solid electrolyte interphase (SEI) and its relationship to formation cycling. Carbon *105*, 52–76. https://doi.org/10.1016/j.carbon.2016.04.008.

11. Wang, A., Kadam, S., Li, H., Shi, S., and Qi, Y. (2018). Review on modeling of the anode solid electrolyte interphase (SEI) for lithium-ion batteries. NPJ Comput. Mater. *4*. https://doi.org/10.1038/s41524-018-0064-0.

12. Peled, E., and Menkin, S. (2017). Review—SEI: past, present and future. J. Electrochem. Soc. *164*, A1703–A1719. https://doi.org/10.1149/2.1441707jes.

13. Goers, D., Spahr, M.E., Leone, A., Märkle, W., and Novák, P. (2011). The influence of the local current density on the electrochemical exfoliation of graphite in lithium-ion battery negative electrodes. Electrochim. Acta *56*, 3799–3808. https://doi.org/10.1016/j.electacta.2011.02.046.

14. Lu, P., Li, C., Schneider, E.W., and Harris, S.J. (2014). Chemistry, impedance, and morphology evolution in solid electrolyte interphase films during formation in lithium ion batteries. J. Phys. Chem. C *118*, 896–903. https://doi.org/10.1021/jp4111019.

15. An, S.J., Li, J., Du, Z., Daniel, C., and Wood, D.L. (2017). Fast formation cycling for lithium ion batteries. J. Power Sources *342*, 846–852. https://doi.org/10.1016/j.jpowsour.2017.01.011.

16. Wood, D.L., Li, J., and An, S.J. (2019). Formation challenges of Lithium-Ion Battery Manufacturing. Joule *3*, 2884–2888. https://doi.org/10.1016/j.joule.2019.11.002.

17. Mao, C., An, S.J., Meyer, H.M., Li, J., Wood, M., Ruther, R.E., and Wood, D.L. (2018). Balancing formation time and electrochemical performance of high energy lithium-ion batteries. J. Power Sources *402*, 107–115. https://doi.org/10.1016/j.jpowsour.2018.09.019.

18. Müller, V., Kaiser, R., Poller, S., Sauerteig, D., Schwarz, R., Wenger, M., Lorentz, V.R.H., and März, M. (2017). Introduction and application of formation methods based on serial-connected lithium-ion battery cells. J. Energy Storage *14*, 56–61. https://doi.org/10.1016/j.est.2017.09.013.

19. Antonopoulos, B.K., Stock, C., Maglia, F., and Hoster, H.E. (2018). Solid electrolyte interphase: can faster formation at lower potentials yield better performance? Electrochim. Acta *269*, 331–339. https://doi.org/10.1016/j.electacta.2018.03.007.

20. Zhang, S.S., Xu, K., and Jow, T.R. (2004). Optimization of the forming conditions of the solid-state interface in the Li-ion batteries. J. Power Sources *130*, 281–285. https://doi.org/10.1016/j.jpowsour.2003.12.012.

21. Heimes, H.H., Offermanns, C., Mohsseni, A., Laufen, H., Westerhoff, U., Hoffmann, L., Niehoff, P., Kurrat, M., Winter, M., and Kampker, A. (2020). The effects of mechanical and thermal loads during lithium-ion pouch cell formation and their impacts on process time. Energy Technol *8*, 1900118. https://doi.org/10.1002/ente.201900118.

22. Münster, P., Diehl, M., Frerichs, J.E., Börner, M., Hansen, M.R., Winter, M., and Niehoff, P. (2021). Effect of Li plating during formation of

lithium ion batteries on their cycling performance and thermal safety. J. Power Sources *484*, 229306. https://doi.org/10.1016/j.jpowsour.2020.229306.

23. Pathan, T.S., Rashid, M., Walker, M., Widanage, W.D., and Kendrick, E. (2019). Active formation of Li-ion batteries and its effect on cycle life. J. Phys. *1*, 044003. https://doi.org/10.1088/2515-7655/ab2e92.

24. Müller, V., Kaiser, R., Poller, S., and Sauerteig, D. (2018). Importance of the constant voltage charging step during lithium-ion cell formation. J. Energy Storage *15*, 256–265. https://doi.org/10.1016/j.est.2017.11.020.

25. Rago, N.D., Basco, J.K., Vu, A., Li, J., Hays, K., Sheng, Y., Wood, D.L., and Bloom, I. (2019). Effect of formation protocol: cells containing Si-graphite composite electrodes. J. Power Sources *435*, 126548. https://doi.org/10.1016/j.jpowsour.2019.04.076.

26. Lee, H.-H., Wang, Y.-Y., Wan, C.-C., Yang, M.-H., Wu, H.-C., and Shieh, D.-T. (2004). A fast formation process for lithium batteries. J. Power Sources *134*, 118–123. https://doi.org/10.1016/j.jpowsour.2004.03.020.

27. Wang, X., Sone, Y., Segami, G., Naito, H., Yamada, C., and Kibe, K. (2007). Understanding volume change in lithium-ion cells during charging and discharging using in situ measurements. J. Electrochem. Soc. *154*, A14. https://doi.org/10.1149/1.2386933.

28. Bauer, M., Wachtler, M., Stöwe, H., Persson, J.V., and Danzer, M.A. (2016). Understanding the dilation and dilation relaxation behavior of graphite-based lithium-ion cells. J. Power Sources *317*, 93–102. https://doi.org/10.1016/j.jpowsour.2016.03.078.

29. Mohtat, P., Lee, S., Sulzer, V., Siegel, J.B., and Stefanopoulou, A.G. (2020). Differential expansion and voltage model for Li-ion batteries at practical charging rates. J. Electrochem. Soc. *167*, 110561. https://doi.org/10.1149/1945-7111/aba5d1.

30. Zhang, Y.Y., Tang, Q., Zhang, Y.Y., Wang, J., Stimming, U., and Lee, A.A. (2020). Identifying degradation patterns of lithium ion batteries from impedance spectroscopy using machine learning. Nat. Commun. *11*, 1706. https://doi.org/10.1038/s41467-020-15235-7.

31. Bommier, C., Chang, W., Lu, Y., Yeung, J., Davies, G., Mohr, R., Williams, M., and Steingart, D. (2020). In Operando acoustic detection of lithium metal plating in commercial LiCoO2/Graphite pouch cells. Cell Rep. Phys. Sci. *1*, 100035. https://doi.org/10.1016/j.xcrp.2020.100035.

32. Davies, G., Knehr, K.W., Van Tassell, B., Hodson, T., Biswas, S., Hsieh, A.G., and Steingart, D.A. (2017). State of charge and state of health estimation using electrochemical acoustic time of flight analysis. J. Electrochem. Soc. *164*, A2746–A2755. https://doi.org/10.1149/2.1411712jes.

33. Knehr, K.W., Hodson, T., Bommier, C., Davies, G., Kim, A., and Steingart, D.A. (2018). Understanding full-cell evolution and non-chemical electrode crosstalk of Li-ion batteries. Joule *2*, 1146–1159. https://doi.org/10.1016/j.joule.2018.03.016.

34. Deng, Z., Hu, X., Lin, X., Xu, L., Che, Y., and Hu, L. (2020). General discharge voltage information enabled health evaluation for lithium-ion batteries. IEEE/ASME Trans. Mechatron. *26*, 1295–1306. https://doi.org/10.1109/TMECH.2020.3040010.

35. Pietsch, P., and Wood, V. (2017). X-ray tomography for lithium ion battery research: a practical guide. Annu. Rev. Mater. Res. *47*, 451–479. https://doi.org/10.1146/annurev-matsci-070616-123957.

36. Wood, V. (2018). X-ray tomography for battery research and development. Nat. Rev. Mater. *3*, 293–295. https://doi.org/10.1038/s41578-018-0053-4.

37. An, S.J., Park, J.Y., Song, J., Lee, J., Kim, G.H., Yoon, J., and Oh, B. (2020). A fast method for evaluating stability of lithium ion batteries at high C-rates. J. Power Sources *480*, 228856. https://doi.org/10.1016/j.jpowsour.2020.228856.

38. Attia, P.M., Harris, S.J., and Chueh, W.C. (2021). Benefits of fast battery formation in a model system. J. Electrochem. Soc. *168*, 050543. https://doi.org/10.1149/1945-7111/abff35.

39. Kim, S.-P., van Duin, A.C.T., and Shenoy, V.B. (2011). Effect of electrolytes on the structure and evolution of the solid electrolyte interphase (SEI) in Li-ion batteries: a molecular dynamics study. J. Power Sources *196*, 8590–8597. https://doi.org/10.1016/j.jpowsour.2011.05.061.

40. Zhang, S., Ding, M.S., Xu, K., Allen, J., and Jow, T.R. (2001). Understanding solid electrolyte interface film formation on graphite electrodes. Electrochem. Solid-State Lett. *4*, 206–209. https://doi.org/10.1149/1.1414946.

41. Dubarry, M., and Baure, G. (2020). Perspective on commercial Li-ion battery testing, best practices for simple and effective protocols. Electronics *9*, 206. https://doi.org/10.3390/electronics9010152.

42. Christopherson, J.P. (2015). Battery test manual for plug-in hybrid electric vehicles, Tech. rep. (Idaho National Laboratory) https://www.osti.gov/biblio/1186745-battery-test-manual-electric-vehicles-revision.

43. Dahn, J.R. (1991). Phase diagram of LixC6. Phys. Rev. B *44*, 9170–9177.

44. Smith, A.J., Burns, J.C., Xiong, D., and Dahn, J.R. (2011). Interpreting high precision coulometry results on Li-ion cells. J. Electrochem. Soc. *158*, A1136–A1142. https://doi.org/10.1149/1.3625232.

45. Fathi, R., Burns, J.C., Stevens, D.A., Ye, H., Hu, C., Jain, G., Scott, E., Schmidt, C., and Dahn, J.R. (2014). Ultra high-precision studies of degradation mechanisms in aged LiCoO 2 /graphite Li-ion cells. J. Electrochem. Soc. *161*, A1572–A1579. https://doi.org/10.1149/2.0321410jes.

46. Severson, K.A., Attia, P.M., Jin, N., Perkins, N., Jiang, B., Yang, Z., Chen, M.H., Aykol, M., Herring, P.K., Fraggedakis, D., et al. (2019). Data-driven prediction of battery cycle life before capacity degradation. Nat. Energy *4*, 383–391. https://doi.org/10.1038/s41560-019-0356-8.

47. Edström, K., Herstedt, M., and Abraham, D.P. (2006). A new look at the solid electrolyte interphase on graphite anodes in Li-ion batteries. J. Power Sources *153*, 380–384. https://doi.org/10.1016/j.jpowsour.2005.05.062.

48. Lu, P., and Harris, S.J. (2011). Lithium transport within the solid electrolyte interphase. Electrochem. Commun. *13*, 1035–1037. https://doi.org/10.1016/j.elecom.2011.06.026.

49. Burns, J.C., Kassam, A., Sinha, N.N., Downie, L.E., Solnickova, L., Way, B., and Dahn, J.R. (2013). Predicting and extending the lifetime of Li-ion batteries. J. Electrochem. Soc. *160*, A1451–A1456. https://doi.org/10.1149/2.060309jes.

50. Reniers, J.M., Mulder, G., and Howey, D.A. (2019). Review and performance comparison of mechanical-chemical degradation models for lithium-ion batteries. J. Electrochem. Soc. *166*, A3189–A3200. https://doi.org/10.1149/2.0281914jes.

51. Yang, X.-G., Leng, Y., Zhang, G., Ge, S., and Wang, C.-Y. (2017). Modeling of lithium plating induced aging of lithium-ion batteries: transition from linear to nonlinear aging. J. Power Sources *360*, 28–40. https://doi.org/10.1016/j.jpowsour.2017.05.110.

52. Bloom, I., Jansen, A.N., Abraham, D.P., Knuth, J., Jones, S.A., Battaglia, V.S., and Henriksen, G.L. (2005). Differential voltage analyses of high-power, lithium-ion cells 1. Technique and application. J. Power Sources *139*, 295–303. https://doi.org/10.1016/j.jpowsour.2004.07.021.

53. Dubarry, M., Truchot, C., and Liaw, B.Y. (2012). Synthesize battery degradation modes via a diagnostic and prognostic model. J. Power Sources *219*, 204–216. https://doi.org/10.1016/j.jpowsour.2012.07.016.

54. Dubarry, M., Berecibar, M., Devie, A., Anseán, D., Omar, N., and Villarreal, I. (2017). State of health battery estimator enabling degradation diagnosis: model and algorithm description. J. Power Sources *360*, 59–69. https://doi.org/10.1016/j.jpowsour.2017.05.121.

55. Lee, S., Siegel, J.B., Stefanopoulou, A.G., Lee, J.-W., and Lee, T.-K. (2020). Electrode state of health estimation for lithium ion batteries considering half-cell potential change due to aging. J. Electrochem. Soc. *167*, 090531. https://doi.org/10.1149/1945-7111/ab8c83.

56. Yang, S., Wang, X., Yang, X., Bai, Y., Liu, Z., Shu, H., and Wei, Q. (2012). Determination of the chemical diffusion coefficient of lithium ions in spherical Li[Ni0.5Mn0.3Co0.2]O2. Electrochim. Acta *66*, 88–93. https://doi.org/10.1016/j.electacta.2012.01.061.

57. Zhou, H., Xin, F., Pei, B., and Whittingham, M.S. (2019). What limits the capacity of layered oxide cathodes in lithium batteries? ACS Energy Lett *4*, 1902–1906. https://doi.org/10.1021/acsenergylett.9b01236.

58. Liu, A., Phattharasupakun, N., Cormier, M.M.E., Zsoldos, E., Zhang, N., Lyle, E., Arab, P., Sawangphruk, M., and Dahn, J.R. (2021). Factors that affect capacity in the low voltage kinetic hindrance region of Ni-Rich positive

electrode materials and diffusion measurements from a reinvented approach. J. Electrochem. Soc. *168*, 070503. https://doi.org/10.1149/1945-7111/ac0d69.

59. An, S.J., Li, J., Daniel, C., Kalnaus, S., and Wood, D.L. (2017). Design and demonstration of three-electrode pouch cells for lithium-ion batteries. J. Electrochem. Soc. *164*, A1755–A1764. https://doi.org/10.1149/2.0031709jes.

60. Abraham, D.P. (2005). Diagnostic examination of generation 2 lithium-ion cells and assessment of performance degradation mechanisms, Prepared by chemical engineering division. Technical report (Argonne National Laboratory). https://publications.anl.gov/anlpubs/2005/07/53944.pdf.

61. Wu, Q., Lu, W., and Prakash, J. (2000). Characterization of a commercial size cylindrical Li-ion cell with a reference electrode. J. Power Sources *88*, 237–242. https://doi.org/10.1016/S0378-7753(00)00372-4.

62. Plett, G.L. (2015). Battery Management Systems Volume I: Battery Modeling (Artech House).

63. Watanabe, S., Kinoshita, M., Hosokawa, T., Morigaki, K., and Nakura, K. (2014). Capacity fade of LiAlyNi1-x-yCoxO 2 cathode for lithium-ion batteries during accelerated calendar and cycle life tests (surface analysis of LiAlyNi1-x-yCo xO2 cathode after cycle tests in restricted depth of discharge ranges). J. Power Sources *258*, 210–217. https://doi.org/10.1016/j.jpowsour.2014.02.018.

64. Yan, P., Zheng, J., Gu, M., Xiao, J., Zhang, J.-G., and Wang, C.-M. (2017). Intragranular cracking as a critical barrier for high-voltage usage of layer-structured cathode for lithium-ion batteries. Nat. Commun. *8*, 14101. https://doi.org/10.1038/ncomms14101.

65. Zhang, S.S. (2020). Problems and their origins of Ni-rich layered oxide cathode materials. Energy Storage Mater. *24*, 247–254. https://doi.org/10.1016/j.ensm.2019.08.013.

66. Takahashi, K., and Srinivasan, V. (2015). Examination of graphite particle cracking as a failure mode in lithium-ion batteries: a model-experimental study. J. Electrochem. Soc. *162*, A635–A645. https://doi.org/10.1149/2.0281504jes.

67. Kupper, C., Weißhar, B., Rißmann, S., and Bessler, W.G. (2018). End-of-life prediction of a lithium-ion battery cell based on mechanistic aging models of the graphite electrode. J. Electrochem. Soc. *165*, A3468–A3480. https://doi.org/10.1149/2.0941814jes.

68. Taleghani, S.T., Marcos, B., Zaghib, K., and Lantagne, G. (2017). A study on the effect of porosity and particles size distribution on Li-ion battery performance. J. Electrochem. Soc. *164*, E3179–E3189. https://doi.org/10.1149/2.0211711jes.

69. Mohanty, D., Dahlberg, K., King, D.M., David, L.A., Sefat, A.S., Wood, D.L., Daniel, C., Dhar, S., Mahajan, V., Lee, M., and Albano, F. (2016). Modification of Ni-Rich FCG NMC and NCA cathodes by atomic layer deposition: preventing surface phase transitions for high-voltage lithium-ion batteries. Sci. Rep. *6*, 26532. https://doi.org/10.1038/srep26532.

70. Jin, Y., Zhu, B., Lu, Z., Liu, N., and Zhu, J. (2017). Challenges and recent progress in the development of Si anodes for lithium-ion battery. Adv. Energy Mater. *7*, 1700715. https://doi.org/10.1002/aenm.201700715.

71. Xiao, J., Li, Q., Bi, Y., Cai, M., Dunn, B., Glossmann, T., Liu, J., Osaka, T., Sugiura, R., Wu, B., et al. (2020). Understanding and applying coulombic efficiency in lithium metal batteries. Nat. Energy *5*, 561–568. https://doi.org/10.1038/s41560-020-0648-z.

72. Sun, P., Bisschop, R., Niu, H., and Huang, X. (2020). A review of battery fires in electric vehicles. Fire Technol. *56*, 1361–1410. https://doi.org/10.1007/s10694-019-00944-3.

73. Liu, X., Ai, W., Naylor Marlow, M., Patel, Y., and Wu, B. (2019). The effect of cell-to-cell variations and thermal gradients on the performance and degradation of lithium-ion battery packs. Appl. Energy *248*, 489–499. https://doi.org/10.1016/j.apenergy.2019.04.108.

74. Harper, G., Sommerville, R., Kendrick, E., Driscoll, L., Slater, P., Stolkin, R., Walton, A., Christensen, P., Heidrich, O., Lambert, S., et al. (2019). Recycling lithium-ion batteries from electric vehicles. Nature *575*, 75–86. https://doi.org/10.1038/s41586-019-1682-5.

75. Engel, H., Hertzke, P., and Siccardo, G. (2019). Second-life EV batteries: the newest value pool in energy storage, Technical Report. https://www.mckinsey.com/industries/automotive-and-assembly/our-insights/second-life-ev-batteries-the-newest-value-pool-in-energy-storage.

76. Rumpf, K., Rheinfeld, A., Schindler, M., Keil, J., Schua, T., and Jossen, A. (2018). Influence of cell-to-cell variations on the inhomogeneity of lithium-ion battery modules. J. Electrochem. Soc. *165*, A2587–A2607. https://doi.org/10.1149/2.0111811jes.

77. Rasheed, M., Kamel, M., Wang, H., Zane, R., and Smith, K. (2020). Investigation of active life balancing to recondition Li-ion battery packs for 2ndLife. In 2020 IEEE 21st Workshop on Control and Modeling for Power Electronics (COMPEL 2020), pp. 1–7. https://doi.org/10.1109/COMPEL49091.2020.9265808.

78. Krishnamoorthy, K., and Lee, M. (2014). Improved tests for the equality of normal coefficients of variation. Comput. Stat. *29*, 215–232. https://doi.org/10.1007/s00180-013-0445-2.

79. Krstajic, D., Buturovic, L.J., Leahy, D.E., and Thomas, S. (2014). Cross-validation pitfalls when selecting and assessing regression and classification models. J. Cheminform. *6*, 10. https://doi.org/10.1186/1758-2946-6-10.

Joule, Volume *5*

Supplemental information

Predicting the impact of formation protocols on battery lifetime immediately after manufacturing

Andrew Weng, Peyman Mohtat, Peter M. Attia, Valentin Sulzer, Suhak Lee, Greg Less, and Anna Stefanopoulou

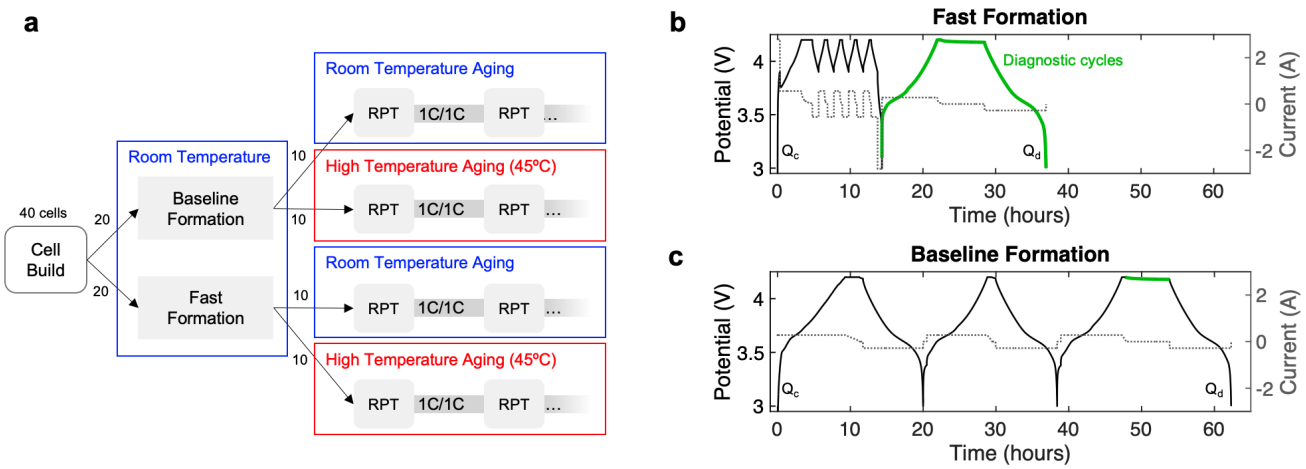

Figure S1. Experimental Design
(a) Distribution of cells across two formation protocols and two aging temperatures. The aging test consists of 1C charge/discharge cycles between 3.0V and 4.2V, with reference performance tests (RPTs) inserted periodically into the test. (b, c) Voltage and current versus time profiles for (b) fast formation and (c) baseline formation. Green lines show diagnostic steps inserted into the formation protocols for the purpose of this study only. The diagnostic cycles are not considered to be part of the formation protocol. Ignoring the diagnostic cycles, the fast formation protocol lasts 14 hours and the baseline formation protocol lasts 56 hours.

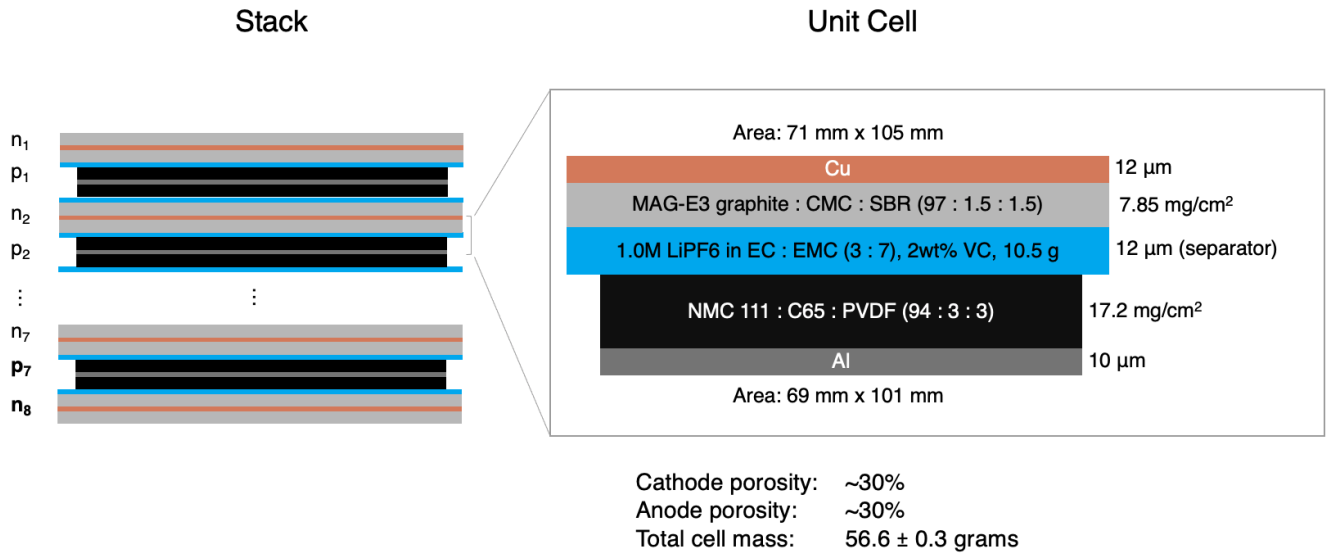

Figure S2. Pouch Cell Architecture
Left: cell stack definition. Right: unit cell definition. The same cell architecture is used for all cells in this study.

	Dimensions	72 mm x 110 mm
	Stack (pos/neg)	7/8
Positive	Chemistry	NMC111
	Composition	NMC111 : C65 : PVDF
	Ratio	94 : 3 : 3
	Loading (double-sided)	34.45 mg/cm^2
	Collector thickness	12 um
Negative	Chemistry	Graphite
	Composition	MAG-E3 : CMC : SBR
	Ratio	97 : 1.5 : 1.5
	Loading (double-sided)	15.7 mg/cm^2
	Collector thickness	10 um
Electrolyte	Salt	1.0 M $LiPF_6$
	Solvent	EC : EMC (3 : 7)
	Additive	2 wt% VC, 4g/Ah
	Mass	10.55 g
Separator	Supplier	Entek
	Thickness	12 um

Table S1. Cell Design Parameters

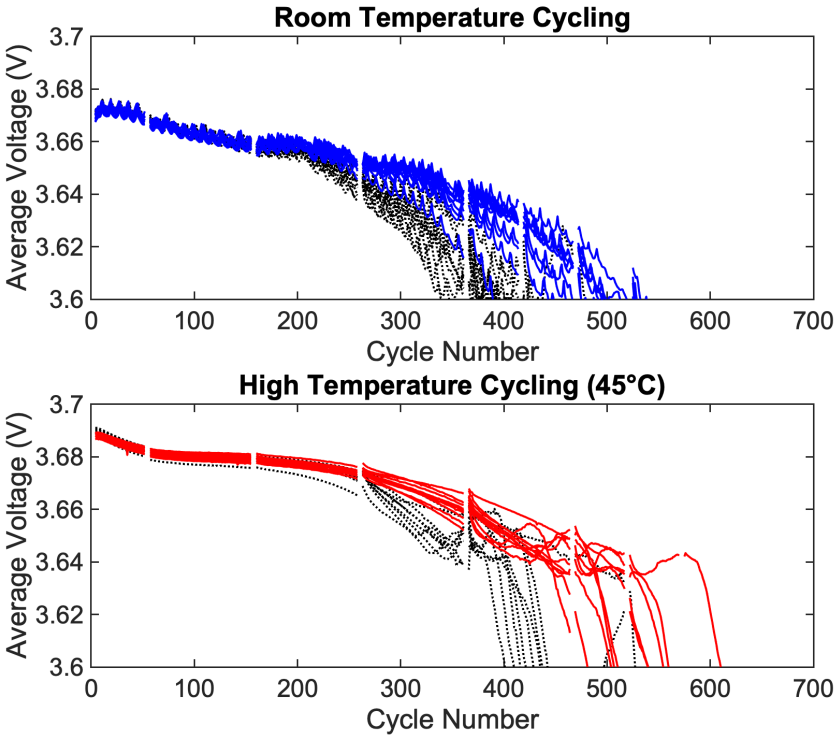

Figure S3. Mean Discharge Voltage Over Cycle Number

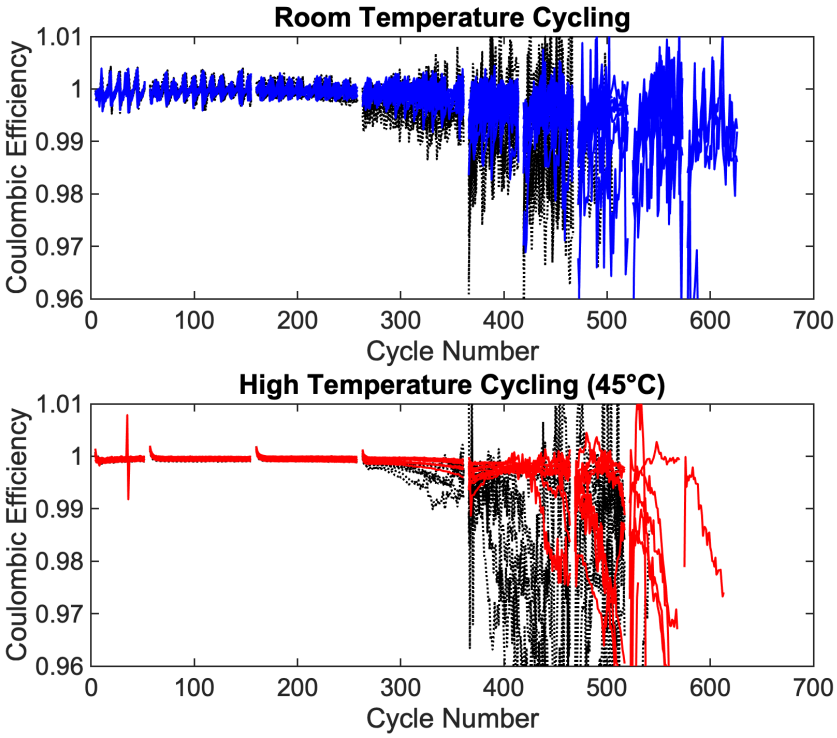

Figure S4. Coulombic Efficiency Over Cycle Number

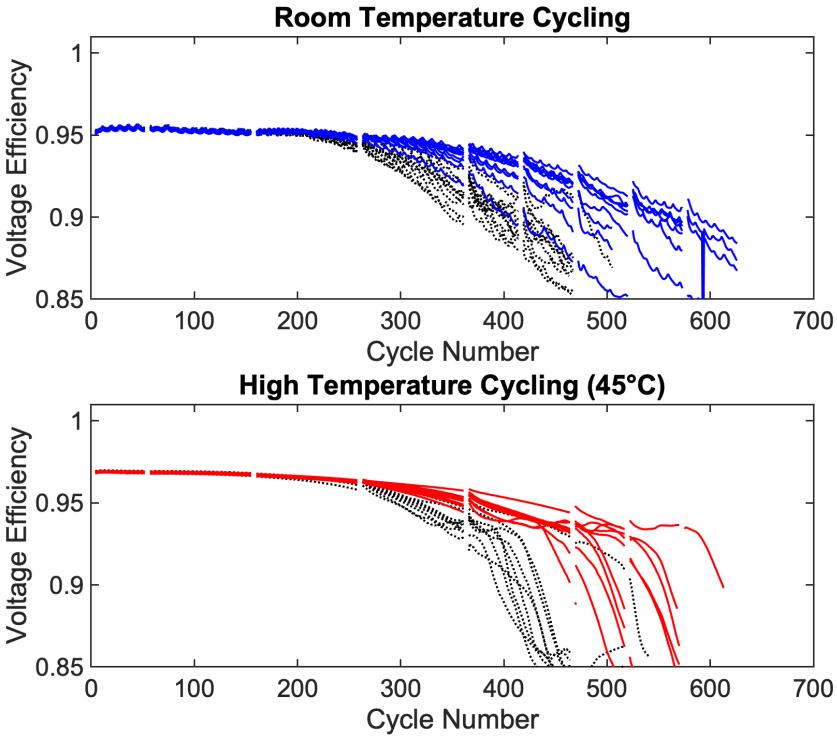

Figure S5. Voltage Efficiency Over Cycle Number

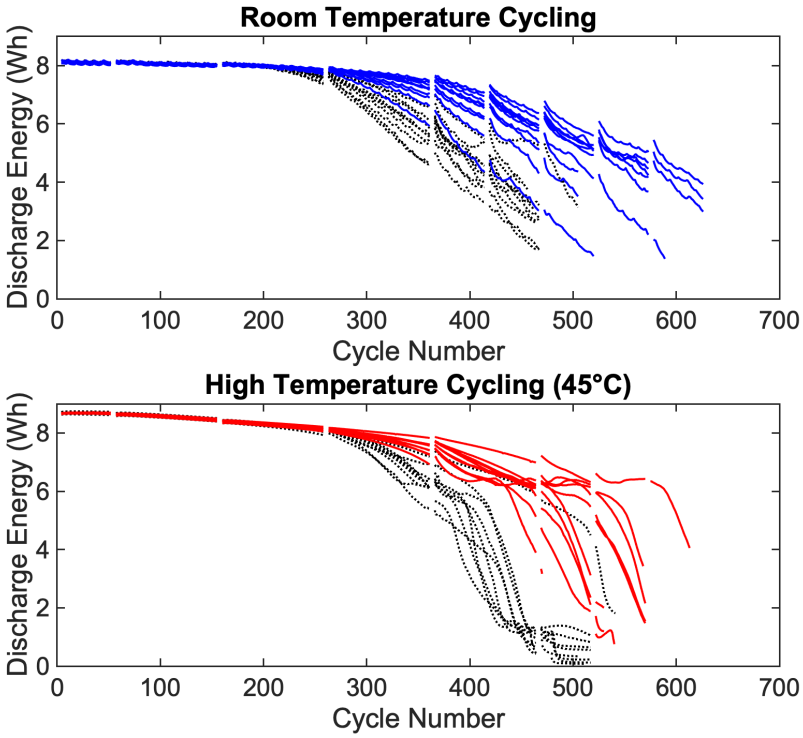

Figure S6. Discharge Energy Over Cycle Number

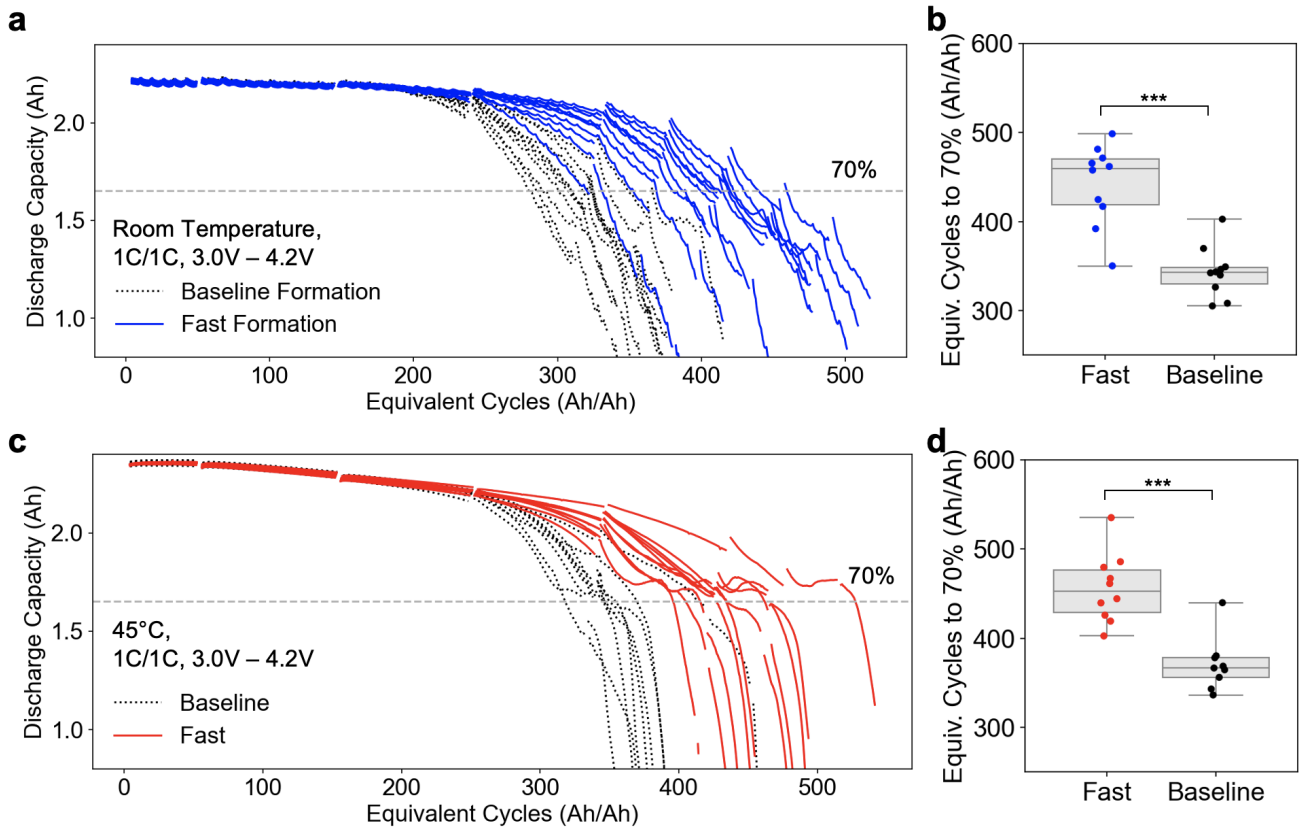

Figure S7. Cycle Life Test Results Plotted With Equivalent Cycles (Ah/Ah) as the Throughput Basis
The total throughput is calculated by taking the cumulative discharge capacity and dividing by the cell nominal capacity (2.36 Ah). (a,c) Discharge capacity for the room temperature (a) and 45℃ (c) tests. (b,d) Distribution of outcomes at the end of life for the room temperature (b) and 45℃ (d) tests. End of life is defined as equivalent cycles to reach 70% of initial capacity.

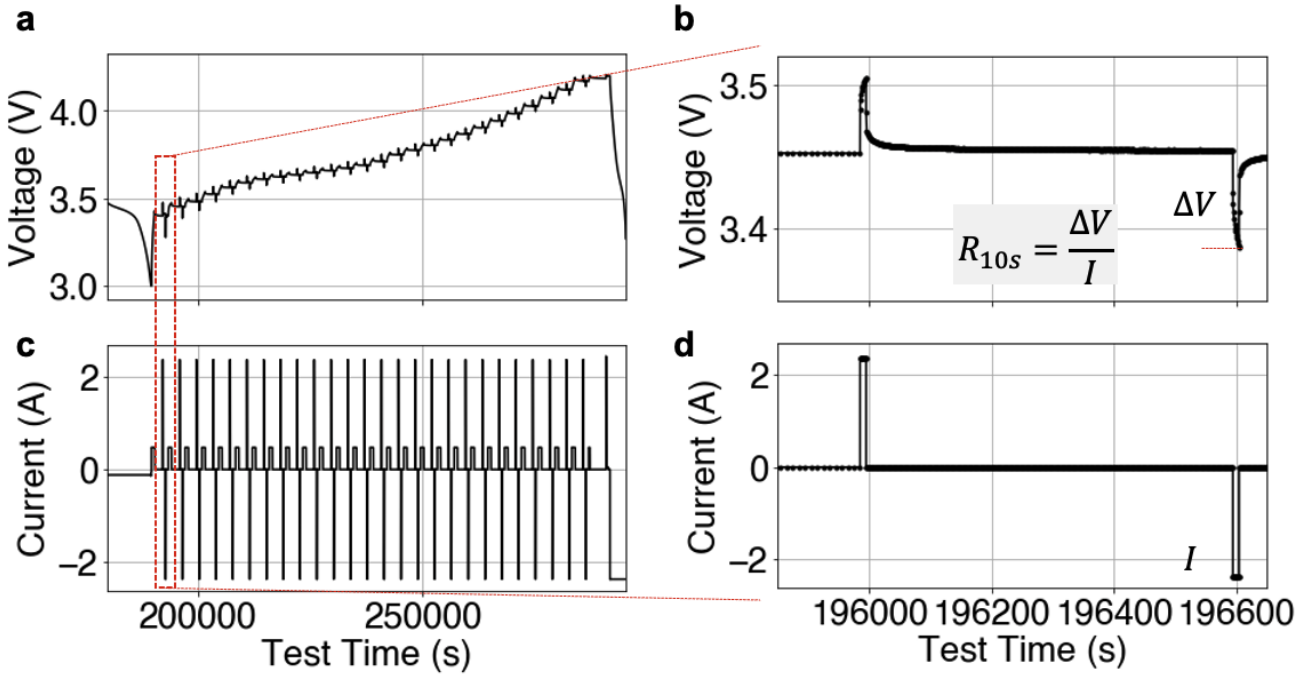

Figure S8. Example Hybrid Power Pulse Characterization (HPPC) Sequence
HPPC is used to extract the 1C, 10-second charge and discharge resistances across different SOCs. (a,c) current and voltage traces from the HPPC protocol. (b,d) magnified view of the first charge and discharge pulse from the pulse sequence, which occurs at ~4% SOC. The HPPC pulses are included as part of every reference performance test (RPT).

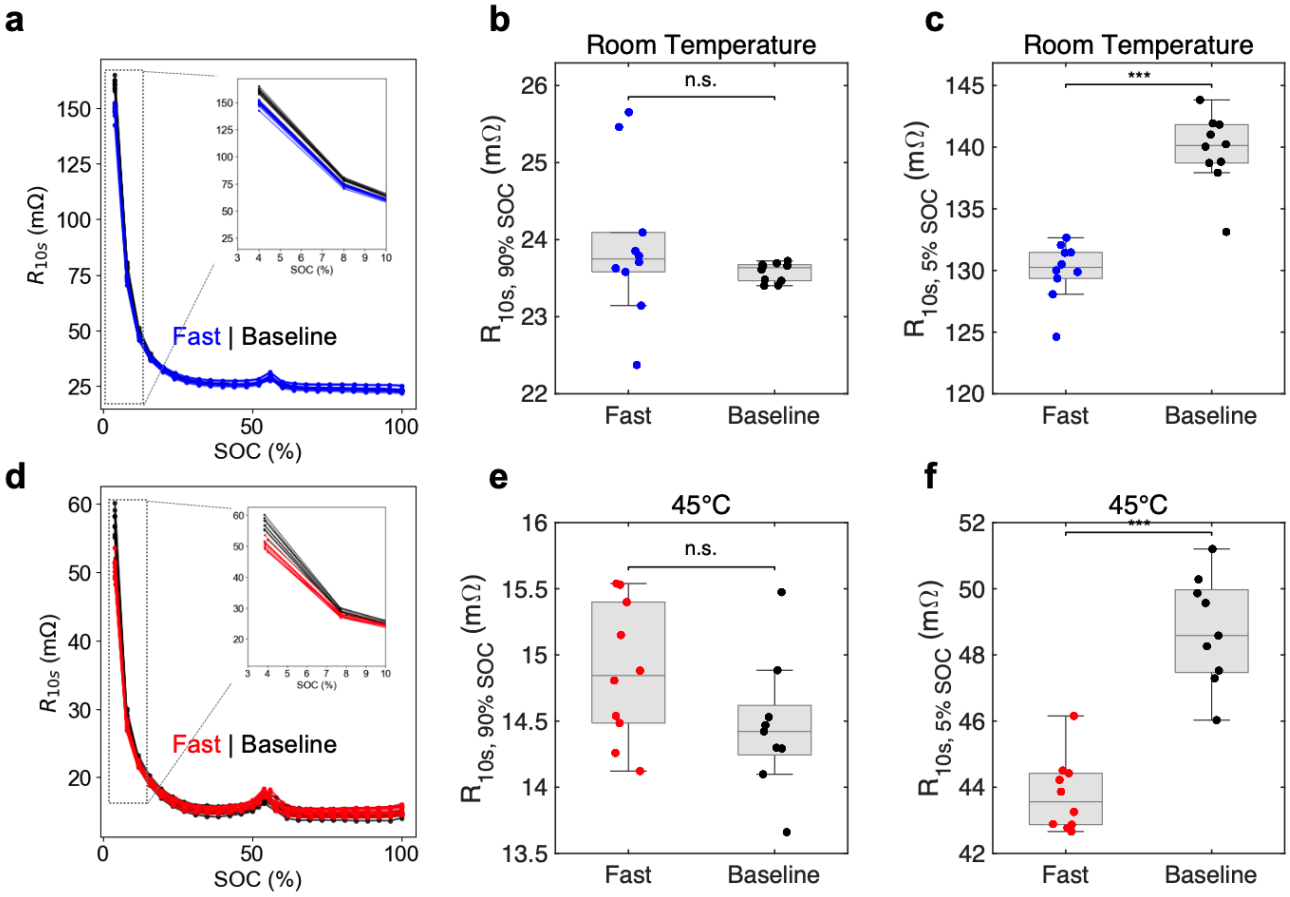

Figure S9. Initial Cell Resistance Comparison
Distribution of resistance measured at (a-c) room temperature and (d-f) 45℃. Resistance is calculated from the Hybrid Power Pulse Characterization (HPPC) test from the first RPT. 'n.s.': not statistically significant. '***': statistically significant with p-value < 0.001.

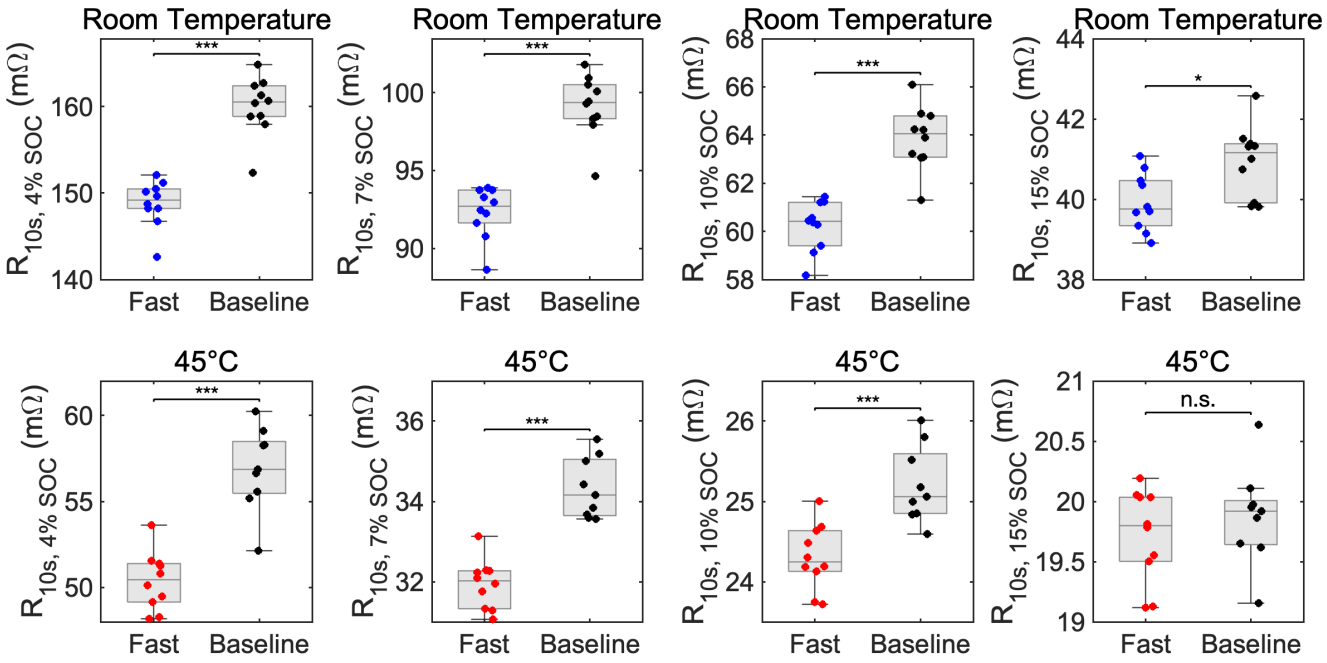

Figure S10. Effect of Measurement SOC on the Cell Resistance Measured from HPPC
Top row: room temperature. Bottom row: 45℃. Values are obtained from the initial Reference Performance Test (RPT) run prior to the start of cycling. 'n.s.': not statistically significant. '***': statistically significant with p-value < 0.001. '*': statistically significant with p-value < 0.05.

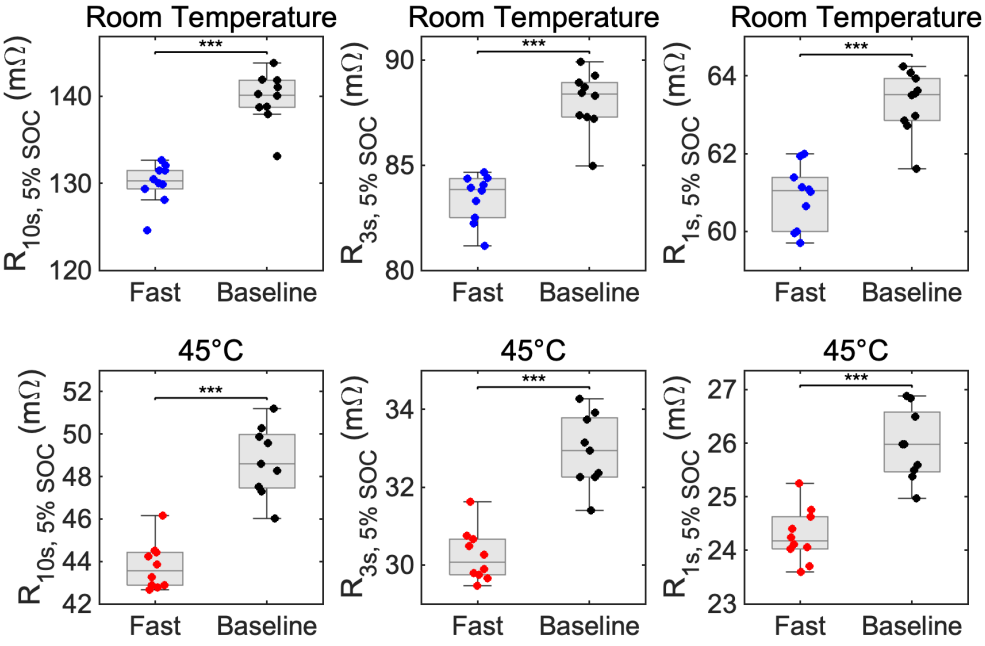

Figure S11. Effect of Pulse Duration on the Cell Resistance Measured From HPPC
Top row: room temperature. Bottom row: 45℃. Values are obtained from the initial Reference Performance Test (RPT) run prior to the start of cycling. '***': statistically significant with p-value < 0.001.

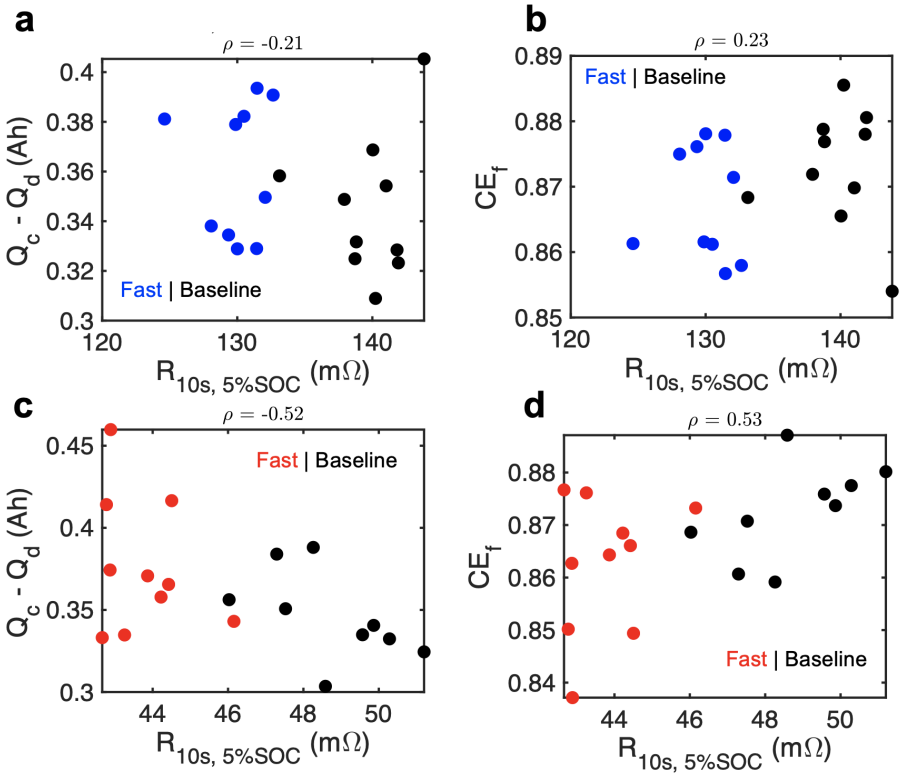

Figure S12. Correlation Between R_{LS} and Conventional Metrics of Lithium Consumption During Formation Conventional metrics include lithium consumed during formation ($Q_{LLI} = Q_c - Q_d$) and Coulombic efficiency (CE_f). (a,b) Correlation with R_{LS} measured at room temperature. (c,d) Correlation with R_{LS} measured at 45 °C. $Q_{LLI} = Q_c - Q_d$ and CE_f are always measured at room temperature since these signals are derived directly from the formation protocol which ran at room temperature. R_{LS} was measured at the temperature of the cycling test.

Room temperature cycling: Fast, Baseline

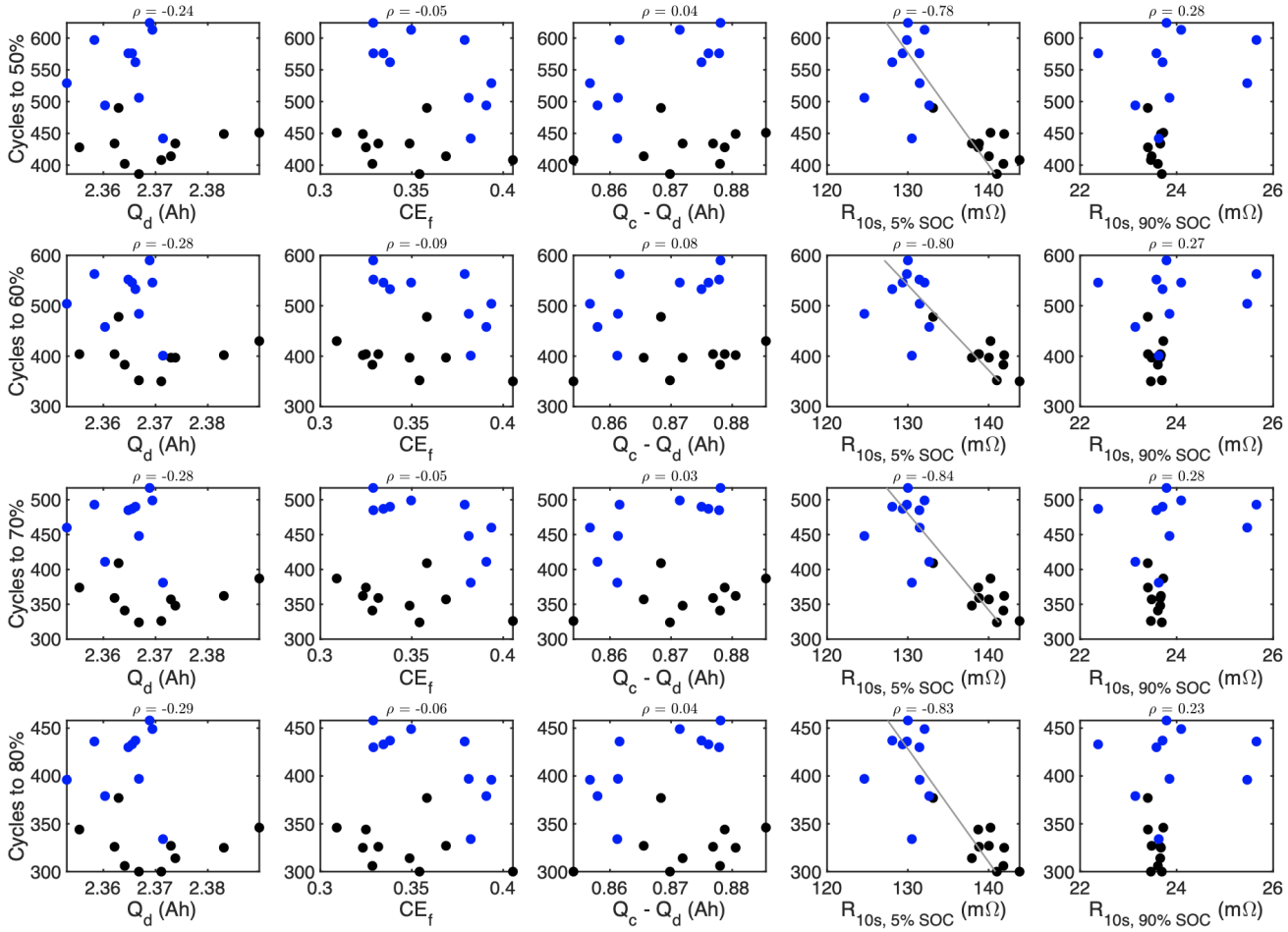

Figure S13. Correlation Between Initial Cell Signals and Cycle Life for Room Temperature Cycling
End of life is defined as cycles to x% of initial capacity, where $x = \{50, 60, 70, 80\}$. Formation signals ($Q_{\mathrm{LLI}} = Q_{\mathrm{c}} - Q_{\mathrm{d}}$ and $\mathrm{CE_f}$) are always measured at room temperature. $\mathrm{R_{10s,5\%SOC}}$ and $\mathrm{R_{10s,90\%SOC}}$ are measured at the same temperature as the cycle life test.

45°C cycling: Fast, Baseline

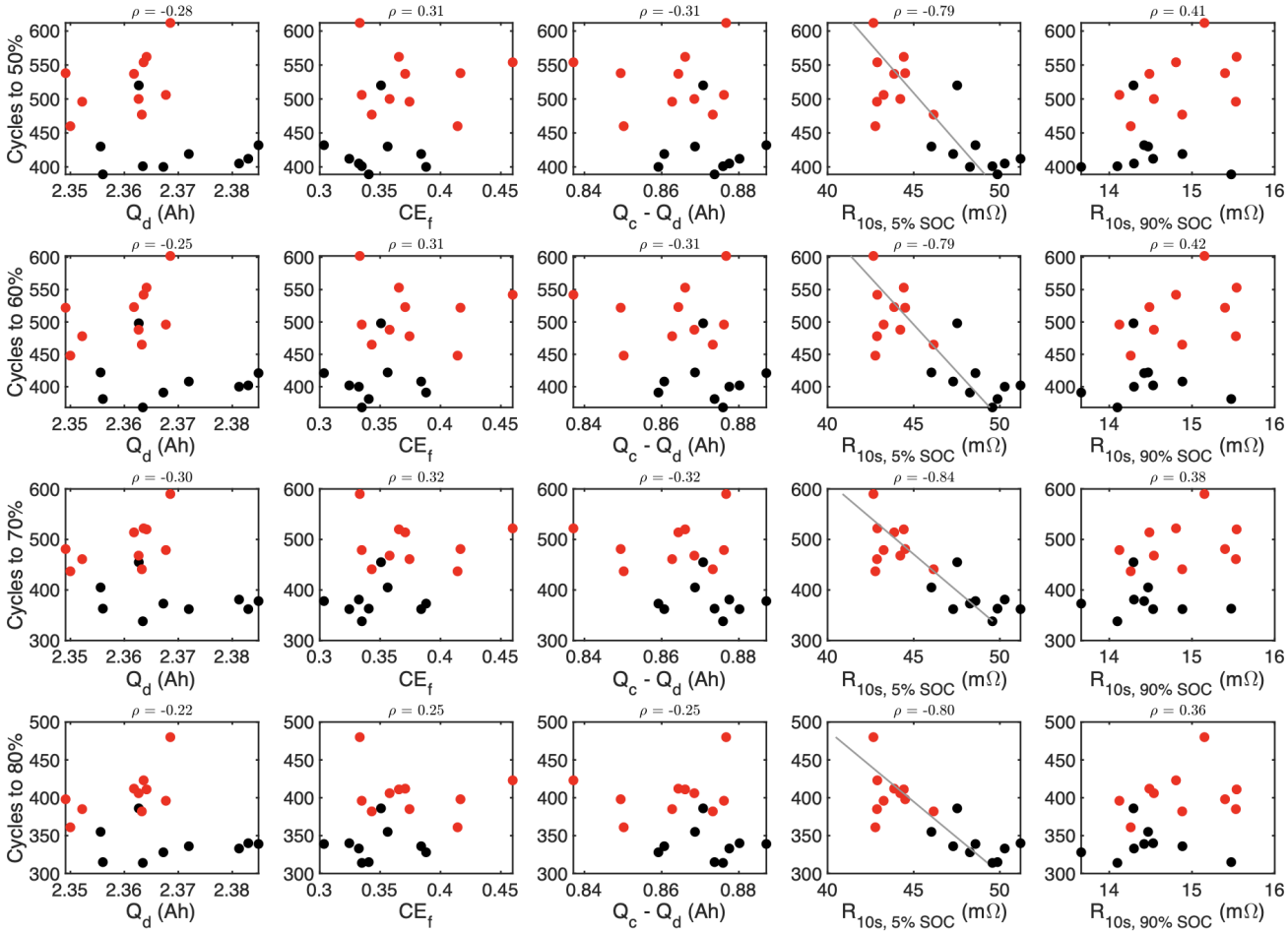

Figure S14. Correlation Between Initial Cell State Signals and Cycle Life for 45℃ Cycling
End of life is defined as cycles to x% of initial capacity, where $x = \{50, 60, 70, 80\}$. Formation signals ($Q_{\mathrm{LLI}} = Q_{\mathrm{c}} - Q_{\mathrm{d}}$ and $\mathrm{CE_f}$) are always measured at room temperature. $\mathrm{R_{10s,5\%SOC}}$ and $\mathrm{R_{10s,90\%SOC}}$ are measured at the same temperature as the cycle life test.

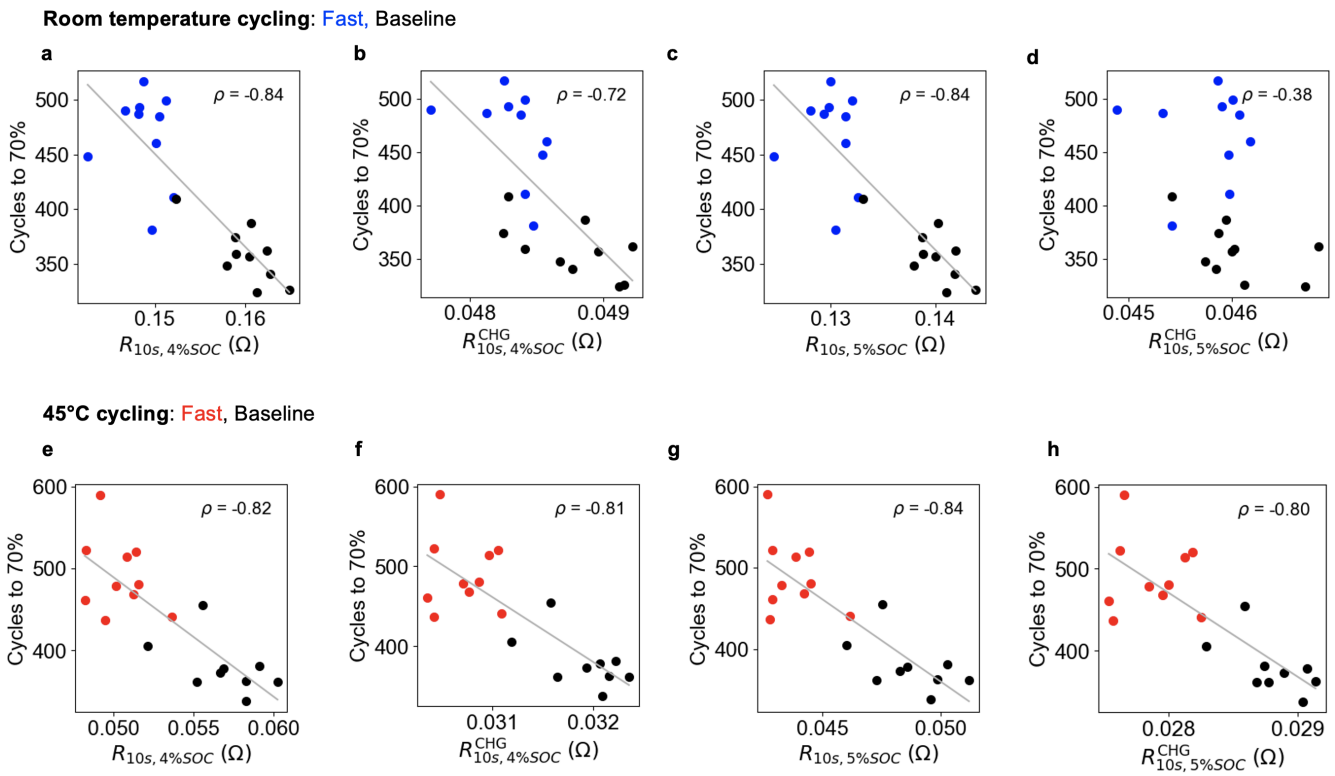

Figure S15. Correlation Between Low-SOC Resistance and Cycle Life: Charge Versus Discharge Pulses Resistances are calculated from either discharge (a,c,e,g) or charge (b,d,f,h) pulses from the Hybrid Pulse Power Characterization (HPPC) sequence. The comparison is provided for resistances evaluated at both 4% SOC (a,b,e,f) and 5% SOC (c,d,g,h).

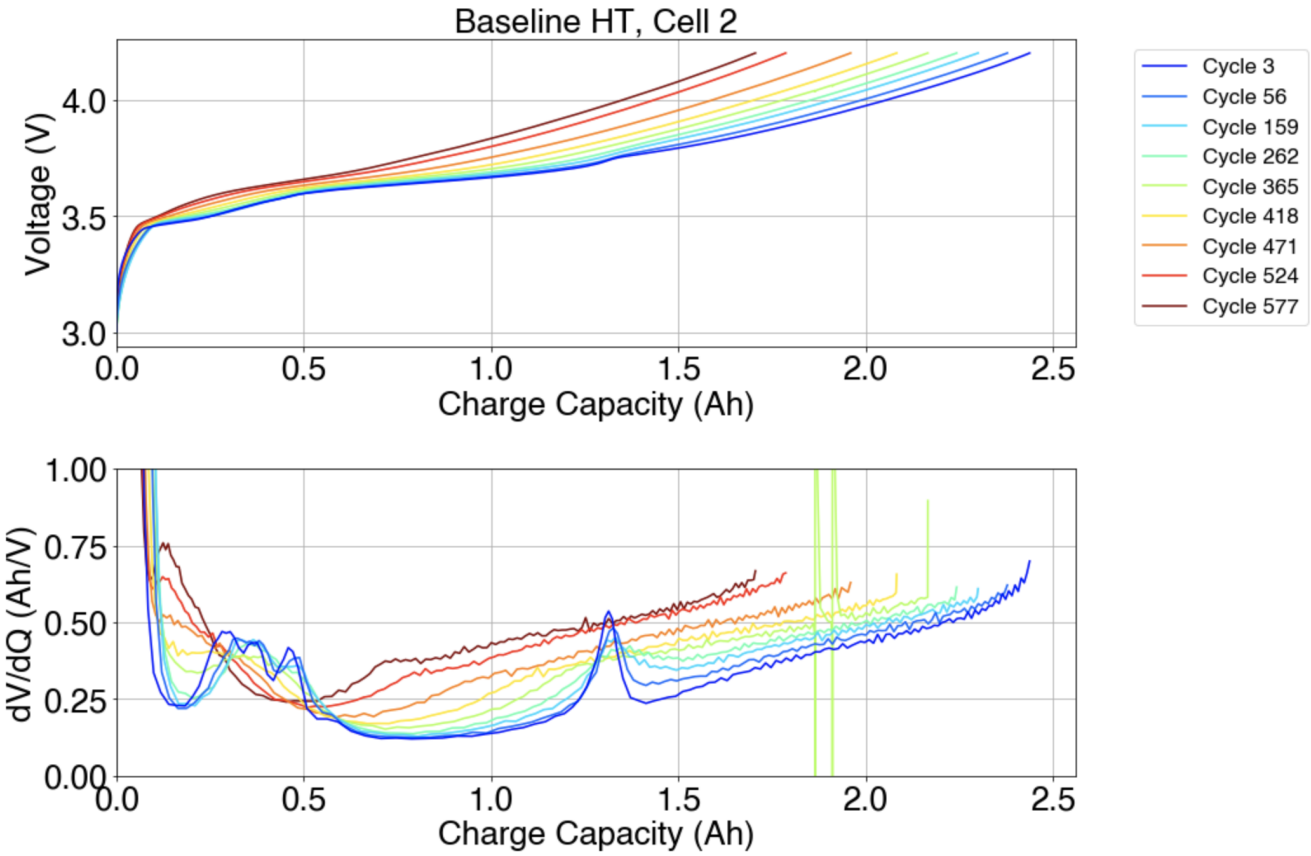

Figure S16. Example Set of C/20 Charge Curves Used for Voltage Fitting Analysis
The C/20 charge curves are embedded as part of the reference performance tests (RPTs).

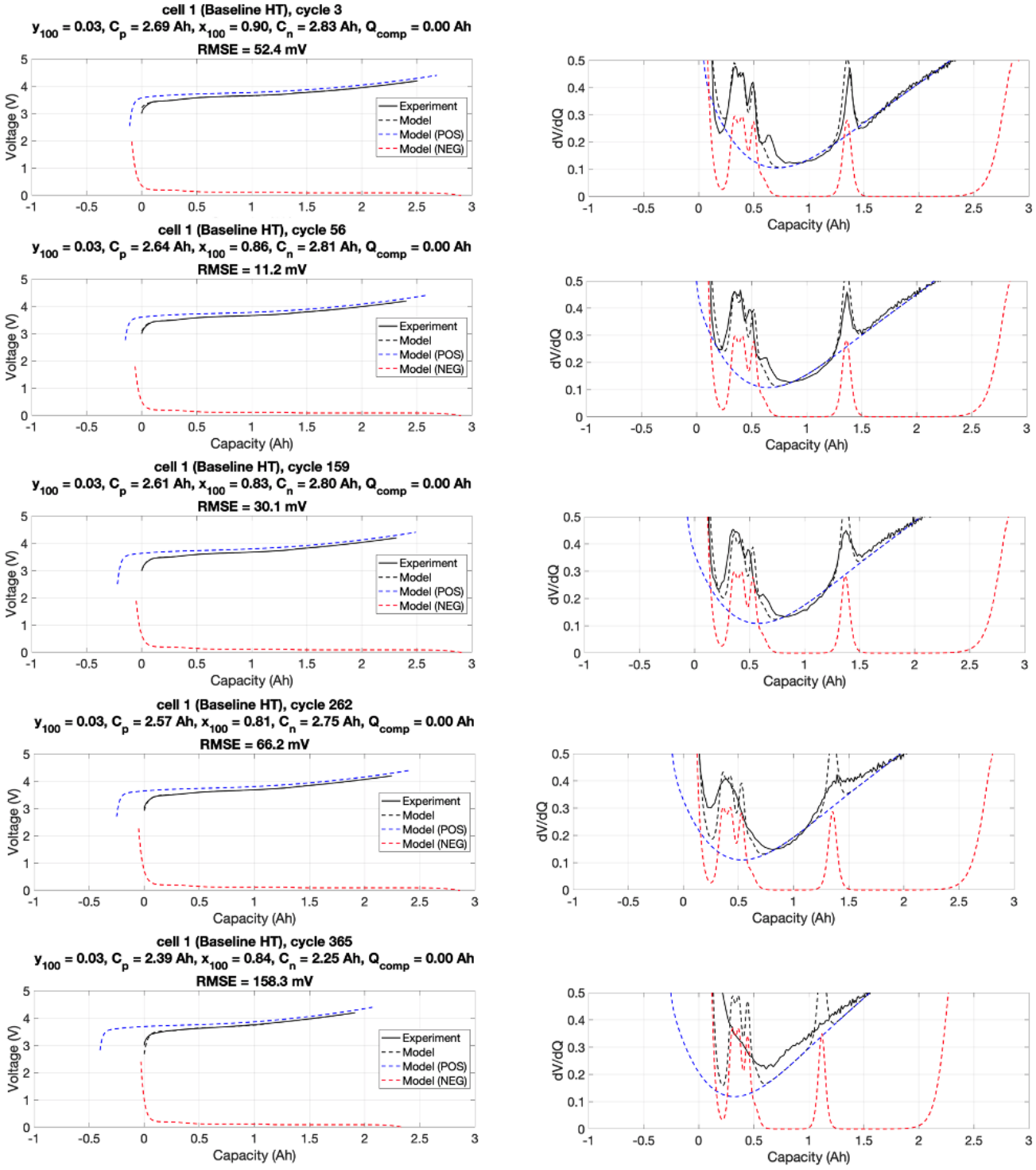

Figure S17. Example of Voltage Fitting Results Obtained on a Single Cell Over Aging
Left column: voltage feature alignment. Right: differential voltage feature alignment. Top row: fresh cell. Bottom row: after 365 cycles have elapsed. Note that the voltage fitting algorithm only consumes voltage data.

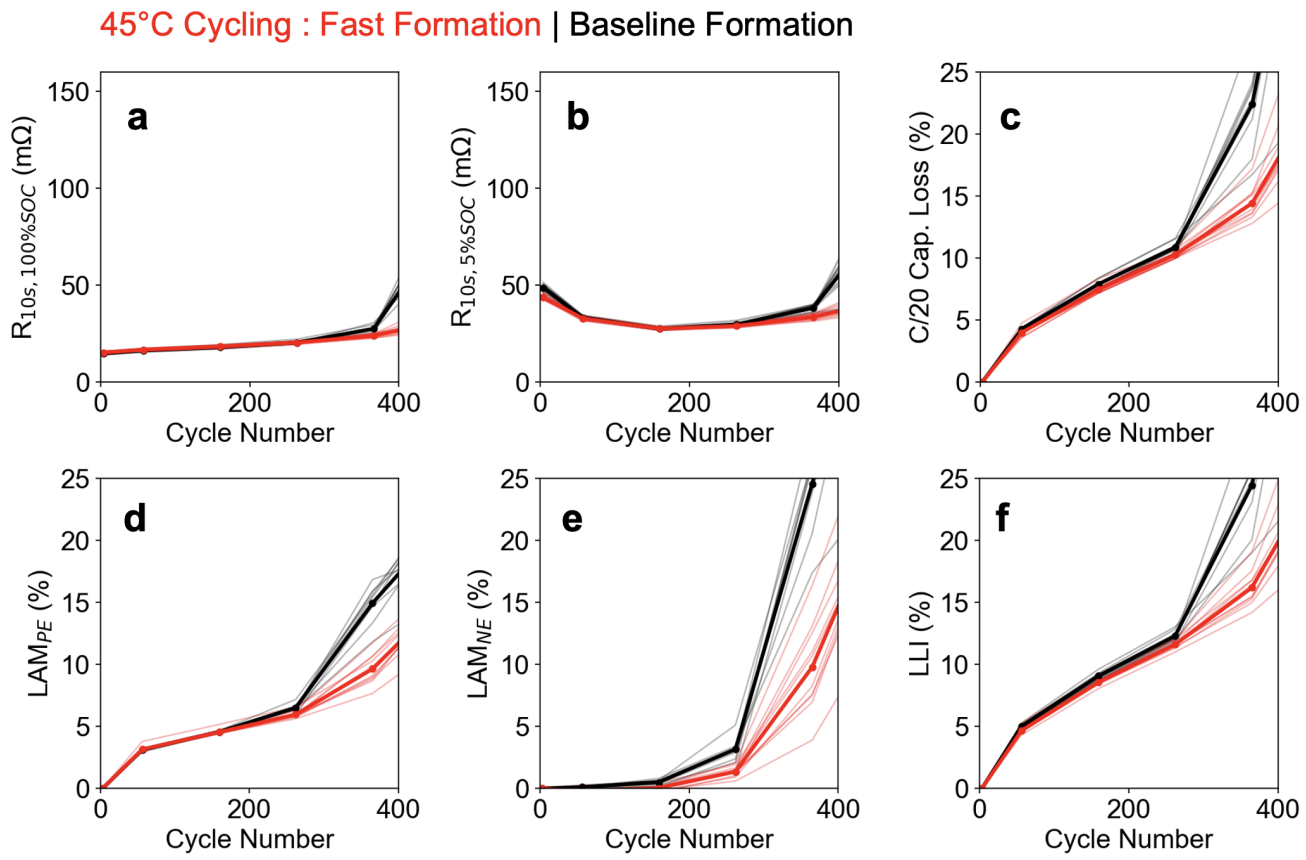

Figure S18. Evolution of Diagnostic Signals Over the course of the 45℃ Cycle Life Test
All metrics shown are calculated using data collected from the Reference Performance Tests (RPTs) run over the course of the cycle life test. Metrics include (a) 10-second resistance calculated at 4% SOC, (b) 10-second resistance calculated at 100% SOC, (c) C/20 discharge capacity loss, (d) loss of active material in the positive electrode, (e) loss of active material in the negative electrode, and (f) loss of lithium inventory. Loss of active material and loss of lithium inventory are calculated using the voltage fitting techniques reported by Lee et al.[1] (e.g. Figure S17). Thick lines show mean values averaged from each group of baseline and fast formation cells. Thin lines show results from individual cells.

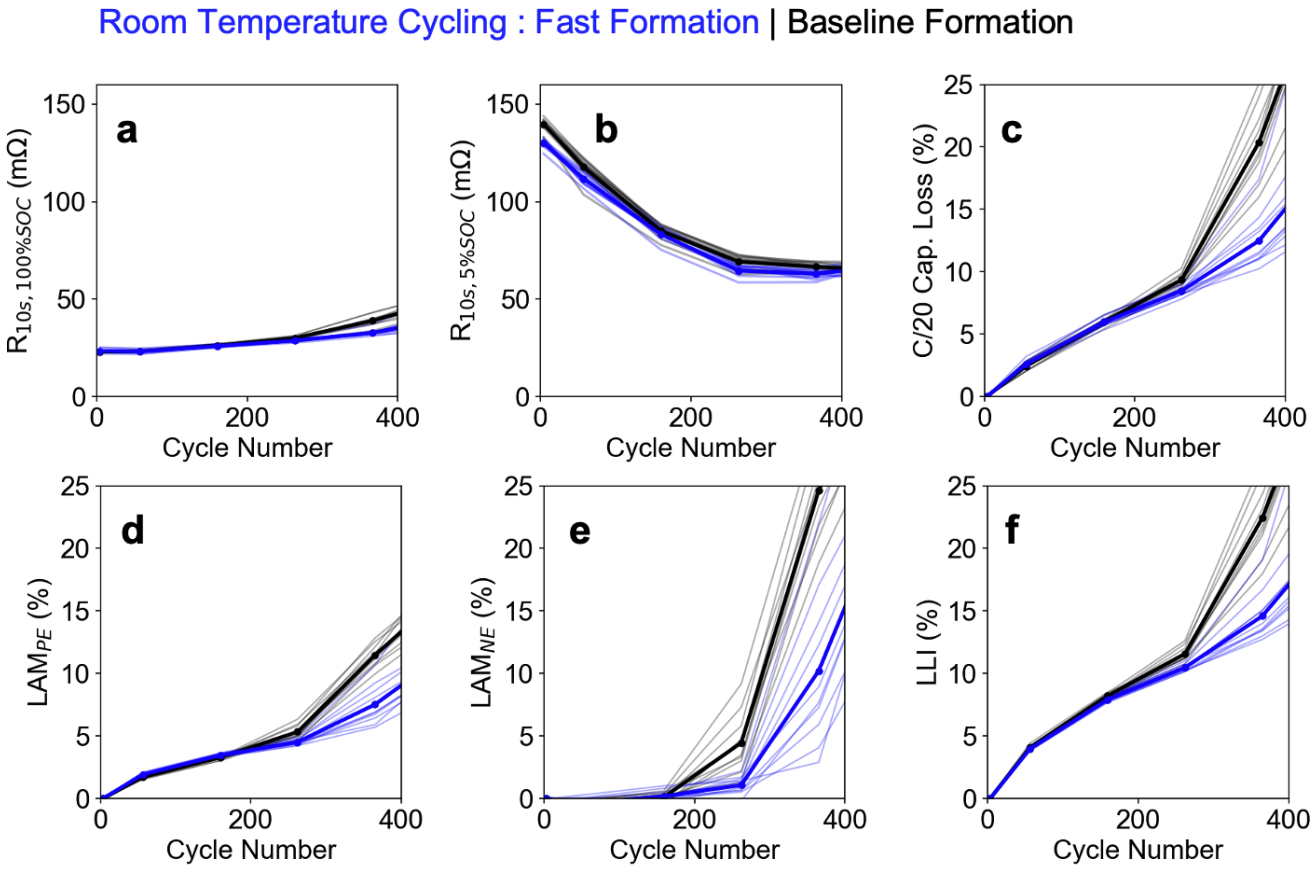

Figure S19. Evolution of Diagnostic Signals Over the Course of the Room Temperature Cycle Life Test All metrics shown are calculated using data collected from the Reference Performance Tests (RPTs) run over the course of the cycle life test. Metrics include (a) 10-second resistance calculated at 4% SOC, (b) 10-second resistance calculated at 100% SOC, (c) C/20 discharge capacity loss, (d) loss of active material in the positive electrode, (e) loss of active material in the negative electrode, and (f) loss of lithium inventory. Loss of active material and loss of lithium inventory are calculated using the voltage fitting techniques reported by Lee et al.[1] (e.g. Figure S17). Thick lines show mean values averaged from each group of baseline and fast formation cells. Thin lines show results from individual cells.

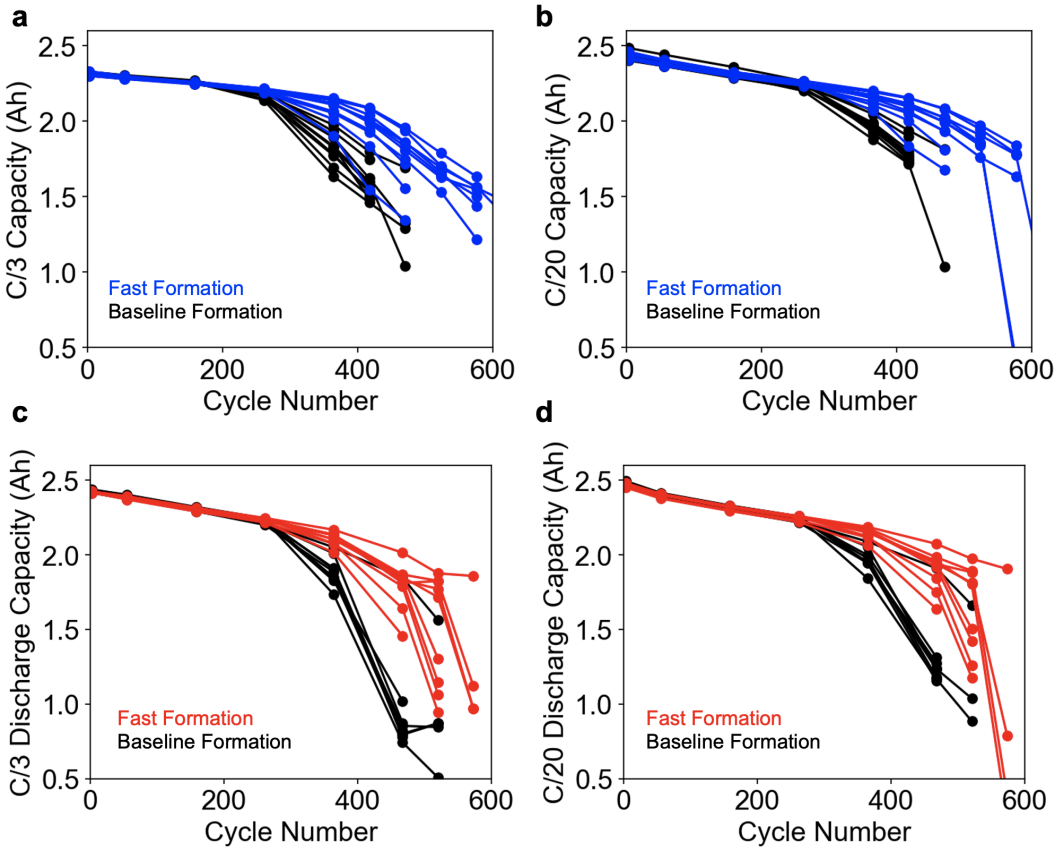

Figure S20. Comparison of Discharge Capacity Versus Cycle Number at Different C-Rates
(a,b) Cycle life tests run at room temperature. (c,d) Cycle life tests run at 45℃. (a,c) C/3 discharge capacity. (b,d) C/20 discharge capacity. All discharge capacities here are measured from the Reference Performance Tests (RPTs).

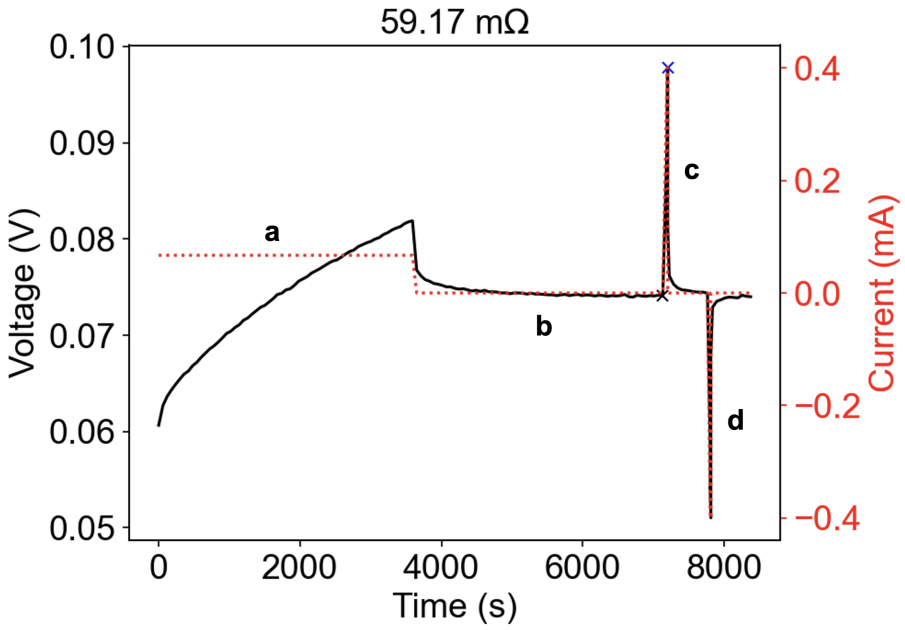

Figure S21. Example Pulse Profile for a Graphite/Li Coin Cell Half Cell
The pulses are obtained as part of the coin cell HPPC test. The coin cell HPPC profile consists of the following repeated sequence: (a) background charge, (b) rest, (c) 10-second charge pulse, and (d) 10-second discharge pulse. The markers (x) indicate the potential difference taken to compute the 10-second resistance using Ohm's law. The potential measured at the end of the rest period (b) is assumed to be in near-equilibrium. The current used during the pulses is 0.4mA for all cells.

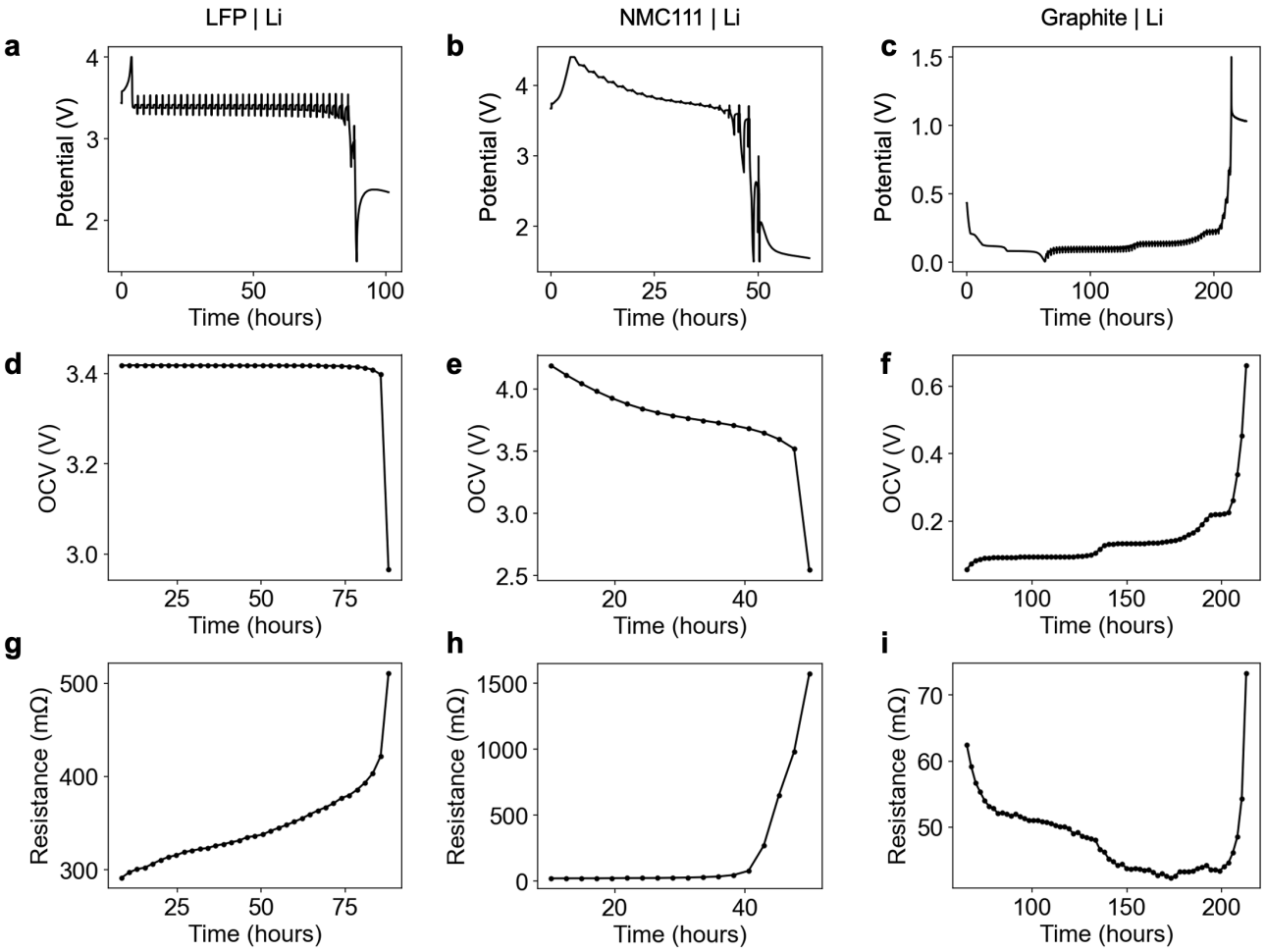

Figure S22. Hybrid Pulse Power Characterization Tests Performed on Coin Cell Half Cells
Potential vs time for (a) LFP/Li, (b) NMC/Li, and (c) Graphite/Li. (d-f) Corresponding pseudo-equilibrium potential curves, where the potential is measured immediately preceding each pulse. (g-h) Calculated 10-second resistances. For the positive electrodes, the resistances are calculated on discharge (i.e. during delithiation). For the graphite negative electrode, the resistances are calculated on charge (i.e. during lithiation).

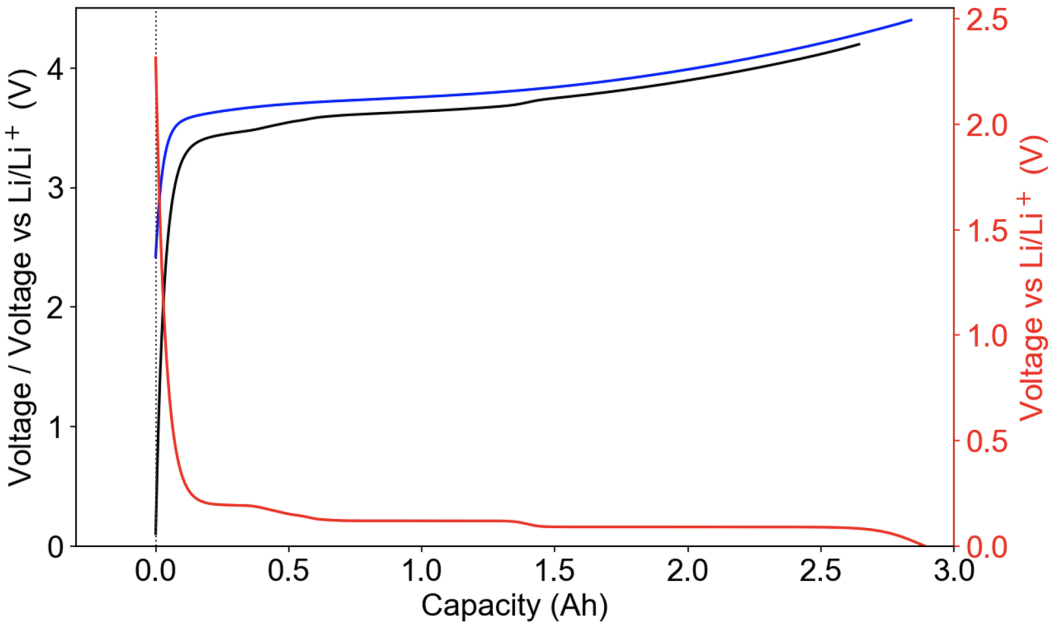

Figure S23. Initial Cell Equilibrium Potential Curves Before Formation
The curves are generated using the electrode stoichiometry model by aligning the point of minimum negative electrode stoichiometry (maximum potential) with the point of maximum positive electrode stoichiometry (minimum potential). Blue: positive electrode. Red: negative electrode. Black: full cell.

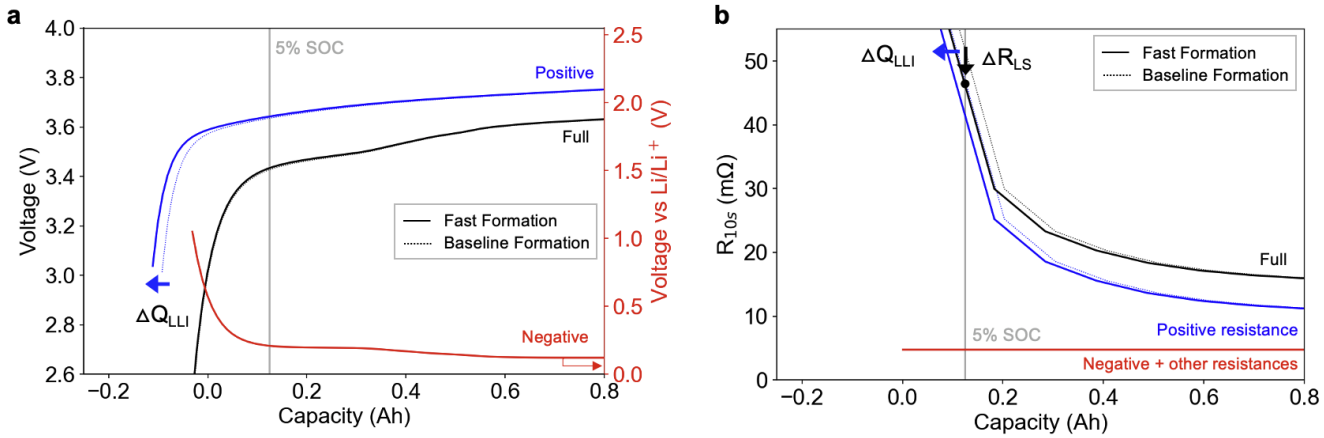

Figure S24. Electrode Stoichiometry Model Illustration
The model shows the impact of fast formation on the alignment of initial cell equilibrium potential curves (a) and resistance curves (b). In this plot, ΔQ_{LLI} has been set to ~23 mAh.

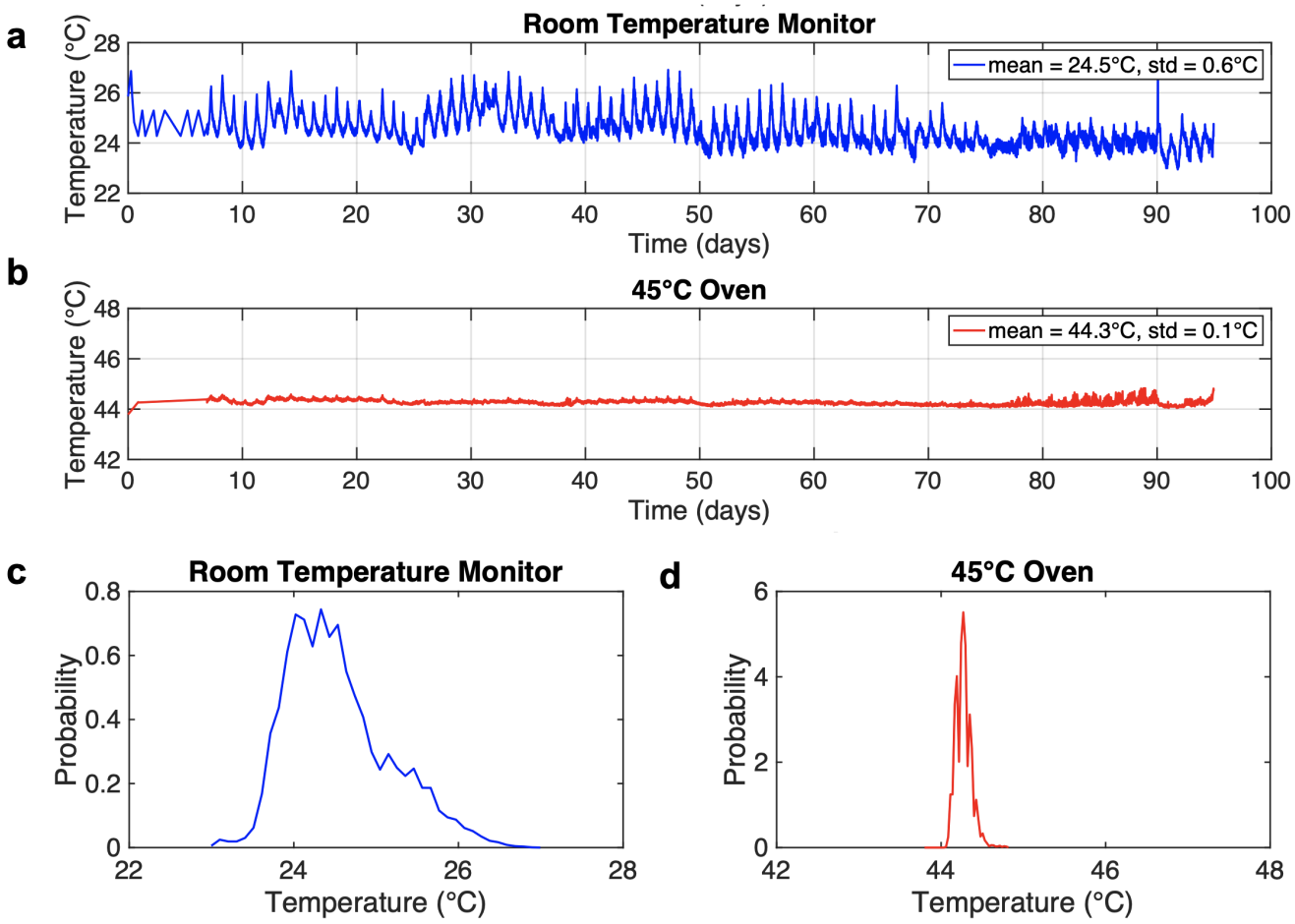

Figure S25. Temperature Measurement During Cycle Life Testing
(a,b) Time-series data for the room temperature (a) and 45℃ (b) tests. (c,d) Temperature histograms for the room temperature (a) and 45℃ (d) tests.

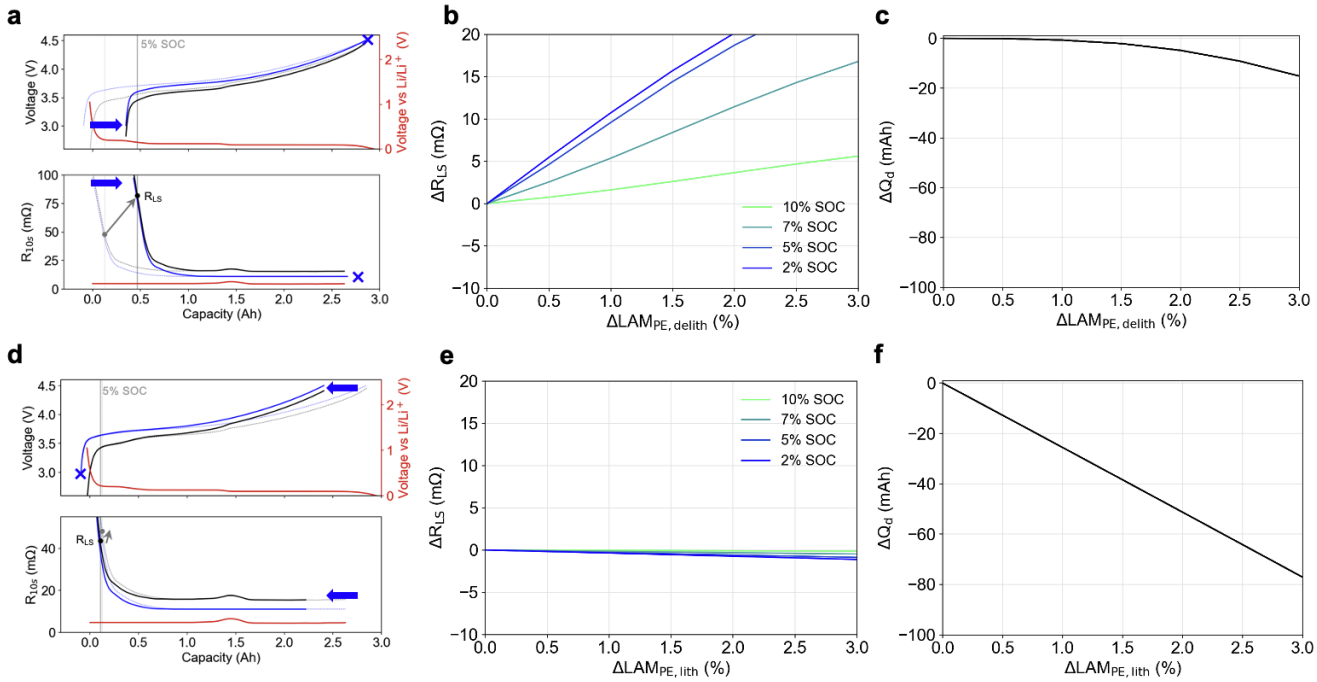

Figure S26. Sensitivity of Low-SOC Resistance to Loss of Active Material in the Positive Electrode
(a-c) Impact of loss of positive active material in the delithiated state. (d-e) Impact of loss of positive active material in the lithiated state. (c,f) Sensitivity of discharge capacity to loss of active material in the positive electrode. In (a,d), LAM is set to 15% for graphical clarity.

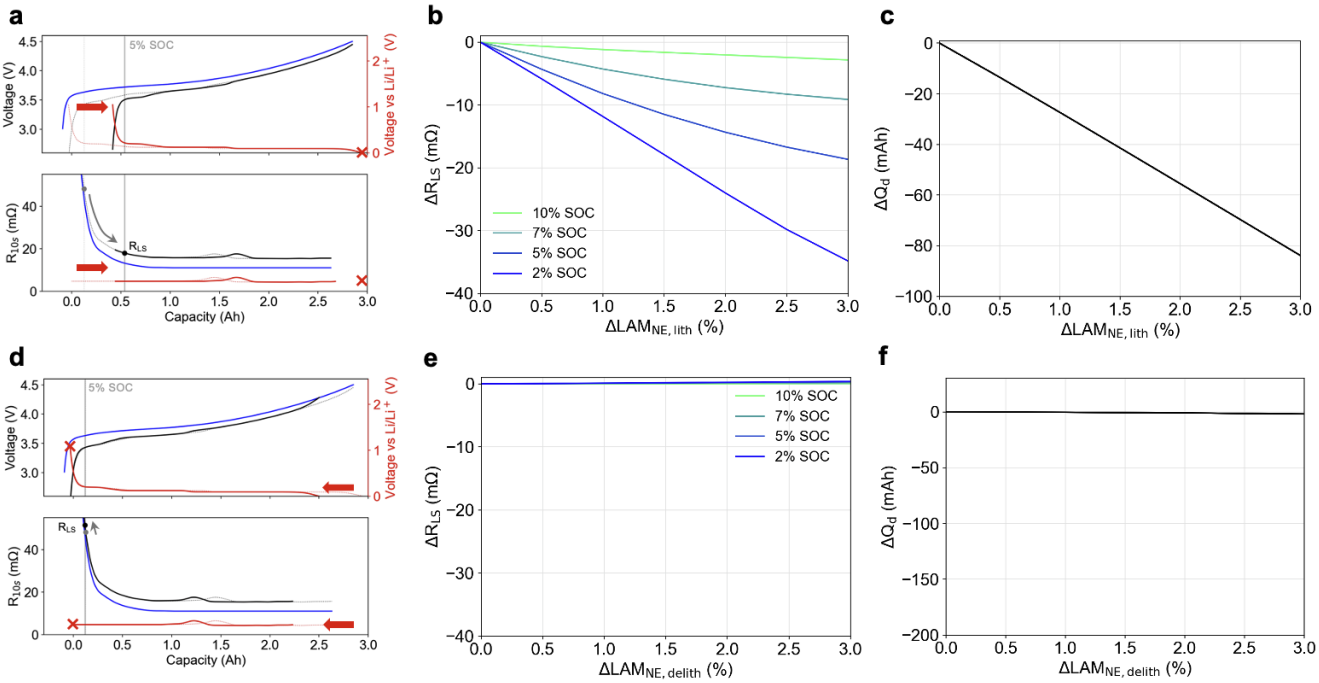

Figure S27. Sensitivity of Low-SOC Resistance to Loss of Active Material in the Negative Electrode
(a-c) Impact of loss of negative active material in the lithiated state. (d-e) Impact of loss of negative active material in the delithiated state. (c,f) Sensitivity of discharge capacity to loss of active material in the negative electrode. In (a,d), LAM is set to 15% for graphical clarity.

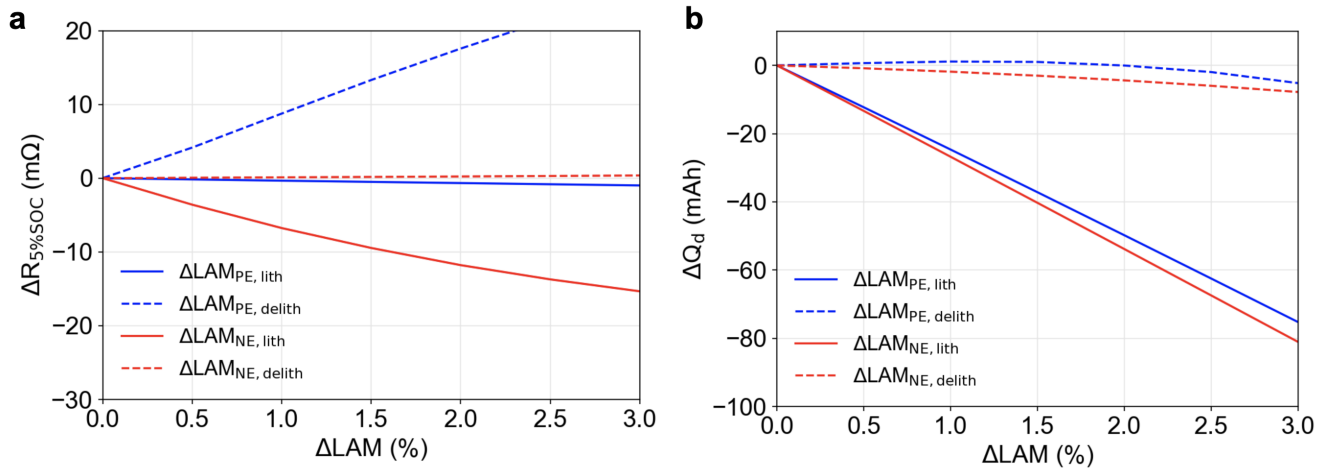

Figure S28. Sensitivity of Low-SOC Resistance and Discharge Capacity to Active Material Loss: Summary
(a) Sensitivity of low-SOC resistance to different active material loss types. (b) Sensitivity of discharge capacity to different active material loss types. In general, active material can be lost at both the positive and negative electrodes, as well as in the lithiated and delithiated states.

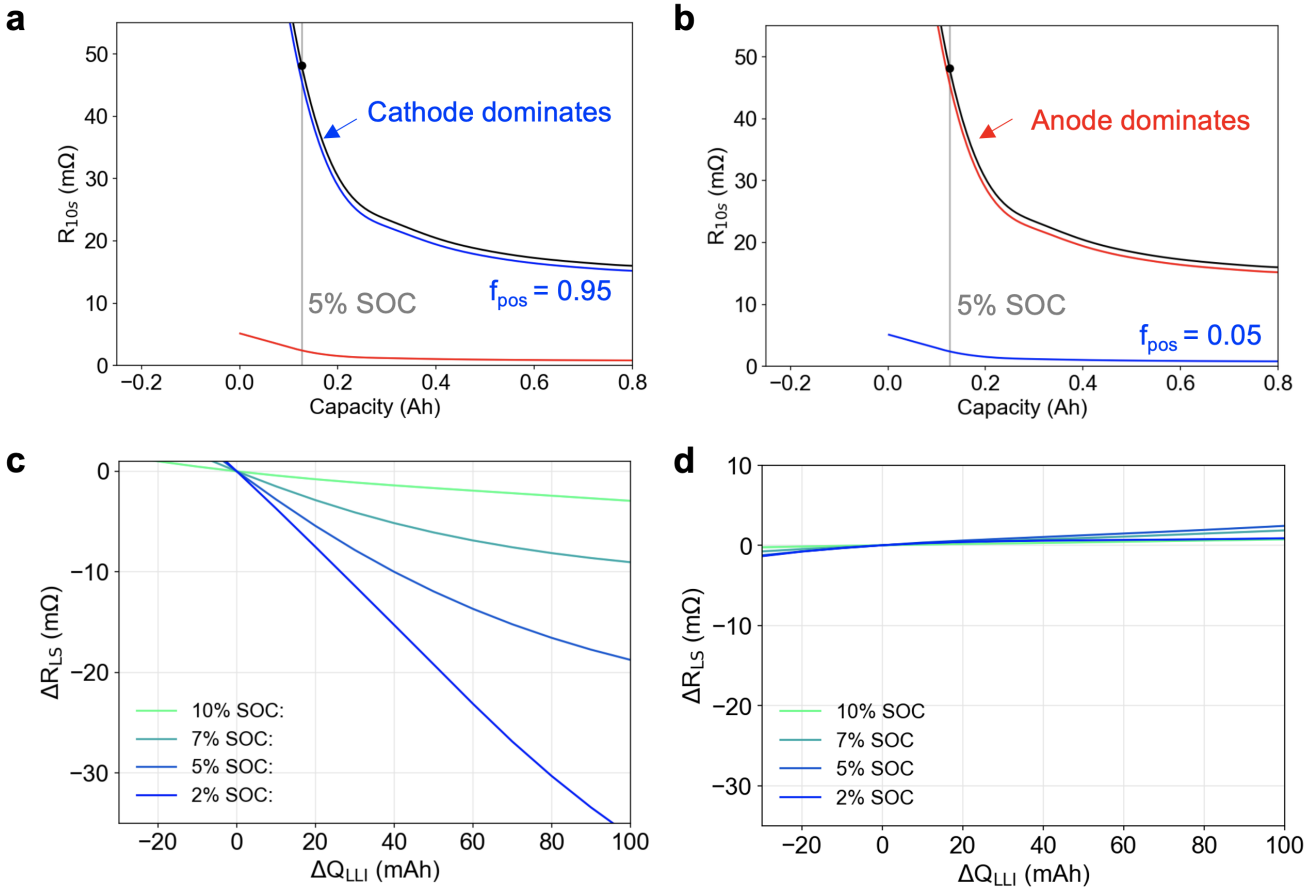

Figure S29. Sensitivity of Low-SOC Resistance to ΔQ_{LLI} Depends on Fractional Contribution of the Positive Electrode to the Total Cell Resistance: Example 1
Sensitivity of the low-SOC resistance metric to ΔQ_{LLI} when (a,c) positive electrode dominates the cell resistance and when (b,d) negative electrode dominates the cell resistance. f_{pos} is the fractional contribution of the positive electrode to the total cell resistance.

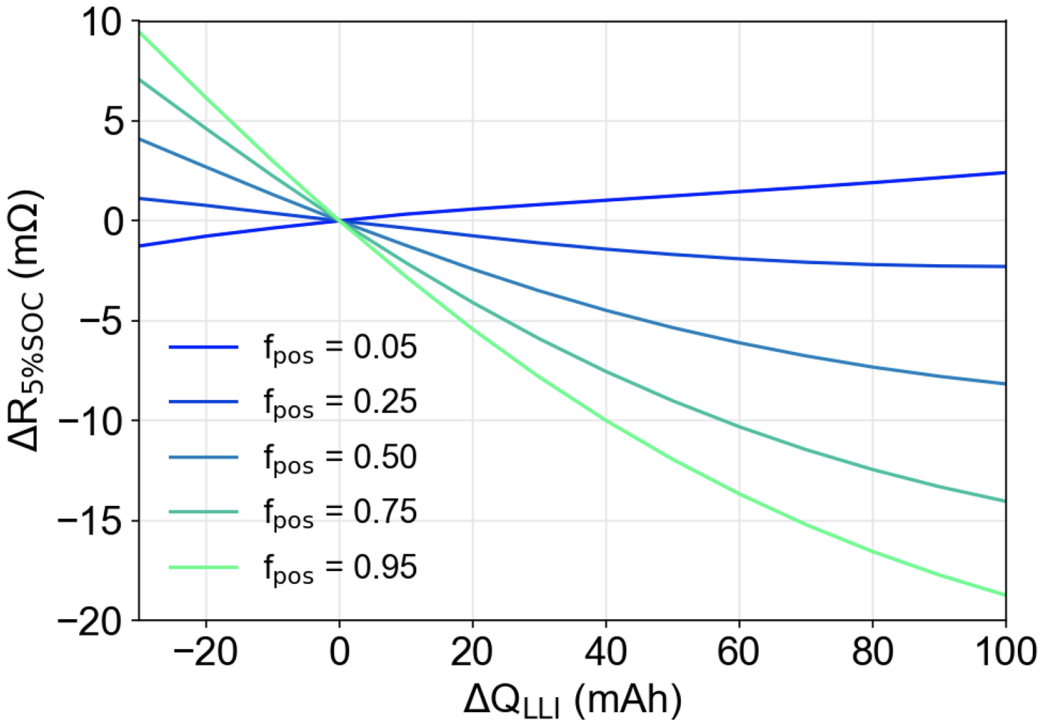

Figure S30. Sensitivity of Low-SOC Resistance to ΔQ_{LLI} Depends on Fractional Contribution of the Positive Electrode to the Total Cell Resistance: Example 2
Sensitivity of the resistance at 5% SOC to ΔQ_{LLI} for varying positive electrode resistance contributions to full cell resistance. f_{pos} is the fractional contribution of the positive electrode to the total cell resistance.

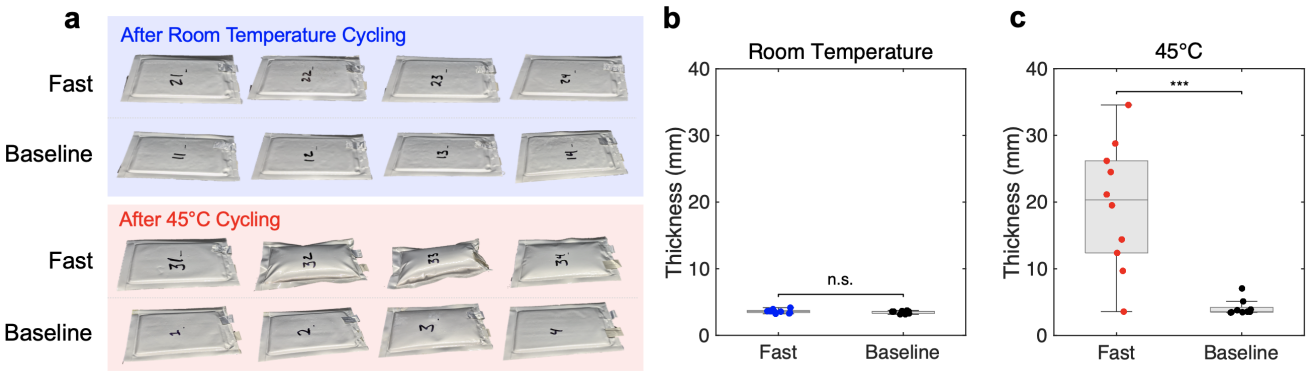

Figure S31. Pouch Cell Swelling at the End of the Cycle Life Test
(a) Example images of pouch cells taken after aging showing varying degrees of swelling. (b-c) Comparison of pouch cell thicknesses measured at the end of the cycle life test. (b) Cells cycled at room temperature. (c) Cells cycled at 45℃. Cell thickness is measured using a manual caliper, which represents the point of maximum deflection. '***' - statistically significant with p-value < 0.001. 'n.s.' - not statistically significant.

Figure S32. Images of Pouch Cells Taken After Aging
Cell #9 has been excluded from the study due to tab weld issues.

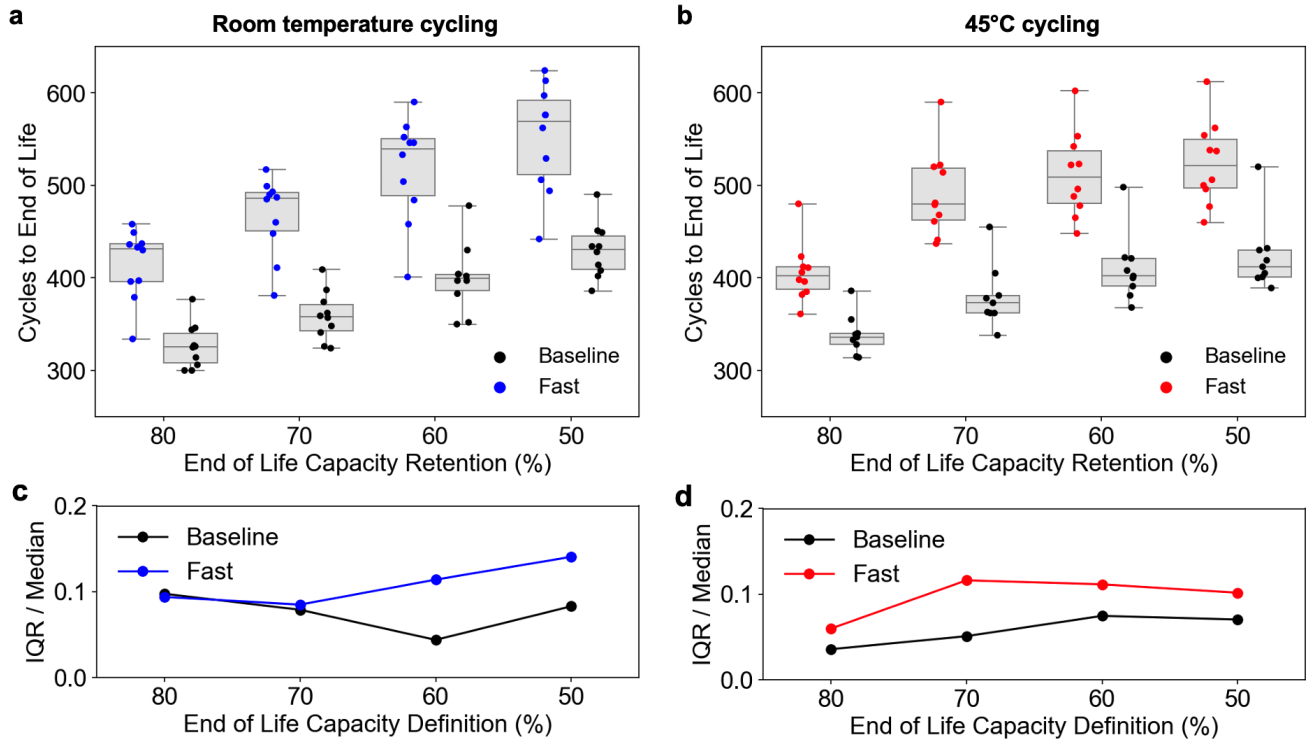

Figure S33. Aging Variability as a Function of End-of-Life Definition
(a,b) Cycles to end of life under (a) room temperature and (b) 45℃ cycling. Boxes show inter-quartile range (IQR) and whiskers show the min and max values. (c,d) Inter-quartile range (IQR) divided by median plotted as a function of end of life capacity definition for (a) room temperature and (b) 45℃ cycling.

Note S1: Signal-to-Noise Analysis on Estimates of Lithium Consumed During Formation

Here, we perform a simple set of calculations to determine the resolution limit of lithium consumed during formation (Q_{LLI}) as a function of the estimation method. We focus on comparing two estimation methods: the low-SOC resistance signal ($\mathrm{R_{LS}}$) and the cell discharge capacity (Q_{d}). Q_{d} represents a conventional signal measured using current integration. In this simplified analysis, we consider only the effect of lithium consumption and ignore possible effect from active material losses. For the analysis, we assume hardware specifications from the battery testing equipment used in our experiments (Maccor Series 4000). The hardware specifications and parameters used in the analysis are provided in Table S2.

Parameter	Symbol	Value	Unit
Voltage Precision	$\mathrm{V_p}$	0.02	% of full scale range
Voltage Full-Scale Range	$\mathrm{V_{FSR}}$	5	V
Current Precision	$\mathrm{I_p}$	0.02	% of full scale range
Current Full-Scale Range	$\mathrm{I_{FSR}}$	5	A
Current Set-Point for $\mathrm{R_{LS}}$ Calculations	$\mathrm{I_{set,1}}$	2.37 (= 1C)	A
Current Set-Point for Q_{d} Calculations	$\mathrm{I_{set,2}}$	0.237 (= C/10)	A

Table S2. Parameters used for the signal-to-noise analysis

The current and voltage errors $\mathrm{I_{err}}$ and $\mathrm{V_{err}}$ can be calculated as

$$\begin{aligned}\mathrm{I_{err}} &= \mathrm{I_{FSR}} \cdot \mathrm{I_p}/100 \\ &= 0.001\mathrm{A}\end{aligned} \tag{1}$$

$$\begin{aligned}\mathrm{V_{err}} &= \mathrm{V_{FSR}} \cdot \mathrm{V_p}/100 \\ &= 0.001\mathrm{V}.\end{aligned} \tag{2}$$

The resolution limit for resistance, $\mathrm{R_{limit}}$, can be calculated as

$$\begin{aligned}\mathrm{R_{limit}} &= \mathrm{R_{high}} - \mathrm{R_{low}} \\ &= 0.88\mathrm{m}\Omega\end{aligned} \tag{3}$$

where

$$\mathrm{R_{high}} = \frac{\Delta V_{\mathrm{meas}} + \mathrm{V_{err}}}{\mathrm{I_{set,1}} - \mathrm{I_{err}}} \tag{4}$$

$$\mathrm{R_{low}} = \frac{\Delta V_{\mathrm{meas}} - \mathrm{V_{err}}}{\mathrm{I_{set,1}} + \mathrm{I_{err}}}. \tag{5}$$

In these equations, $\Delta \mathrm{V_{meas}}$ is the measured voltage drop during the discharge pulse. From Figure S8, this value is less than 0.1V at low SOCs. For the remaining calculation, we assume $\Delta \mathrm{V_{meas}} = 0.1V$.

The resolution limit for a capacity measurement can be estimated as

$$\begin{aligned}\mathrm{Q_{limit}} &= \mathrm{Q_{high}} - \mathrm{Q_{low}} \\ &= 20\mathrm{mAh}\end{aligned} \tag{6}$$

where

$$\mathrm{Q_{high}} = (\mathrm{I_{set,2}} + \mathrm{I_{err}}) \cdot 10 \text{ hours} \tag{7}$$

$$\mathrm{Q_{low}} = (\mathrm{I_{set,2}} - \mathrm{I_{err}}) \cdot 10 \text{ hours}. \tag{8}$$

These capacities correspond to the C/10 constant current discharge steps during the final diagnostic cycle of the formation protocol (Figure S1b,c). Here, we neglect the effect of voltage inaccuracies which would add an additional error in the voltage termination condition for the discharge cycle. By ignoring this error, the estimate of the resolution limit for Q_{d} remains optimistic.

To calculate the sensitivity of ΔQ_{LLI} to $\Delta \mathrm{R_{LS}}$, we linearize the curve from Figure 4d at 5% SOC to find that

$$\begin{aligned} \frac{\Delta Q_{\mathrm{LLI}}}{\mathrm{R_{10s,5\%SOC}}} &= \frac{40\mathrm{mAh}}{10\mathrm{m\Omega}} \\ &= 5.00\mathrm{mAh/m\Omega}. \end{aligned} \tag{9}$$

A similar exercise is done for ΔQ_{d} which yields

$$\begin{aligned} \frac{\Delta Q_{\mathrm{LLI}}}{\Delta Q_{\mathrm{d}}} &= \frac{40\mathrm{mAh}}{37\mathrm{mAh}} \\ &= 1.08\mathrm{mAh/mAh}. \end{aligned} \tag{10}$$

Finally, the resolution of Q_{LLI} calculated using the two different methods are computed as

$$\begin{aligned} Q_{\mathrm{LLI}} \text{ calculated from } \mathrm{R_{10s,5\%SOC}} &= \frac{\Delta Q_{\mathrm{LLI}}}{\Delta \mathrm{R_{10s,5\%SOC}}} \cdot \mathrm{R_{limit}} \\ &= 3.9\mathrm{mAh} \end{aligned} \tag{11}$$

$$\begin{aligned} Q_{\mathrm{LLI}} \text{ calculated from } Q_{\mathrm{d}} &= \frac{\Delta Q_{\mathrm{LLI}}}{\Delta Q_{\mathrm{d}}} \cdot \mathrm{Q_{limit}} \\ &= 22.2\mathrm{mAh}. \end{aligned} \tag{12}$$

This simple calculation demonstrates that the low-SOC resistance metric improves the resolution limit of Q_{LLI} by five-fold compared to the same calculation made using Q_{d}.

We note that $\mathrm{Q_{limit}} = 20$ mAh corresponds to the magnitude of the difference in lithium consumed between the fast formation and baseline formation protocols (23 mAh), which confirms that it would be difficult to detect such small changes in lithium consumption using ordinary cycler equipment.

The precision of the Q_{d} measurement can be improved in several ways. First, a higher C-rate discharge would lead to less current integration error and higher accuracy. However, a high-rate discharge would also include a kinetic contribution making it more difficult to correlate to lithium loss. Second, Q_{d} can also be improved by using higher precision cyclers. For example, if the voltage and current precision both increased by 100-fold, then the resolution limit of Q_{LLI} calculated from Q_{d} will have improved to 0.2 mAh. However, in this scenario, the resolution limit of Q_{LLI} calculated from $\mathrm{R_{10s,5\%SOC}}$ would also have improved to 0.04 mAh.

Note S2: Origin of Gas Evolution over Cycle Life Due to Fast Formation

At the negative electrode, some common gas-generating reaction pathways include the reduction of ethylene carbonate (EC) to form carbon monoxide (CO) and the reduction of water impurities (e.g. from manufacturing) which can form carbon dioxide (CO_2) and hydrogen gas[2]. Since every cell in the experiment was taken from the same manufacturing batch, their water content is expected to be similar. It is therefore unlikely that water reduction pathways is the major source of difference in the amount of gas formed between the two different formation protocols. Next, the reduction of EC is lithium-consuming and thus the amount of CO formed through this reaction pathway is expected to correlate to the loss of lithium inventory (LLI) over life. However, our voltage fitting analysis (Figures S18, S19) suggests that the rate of LLI for fast formation cells is equal to or lower than that of baseline formation. We therefore expect the formation rate of CO from the EC reduction pathway to be comparable between the two different formation protocols. From this brief survey, it is unlikely that a reaction pathway based on the negative electrode can account for differences in measured gas amount over life between the two different formation protocols.

We note that oxidation reactions at the positive electrode (e.g. at high potentials) can also contribute to gas evolution over aging. Common reaction pathways at the positive electrode include the decomposition of lithium carbonate at the surface of the NMC electrodes and the oxidation of EC. The reaction products include the generation of CO_2, CO, and oxygen gas[2]. These reactions are known to accelerate at higher positive electrode potentials vs Li/Li^+, a phenomenon studied in detail by Jung et al.[3].

To determine whether fast formation could have caused the positive electrode to experience higher potentials at the top of charge, we used the electrode stoichiometry model to measure the impact of increased lithium consumption during formation on the positive electrode potential vs Li/Li^+ at the top of charge (i.e. 4.2V in the full cell). The result, shown in Figure S34, illustrates how an increase in the magnitude of ΔQ_{LLI} shifts the positive electrode stoichiometry window towards marginally lower values at both the bottom of discharge and the top of charge. From this graphical analysis, we see that the positive electrode stoichiometry at the top of charge (i.e. 4.2V in the full cell) has increased by 0.5 mV vs Li/Li^+. Thus, fast formation may have increased the positive electrode potential at the top of charge, creating a more oxidizing environment and promoting more gas generation. While the difference in the potential is marginal, a small change in oxidation rates could lead to a large difference in accumulated gas generated over the course of hundreds of cycles. We also note that a significant portion of the charge cycles are spent in the CV hold phase where the positive electrode would stay at this higher potential. A similar mechanism has been identified as part of work by Dose et al.[4]. Note that Dose et al. observed that the positive electrode impedance increased due to these oxidation reactions, but in our work, this impedance rise was not observed (Figure S18a).

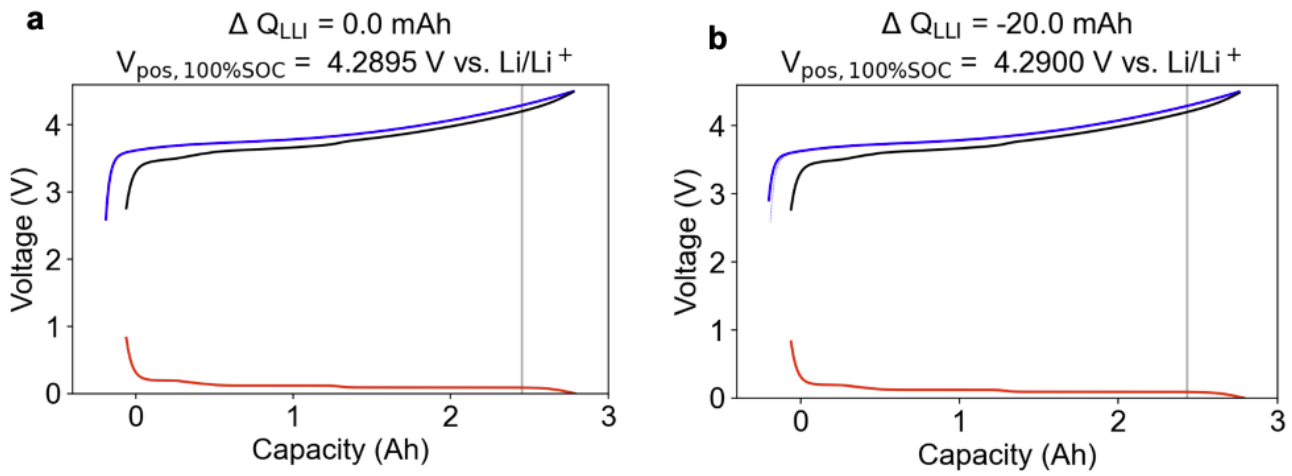

Figure S34. Electrode stoichiometry model showing the impact of 20 mAh of additional lithium loss on the positive electrode potential at the top of charge. (a) Model for baseline formation. (b) Model for fast formation.

In general, gas build-up represents the combination of gas both generated and consumed. Xiong et al.[5]

demonstrated that gas in NMC-graphite cells can be generated at the positive electrode and subsequently reduced at the negative electrode via a 'shuttle' mechanism[6]. At the positive electrode, gas species such as O_2, CO, and CO_2 can be generated through electrolyte oxidation pathways[2,3], and at the negative electrode, gas species can be further reduced into solid products[2]. Fast formation may be exacerbating the gas generation rate, suppressing the gas consumption rate, or both.

We further hypothesize that the gas build-up over life may have a secondary benefit to cycle life. Krause et al.[7] and Chevrier et al.[8] have reported that the reduction of CO_2 at the negative electrode contributes to the SEI growth process and have a stabilizing effect. Since fast formation had increased cycle life, it is possible that more CO_2 is being generated at the positive electrode and reduced at the negative electrode, further improving SEI passivation and delaying the knee-point. More experimental work will be needed to confirm this theory.

Note S3: Effect of Lithium Consumption during Formation on Maximum Positive Electrode Stoichiometry

A careful study of the electrode-specific equilibrium potential curves suggests another possible contributor to the improved cycle life seen in fast formation cells. Returning to Figure 4a, we observe that the capacity corresponding to the extra lithium consumed from fast formation, ΔQ_{LLI}, is also associated with a decrease in the maximum positive electrode stoichiometry, y_{max}. Since fast formation consumed more lithium to create the SEI, the positive electrode becomes less fully lithiated when the cell is fully discharged. By comparison, the positive electrodes of baseline formation cells will be more lithiated at the end of discharge.

Access to higher positive electrode lithiation states is associated with higher levels of particle-level stress, leading to more likelihood for cracking of the ceramic oxide secondary particles[9–11]. Stress-induced cracking over life can lead to electrical isolation of particles, resulting in loss of active sites. The cracking may also expose additional surface area which could accelerate the rate of parasitic reactions leading to earlier knee-points[12]. We speculate that this difference in y_{max}, while small, could protect the fast formation cells against cracking over the course of many cycles, leading to an overall improvement in the overall cycle life. This degradation mechanism is particularly relevant in our testing where every cycle ends on the minimum voltage target of 3.0V. This 'hidden degradation mechanism' involving the positive electrode motivates the usage of the low-SOC resistance, $\Delta \mathrm{R}_{\mathrm{LS}}$, to quantify the small changes in Δy_{max} due to new formation protocols.

References

[1] S. Lee, J. B. Siegel, A. G. Stefanopoulou, J.-W. Lee, and T.-K. Lee, "Electrode State of Health Estimation for Lithium Ion Batteries Considering Half-cell Potential Change Due to Aging", Journal of The Electrochemical Society **167**, 090531 (2020).

[2] B. Rowden and N. Garcia-Araez, "A review of gas evolution in lithium ion batteries", Energy Reports **6**, 10–18 (2020).

[3] R. Jung, M. Metzger, F. Maglia, C. Stinner, and H. A. Gasteiger, " Oxygen Release and Its Effect on the Cycling Stability of LiNi x Mn y Co z O 2 (NMC) Cathode Materials for Li-Ion Batteries ", Journal of The Electrochemical Society **164**, A1361–A1377 (2017).

[4] W. M. Dose, C. Xu, C. P. Grey, and M. F. De Volder, "Effect of Anode Slippage on Cathode Cutoff Potential and Degradation Mechanisms in Ni-Rich Li-Ion Batteries", Cell Reports Physical Science **1**, 100253 (2020).

[5] D. J. Xiong, L. D. Ellis, R. Petibon, T. Hynes, Q. Q. Liu, and J. R. Dahn, "Studies of Gas Generation, Gas Consumption and Impedance Growth in Li-Ion Cells with Carbonate or Fluorinated Electrolytes Using the Pouch Bag Method", Journal of The Electrochemical Society **164**, A340–A347 (2017).

[6] L. D. Ellis, J. P. Allen, L. M. Thompson, J. E. Harlow, W. J. Stone, I. G. Hill, and J. R. Dahn, "Quantifying, Understanding and Evaluating the Effects of Gas Consumption in Lithium-Ion Cells", Journal of The Electrochemical Society **164**, A3518–A3528 (2017).

[7] L. J. Krause, V. L. Chevrier, L. D. Jensen, and T. Brandt, "The Effect of Carbon Dioxide on the Cycle Life and Electrolyte Stability of Li-Ion Full Cells Containing Silicon Alloy", Journal of The Electrochemical Society **164**, A2527–A2533 (2017).

[8] V. L. Chevrier, L. J. Krause, L. D. Jensen, C. Huynh, M. Triemert, E. L. Bowen, and J. Thorson, "Design of Positive Electrodes for Li-Ion Full Cells with Silicon", Journal of The Electrochemical Society **165**, A2968–A2977 (2018).

[9] M. Li, M. Feng, D. Luo, and Z. Chen, "Fast Charging Li-Ion Batteries for a New Era of Electric Vehicles", Cell Reports Physical Science **1**, 100212 (2020).

[10] S. Watanabe, M. Kinoshita, T. Hosokawa, K. Morigaki, and K. Nakura, "Capacity fade of LiAlyNi1-x-yCoxO 2 cathode for lithium-ion batteries during accelerated calendar and cycle life tests (surface analysis of LiAlyNi1-x-yCo xO2 cathode after cycle tests in restricted depth of discharge ranges)", Journal of Power Sources **258**, 210–217 (2014).

[11] S. S. Zhang, "Problems and their origins of Ni-rich layered oxide cathode materials", Energy Storage Materials **24**, 247–254 (2020).

[12] X. Ma, J. E. Harlow, J. Li, L. Ma, D. S. Hall, S. Buteau, M. Genovese, M. Cormier, and J. R. Dahn, " Editors' Choice—Hindering Rollover Failure of Li[Ni 0.5 Mn 0.3 Co 0.2]O 2 /Graphite Pouch Cells during Long-Term Cycling ", Journal of The Electrochemical Society **166**, A711–A724 (2019).